Novel optical sensors for chemical and biological applications

by

Jérôme Michon

M.Sc., École Polytechnique (2015)

Submitted to the Department of Materials Science and Engineering
in partial fulfillment of the requirements for the degree of

Doctor of Philosophy

at the

MASSACHUSETTS INSTITUTE OF TECHNOLOGY

June 2019

Author .....
Materials Science and Engineering
May 9, 2019

Certified by .....
Juejun Hu
Associate Professor of Materials Science and Engineering
Thesis Supervisor

Accepted by .....
Donald R. Sadoway
John F. Elliott Professor of Materials Chemistry
Chairman, Department Committee on Graduate Studies

Novel optical sensors for chemical and biological applications

by

Jérôme Michon

Submitted to the Department of Materials Science and Engineering
on May 9, 2019, in partial fulfillment of the
requirements for the degree of Doctor of Philosophy in
Materials Science and Engineering.

Abstract

Optical sensors have attracted a lot of interest due to their increased performance and ability to perform chemical identification through spectroscopy. Integrated sensors present the additional advantages of compactness and increased light-matter interactions. This thesis aimed at advancing the field of photonic sensing by demonstrating novel devices and applications, and improving the performance of current sensors. In particular, we studied flexible integrated photonic sensors and substrates for surface-enhanced Raman spectroscopy.

We first propose and demonstrate a three-dimensional flexible photonic sensor array for stress mapping in soft materials systems such as cell cultures. Our device relies on stress-optical coupling to infer stress from optical measurements and uses a deterministic 3-D fabrication method to precisely position the sensors in space. We characterized the sensors' response to mechanical stimulation by measuring their strain-optical coupling coefficient. Our device is amenable to measuring strains down to 0.001% or forces down to 1 nN in any matrix with a modulus greater than 300 Pa, with a spatial resolution of 100 µm, enabling the detection of the effects of about a dozen cells. Overall, our device provides fast, easy, and precise measurements even in opaque samples, in a greater range of volumes and geometries than previously available. More broadly, this platform prefigures the ability to perform multifunctional sensing and light delivery in three dimensions.

In addition, we look at the efficiency of surface-enhanced Raman spectroscopy (SERS), a popular spectroscopy technique with a broad range of applications. Using a reasoning based on the local density of states (LDOS), we derived a limit for the enhancement provided by nanoantennas, which is shown to include factors relating to the antenna's material and to the antenna's geometry. We then simulated the response of typical structures and found that they lie several orders of magnitude away from the bound. In the case of spheres, we showed that periodic structures can outperform isolated structures only under certain geometrical conditions. This study paves the way for the definition of performance metrics that can be used for further optimization of SERS substrates.

Thesis Supervisor: Juejun Hu
Title: Associate Professor of Materials Science and Engineering

Acknowledgments

As the saying goes, it takes a village... particularly to get a PhD. In research, around research, outside research – all along the way I have had the utmost chance to be surrounded by people without whose support this five-year endeavor would simply not have been possible. I would like to use this opportunity to recognize all of them.

I would first like to express my deepest gratitude to my advisor, Prof. Juejun "JJ" Hu, for providing me with the unique opportunity to do research in his group. I was fortunate to benefit from his constant guidance and unwavering support throughout my work. Whatever the results, good or bad, he always had both motivating words and suggestions on how to improve. Under his supervision, the PMAT (Photonic MATerials) group has become the perfect environment for all of its members to thrive. I am notably very thankful for the freedom he has given me to engage in activities not directly related to research, such as teaching and taking classes. I often say, thinking back to the decisions of committing to pursuing a PhD and choosing an advisor, that I didn't really know what I was doing and that my choices were fairly ill-informed – but ever since I couldn't have been more glad that I chose to join JJ's group.

I would like to thank my committee members Prof. Polina Anikeeva and Prof. Silvija Gradečak for their helpful suggestions and direction during committee meetings and the preparation of this thesis. Their mentorship proved very valuable along the (long) way that is a PhD, as it is very easy to focus on the details and forget about the broader impacts of projects on which we work every day. Their guidance ensured that I didn't lose sight of the bigger picture.

I am also very grateful to my collaborators, starting with Prof. Xinqiao Jia and Sarah Geiger from the University of Delaware. It was a pleasure working on a project with a reach beyond optics, and Sarah did an amazing job at constantly bridging the gap between optics and biology. She explained to me her needs from a biology standpoint, while thanks to her multidisciplinarity we could also discuss processing and optical design. Our project kept me busy and worried for most of my PhD, and additional pressure from a demanding collaborator could easily have made this a situation difficult to sustain. Yet Sarah was always patient and compassionate whenever we would encounter issues. I also had the chance

to work on the Raman limits project with Prof. Steven Johnson from the Department of Mathematics at MIT, Prof. Owen Miller from the Department of Applied Physics at Yale, and Prof. Johnson's students Mohammed Benzaouia and Wenjie Yao. I deeply appreciate the trust Prof. Johnson and Prof. Miller put in me when they agreed to let me lead this project originating from their research. Mohammed's and Wenjie's help was most welcome as I ventured on topics outside of my usual area of work.

The PMAT group has been a wonderful environment to work in, where stimulating discussions, selfless help, and pleasant company make up the day-to-day life of the group. I am thankful to all of its past and present members for creating and perpetuating this atmosphere. With everyone, be they former or current PhD students, post-docs, visiting students, I had the chance to interact, sometimes collaborate, and always learn from their experience and expertise. Here I cannot but single out Derek Kita whose drive and enthusiasm for photonics research undoubtedly contributed to growing and sustaining mine, through our formal joint work on on-chip Raman sensing as well as our countless informal discussions over five years about anything and everything related to science and research – which actually extended beyond the laboratory (*vide infra*).

This work also owes a tremendous amount to many people who surrounded me in and around the laboratory. I cannot thank enough the staff at MIT and Harvard, for the care they take of the machines my work relied on, their patience in training me, their responsiveness whenever an issue arose, their help and advice in processing, and the overall positive atmosphere they created around the labs. In that regard, I would like to extend special thanks the staff and community of MTL, where I performed most of my work. In particular, my deepest respect and gratitude goes to Kurt Broderick and Mark Mondol, in charge of EML and the electron-beam lithography facilities respectively, who were always available to fix a problem, discuss a processing issue, and generally chat merrily.

I would also like to express my gratitude to the broader community in and around MIT that made these 5 years an amazing experience beyond research. Being a Teaching Assistant for 3.091 with Prof. Jeffrey Grossman, Laura von Bosau, the entire 3.091 staff through the years, and all the students I interacted with, was undoubtedly one of the most fun and rewarding experiences of my time here. Teaching 3.003-3.004 with Prof. Lionel Kimer-

ling introduced me to laboratory teaching, and gave me the unique opportunity to discover Japan. The ability to take Finnish classes through Harvard was a dream come true and I cannot thank Saana McDaniel enough for her dedication to teaching her language, her patience, and her seemingly endless joyful mood. Russian classes were also a defining feature of my time here in large parts thanks to Maria Khotimsky, whose kindness and dedication to her students are only matched by her excellent pedagogy. Thank you as well to Masha, Krista, and all the class and conversation partners I had the chance to practice speaking Russian and Finnish with through the years. MIT is full of great communities and I was fortunate to be part of some of them. Come to mind in particular the entire Department of Materials Science and Engineering, where I had the chance to be part of the Graduate Materials Council for 4 years, participate in several editions of MADMEC, and generally spend many many good moments; also the MIT Outing Club, which introduced me to the White Mountains, my home for so many weekends during these five years; and the MIT Rowing Club, that not only gave a meaning to my early mornings but also provided many fun and exciting moments everywhere from Cambridge to Asia.

A PhD is much more than a purely academic experience and in that respect I count myself as most lucky to have had wonderful friends by me all along this journey. In no particular order: Owen, Derek, Jonathan, Seth, Kevin, Elena, Constance, Alex, Pablo, Claire, Mark, Johannes, Masha, Sylvain, June, Lina, Corentin, Olivia, Joe, Hofi, and everyone who was a part of this journey – it was a chance to be able to count you as flatmates, hiking and/or skiing and/or concert partners, friends with whom to travel, have dinner, or just hang out and chat. I also know first-hand how difficult it is to stay connected to people who are far away and therefore I am incredibly thankful to my friends from France for not letting distance take its toll on us, most notably all the *tazons* from the Polytechnique rowing team, and Joséphine. Being surrounded by such incredible people is in great part, if not entirely, what makes me strive to outdo myself in everything I do, in research as well as in sports, from cooking dinners for/with you to trying to make you laugh – in life in general. I couldn't ask for more than your continued companionship.

This also applies to my parents and family, to whom this work as well as everything that lead me to this point owes a lot. Not only am I constantly inspired by what every single one of them, Papa, Maman, Antoine, Perrine, has accomplished and keeps on accomplishing,

but I am also very conscious and grateful for the chance they have given me to evolve in such a fostering and supportive environment: for example, I still have vivid memories of my dad explaining to me the balance of forces on a rocket at take-off as I was about 10 years old, or of my mom teaching me percentages and fractions with candies. I may not have become a rocket scientist nor a mathematician but this always-stimulating yet never-pressurizing atmosphere undoubtedly contributed to, if not generated altogether, my love for science and carried me all the way here. Merci pour tout !

Contents

List of Figures

List of Tables

THIS PAGE INTENTIONALLY LEFT BLANK

Chapter 1

Introduction

1.1 Flexible integrated photonics[1]

Photonics, the science and technology of manipulating light, is now a well-established field most notably playing a major role in information and communications technology (ICT). While still researched mainly as an alternative to electrical circuits in ICT, photonics is increasingly penetrating into other emerging application areas such as biotechnology and healthcare. Integrated photonics in particular presents features that make it a unique platform for example for *in-vitro* or *in-vivo* sensing: it combines small form factor, low power consumption, robustness, large multiplexing capability, and tight optical confinement that allows for strong light-matter interactions. However, conventional integrated photonic devices are inherently rigid and two-dimensional because of the substrate on which they are fabricated – whereas the world isn't flat and stiff. This prevents integrated photonics from being used in applications that would otherwise benefit from its features. For example, traditional rigid, planar devices are not compatible with the soft, curvilinear surfaces of living organisms [6]. This mismatch demands flexible and stretchable devices that can be mechanically deformed (bent, folded, twisted, stretched or compressed) without damage to their optical properties.

By imparting mechanical flexibility to devices, structures that were fabricated in two dimensions can be made three-dimensional, thus enabling both the extension of traditional applications to non-planar geometries, and novel functionalities that cannot be attained

[1] Our work on this topic will be included in a review paper entitled: "Flexible integrated photonics: what's already on the table, and what's next?".

with planar devices. The successes of flexible electronics over the past two decades have well established the benefits of flexible devices: amenability to large-area, low-cost fabrication via roll-to-roll processing [7–10], and conformal integration with curvilinear surfaces and biological tissues [6, 11]. Thanks to novel materials and designs [12–14], numerous components were demonstrated, including metal routings [15], transistors [16, 17], wireless transmitters [18, 19], batteries [20, 21], photodiodes [22], and LEDs [23, 24].

Flexible photonics has emerged in an effort to provide the same deployment flexibility to optical systems. Flexible photonics brings additional features to the table. Compared with electronics (which we take to include free-space optoelectronic components such as LEDs and photodiodes), it presents the advantage of allowing for an enhanced control of light propagation and light-matter interaction, which translates to light delivery with minimal loss and cross-talk. Its large multiplexing capability results in a smaller footprint for devices. It also differentiates itself from fiber optics by its manufacturing scalability and a tight optical confinement that allows for strong light-matter interactions. Complex geometries without axial symmetry can, notably, be readily defined in high-volume production of flexible photonics, but are not possible in fiber optics.

To date, demonstrations of flexible integrated photonic devices include systems conformally integrated on curved surfaces, optical interconnects and solutions for optical packaging, strain sensors, and strain-tunable devices. Applications of conformally integrated optical devices with unconventional substrates range from sensing [25, 26] to imaging and cloaking [27, 28]. Conformal metasurfaces in particular have attracted interest thanks to their ability to control arbitrarily the phase, amplitude, and polarization of an incident beam [29, 30], thereby enabling decoupling of the optical functionality and substrate geometry, which traditional conformal free-space systems cannot do [31]. The efforts around flexible optical interconnects [32–36] have been driven by the many promises of this technology: it provides a scalable, high-bandwidth, high-density platform through single-mode waveguides, offers the possibility to stack up multiple sheets to further increase the density [33, 37], has the ability to accommodate misalignment [38] and increases the degrees of freedom for sub-assembly designs [32] thanks to its mechanical flexibility. The strain-optical coupling linking device deformation and optical response has enabled sensors with high sensitivity and multi-directional sensing capabilities [2, 39], as well as strain-tunable resonant structures, adjustable metalenses, and strain-switchable metasurfaces [30, 40, 41].

A few challenges remain that still prevents flexible integrated photonics from benefiting from the same widespread use as flexible electronics. The range of available geometries is limited by the fabrication techniques. Most devices are fabricated as a continuous layer (or stack of layers) and used as such after conformal integration, whereas many geometries cannot be obtained by deforming (however much) a sheet. Methods to realize truly 3-D devices suffer from limited resolution or choice of materials. In addition, most of the existing design approaches for stretchable and flexible devices do not take into account stress-induced strain-optical coupling during the fabrication and integration processes. Yet considering these effects is essential to decoupling optical functionality and substrate geometry and enhancing light-matter interactions. Therefore, a wholistic design approach that properly accounts for such an optical property change due to deformation is necessary for optimal device design.

1.2 Stress sensing in soft materials

Mechanical constraints play an important role in biological systems, as they are involved in e.g. cell migration [42, 43] and differentiation [44], wound healing [45–47], and tumor progression [48]. Measuring stress or strain at the cellular level is therefore critical to the understanding of these processes. However, *in-situ* stress measurement in environments as soft as cell cultures imposes several constraints which preclude the use of traditional methods. Conventional force gauges used for building structural health monitoring suffer from the enormous difference in elastic moduli between the soft matrix (generally in the range of MPa, e.g. some elastomers, to hundreds of Pa, e.g. hydrogels) and the sensor material (typically over 10 GPa for metals, ceramics and semiconductors, out of which most stress sensors are made). This difference causes a highly inefficient strain transfer from the soft material to the stiff sensor, which needs to be compensated by an increased sensitivity of the sensor. Issues also arise due to the mere presence of the sensor in the soft matrix as the large elastic mismatch between the structure and the tissues can cause perturbations to the local microenvironments. A too large elastic mismatch could even result in undesired tissue reactions such as glial scarring and tissue encapsulation [49]. The sensor structure should therefore be mechanically compliant in order to both maximize the stress transfer and minimize the perturbations to the system.

Several approaches have been explored for stress monitoring in soft matter and particularly in biological systems such as cell cultures. The most popular technique is probably traction-force microscopy (TFM), which relies on the idea of tracking the deformation of the external medium to infer the action of cells [50–54]: microscopic markers, typically microspheres, are incorporated in a transparent matrix to create a discernable optical contrast. As the matrix deforms as a result of cellular force due to the embedded cells, the markers are optically tracked, which enables to spatially resolve displacement and deduce mechanical strain using dedicated imaging processing algorithms. The small sizes of the markers (typically <1 µm) allows for high spatial resolution. Again, this approach is limited to the study of transparent materials. It also suffers from the need for advanced microscopy equipment and analysis software, and careful processing of the data to get high-quality displacement fields. Another method infers the local strain distribution by monitoring the deformation of patterned hydrogel or elastomeric thin film microstructures (e.g., micro-pillars or cantilevers) [55–58]. The small size of the patterns allows for high spatial resolution, while the force sensitivity can be tailored by engineering the substrate's mechanical properties. This also offers the possibility to provide various mechanical environments, including rigidity gradients. However, the discrete nature of the cell-to-sensor contact points influences the cell's behavior. The system under study is also required to be transparent, such that the displacement of the pattern can be optically monitored to calculate the forces that caused it. A similar technique relies on molecules such as DNA hairpins or proteins instead of inert biomaterials to detect and measure forces [59–61]. These molecular sensors benefit from enhanced specificity thanks to the chemical link with the sensing molecules, yet suffer from the same previously transparency and localization drawbacks. More broadly, these techniques remain largely applicable only to measurements in a 2-D plane. This is problematic as cells do not behave similarly in 2-D and in 3-D, therefore 2-D measurements cannot be used to infer information about what goes on in 3-D environments.

A few 3-D techniques have been developed to mitigate this issue. Many of the early efforts relied on 2-D structures flexible and stretchable enough to be conformally integrated with curvilinear systems. As part of a larger push towards the realization of "electronic skin" or e-skin, epidermal stress sensors using flexible thin film strain gauges have been realized, often made of a thin silicon, polymer, piezoelectric ceramic, or nanotube membrane embedded in an elastomeric film [62–65]. The limited resolution of these devices is compensated

by their ease-of-use and the ability to monitor large samples. Yet curvilinear shapes are only a very limited subset of 3-D geometries. 3-D printed flexible strain gauges have been demonstrated [66], but the coarse printing resolution results in large sensor sizes that limit the sensor density and spatial resolving power. 3-D scanning confocal microscopy offers another powerful tool for 3-D stress measurement, for example in the case of 3-D TFM (where the microspheres are embedded in a 3-D matrix in which the cells grow) [50, 67, 68]. Yet just like its 2-D counterpart, its utility is limited to transparent and optically homogeneous materials as optical scattering inevitably leads to image quality degradation and cross-talk with out-of-focus light. Computational treatment of the output data is also all the more challenging in 3-D. Using a similar principle to TFM, digital volume correlation (DVC) is a method consisting in relying on images of the sample (instead of embedded markers as in TFM) at different times to reconstruct its deformation and calculate the forces at play [69–71]. Images might be generated through a variety of techniques such as magnetic resonance imaging (MRI) or optical coherence tomography (OCT), depending on the system's requirements. Provided the images are of sufficient quality, very high precision can be reached, yet once again at the cost of computationally expensive and time-consuming post-processing, thus preventing the large-scale usage of these methods in biological laboratories. The performances of all the above-mentioned methods are summarized in Table 1 where it can be seen that every method proves unsatisfactory in some way: it either doesn't provide 3-D information, and/or is limited in its spatial extent, and/or requires complex post-processing.

In summary, a general multi-point 3-D stress measurement technique for soft materials remains an unmet need. For the specific case of cellular force measurement, standards are set by the characteristics of a single cell: it exerts from hundreds of piconewtons to tens of nanonewtons of force and measures tens of microns. While single-cell resolution isn't necessarily required when monitoring entire cell cultures, a practical stress sensing method for cell culture monitoring would nonetheless need to detect the effects of small cell clusters of about a dozen cells. Desirable performance levels would thus be a force sensitivity in the nanonewtons range, a spatial resolution of 100 µm, a sampling frequency of one measurement per minute, and a sampling volume of several cubic centimeters to allow for realistic *in-vitro* conditions.

Method	Dimensionality	Force resolution	Spatial resolution	Transparency?	Sampling volume	Speed	Complexity
Requirements	3D	<100 nN	<100 µm	No	cm^3	sec	Low
2-D TFM	2D	1 nN	1 µm	Yes	mm^3	min-hours	High
Flexible gauges	2D	10 µN	10 µm	No	cm^3	sec	Low
Micro-pillars	2D	0,01-100 nN	1 µm	Yes	mm^3	sec	Low
Molecular sensors	2D	1-10 pN	10 nm	No	mm^3	sec	Low
Collagen gel	3D	10 µN	-	No	mm^3	sec	Low
3-D TFM	3D	10 nN	1 µm	Yes	$< mm^3$	min-hours	High
DVC	3D	0,01%	1 µm	No	mm^3-cm^3	hours	High

Table 1.1: Comparison of the performance of currently available methods for mechanical sensing at the cellular or few-cells scale.

1.3 Surface-enhanced Raman spectroscopy

Perhaps the most unique feature of optical sensing is the ability to perform label-free chemical identification through spectroscopy. By accessing information about the molecular energy levels that are specific to each chemical, one can uniquely determine the chemical composition of an unknown mixture, both qualitatively and quantitatively. Spectroscopy comes in many declinations depending on the nature of the interaction between the incoming energy and the material of interest. In Raman spectroscopy, the incoming ("pump") light excites electrons from their ground energy state to virtual states, from which they instantly relax back to a ground state, thereby emitting a photon. If they relax to the same level they started from, this process is called Rayleigh scattering and doesn't yield any information about the molecule. If they relax to levels above or below their original level (see Figure 1-1(b)), the frequency of the emitted photons are slightly shifted compared to this of the pump photons. This shift is molecule-specific and therefore allows for identification of the molecule. These processes are called Stokes and anti-Stokes scattering, respectively.

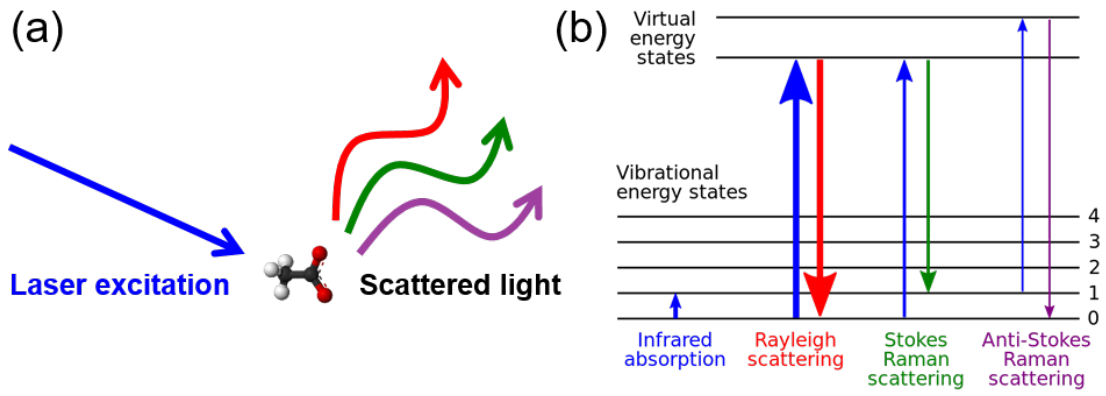

Figure 1-1: (a) Schematic principle of Raman spectroscopy. (b) Energy level diagram showing the electronic transitions involved in Raman spectroscopy. From [1].

A major drawback of Raman spectroscopy is however the very low magnitude of the Raman cross-section of most chemicals: the Raman radiation emitted by a material is traditionally on the order of 0.001% of the power of the pump signal [72], that is, 1 million pump photons are on average required for 1 Raman-shifted photon to be emitted. This poses challenges in concentrating the pump laser, collection of the Raman light, and filtering. Several methods have been developed in order to increase the Raman signal. In surface-enhanced Raman spectroscopy (SERS), the chemicals of interest are placed in contact with or in the vicinity of a surface, typically metallic nanoparticles. These particles interact with the electromagnetic radiation and act as antennae concentrating the incoming pump light and radiating the emitted Stokes signal [73, 74]. Chemical enhancement through charge-transfer mechanisms also plays a role, although its contribution is weaker than the electromagnetic enhancement effect [75]. Overall, efficiency up to 12 orders of magnitude larger than this of traditional Raman have been demonstrated, allowing for detection levels down to the single molecule [76, 77] and opening up applications in the fields of e.g. biochemistry, forensics, food safety, threat detection, and medical diagnostics. Many different materials and antenna geometries have been used for such measurements [74, 78] : metals such as silver, gold, or copper, dielectrics such as silicon carbide or indium tin oxide, were implemented in various shapes such as spheres, bowties, or cones, either by themselves or in arrays. Eventually, the choice of a particular substrate (materials and geometry) is dictated by the compatibility with the analyte, the fabrication constraints, the excitation laser (visible or near-infrared

(IR) are typically used), and naturally the expected enhancement, which is often correlated to all of the previous factors. Maximizing the enhancement under a given set of constraints or for particular applications has naturally been the goal of many efforts [79,80], with the aim of improving over current designs. However, no study so far has looked at how much could the current designs even be improved. Whether a maximum exists, what its value is, and how do current substrates compare to that maximum, would greatly inform future optimization efforts, notably by concentrating on designs with the greatest room for improvement.

1.4 Thesis outline

This thesis work aimed at advancing the field of photonic sensing by demonstrating novel devices and applications and improving the performance of current sensors. Chapter 1 reviews the progress and challenges faced by flexible integrated photonics while underlining the need for additional capabilities through a review of current methods for stress sensing in biological systems. We also present the principles and motivation for surface-enhanced Raman spectroscopy.

Chapter 2 introduces the 3-D flexible integrated photonic device used as a stress sensor for soft materials. After presentation of the general idea of the device, we explain the physical mechanisms underlying the key properties of the device: stress-optical coupling that allows for stress sensing by optical measurement, and large-deformation buckling of a beam with uniform or piecewise constant cross-section for deterministic control of the position of the sensors.

In Chapter 3, a proof-of-concept device is experimentally demonstrated. We first justify the choice of a set of materials and processing route and give the details of the fabrication process. Keeping in mind the intended use of the device in a biological laboratory, we then discuss practical problems we encountered and solutions we developed: the device needs to be robustly packaged and must be able to distinguish between the contribution due to stress and these due to temperature and illumination variations. We also discuss different resonator design to allow for multiplexed measurements.

Chapter 4 details the calibration process of our device. It must involve knowing both the stress and the optical shift in order to extract the relation between the two, which can then be used in subsequent measurements to infer unknown stresses from optical data. We

therefore present mechanical simulation results to deduce the strain and optical measurement results to get the optical shift. In an effort to increase the calibration precision by eliminating coarse geometrical measurements, a method relying only on optical measurements is introduced. Finally, we look at the factors influencing the sensitivity of our device and calculate the minimum resolvable strain. This allows us to benchmark our solution with respect to previously available methods described in Section 1.2.

Chapter 5 focuses on calculating and approaching a bound to the Raman response of metallic nanoparticles, as used in surface-enhanced Raman spectroscopy (SERS). We first review the concept of local density of states (LDOS) and the previous findings on a bound to that quantity. We then build on these LDOS bounds to derive a bound for Raman enhancement, by decomposing the Raman process into three subsequent steps. In order to simulate the response of nanoparticles and compare it to our bound, the scuff-em package is introduced. Simulating typical nanoparticles used in SERS shows that they remain far from the bound and that optimization is therefore possible. In order to assess the effect of adding periodicity to the SERS structure, we derive a periodic Raman limit and come up with a condition for a periodic array of spheres to outperform a single sphere.

In conclusion, Chapter 6 summarizes the findings of this thesis and presents several ways to build upon this work, by e.g. adding new functionalities to our 3-D photonic sensor platform or introducing new materials. Further calculations and simulations could extend the reach and practical impact of our Raman limits.

THIS PAGE INTENTIONALLY LEFT BLANK

Chapter 2

Proposal of a three-dimensional photonic sensor array

2.1 Device description

We propose a device that fulfills the requirements outlined in Section 1.2 for a strain sensor for soft materials. Our device consists in a 3-D array of optical stress sensors placed at different locations within a soft matter system, as illustrated on Figure 2-1. Optical waveguides are encapsulated in a thin, mechanically compliant, and biocompatible polymer structure made of buckled strips between two larger, flat "islands". This structure is fabricated in 2-D and then deterministically deformed into the desired 3-D geometry. Once fabricated, the compliant 3-D device can be embedded in the soft matrix of interest. The actual sensors are optical resonators positioned along the waveguides. Mechanical stress can be detected thanks to the strain-optical effect, which couple local strain and optical properties, enabling a measure of the strain at the sensor's location.

This approach yields several advantages. It minimizes disturbance to the surrounding environment thanks to the mechanical compliance of the buckles and their small size (few microns in width and thickness). It is also readily scalable to a large number of sensors by adding additional channels, or buckles, to a single device. Furthermore, since light is delivered to the sensors through waveguides, it is not limited by the matrix's transparency, allowing for measurement at any depth in any material.

There are three conditions for this device to work as desired: 1) the device must be

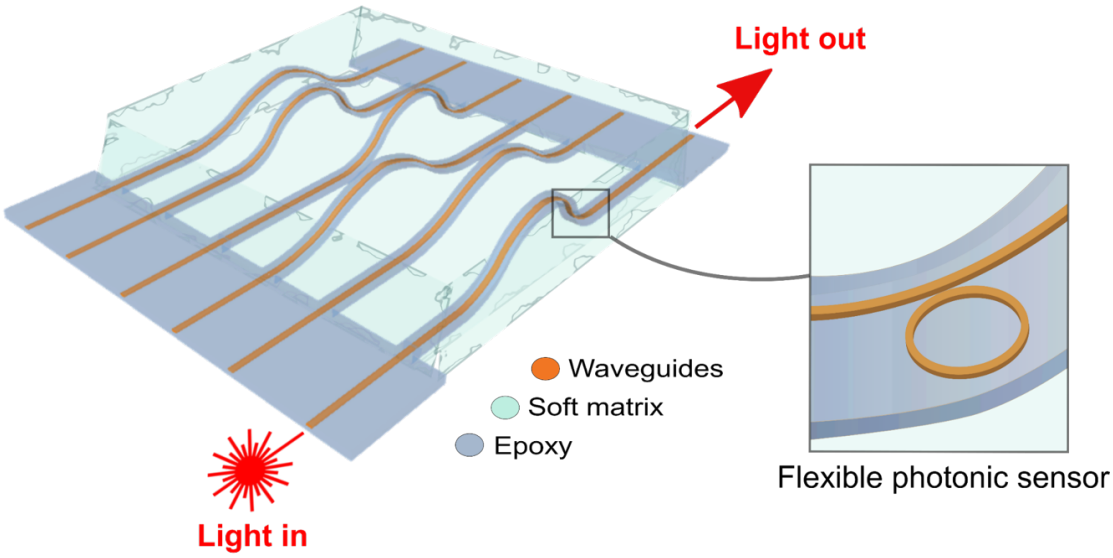

Figure 2-1: Schematic of the proposed 3-D photonic sensor array embedded inside a soft material matrix. Optical resonators placed along the waveguides are the actual sensors.

made in 3-D with the sensors located at the points of interest, 2) it needs to be amenable to integration with the matrix of interest, and 3) interrogating the sensor (optical measurement) must yield information about the local stress in the soft matrix. These are the topics of the following sections.

2.2 3-D position control by deterministic buckling

2.2.1 Buckling for realization of 3-D integrated photonics

For our device to yield useful information, we must be able to choose and control the 3-D position of the sensors. Yet none of the currently available 3-D (or assimilated) fabrication methods for integrated photonics fits our needs. So-called 3-D photonic multilayer devices, made by stacking optical components in layers, remain inherently planar and do not allow for seamless integration with an external matrix, as they either are made of solid layers or leave little space available. Likewise, bendable or stretchable membranes such as "e-skin" can be deformed into various 3-D shapes but would either remain on top of the matrix, or cut it in separate regions. 3-D printing technologies are capable of almost arbitrary 3-D shapes but are limited by their resolution (sub-micron features are required for integrated photonics) and the choice of materials, notably high optical index materials

required for small footprint and . Their throughput is also much lower than conventional 2-D processing through lithography. Buckling of 2-D structure after fabrication or transfer onto an elastomeric substrate has been demonstrated as a powerful way of creating many different 3-D shapes [81]. The challenge in directly translating this method to photonics lies in the large coefficient of thermal expansion (CTE) mismatch between elastomers and common optical materials (e.g., the CTE of PDMS is 310 ppm/°C whereas the CTE of TiO_2 glass is 9 ppm/°C). Advanced fabrication optimization [82] or transfer-printing of the optical materials are therefore needed, making fabrication more involved.

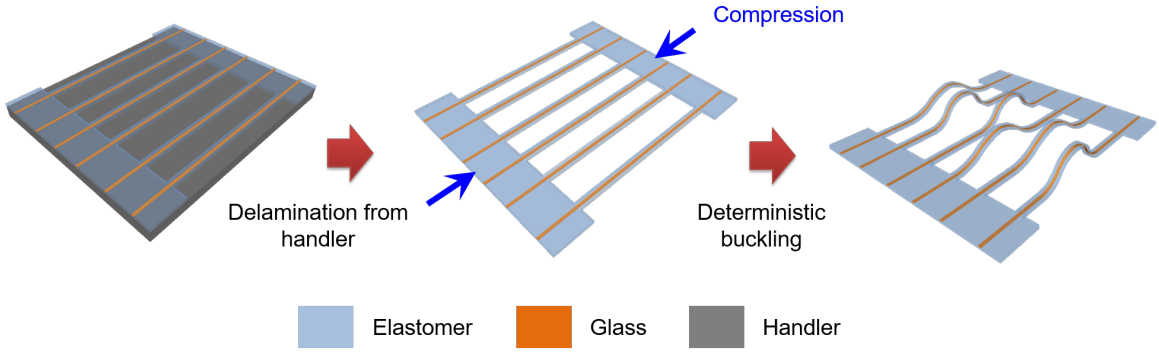

Figure 2-2: Schematic fabrication process flow of the buckled 3-D photonic structure.

We propose to adapt the 2-D-to-3-D buckling method to photonic devices, as this method offers three key advantages. First, it leverages mature planar processing technologies that allows for fabrication of high-quality optical components. Second, it is readily scalable to a large number of sensing channels, simply by changing the dimensions of the device (strip width, strip spacing, device overall width, etc.) without compromising the quality and throughput of fabrication. Third, it enables construction of 3-D architectures by controlled, deterministic mechanical deformation – much like pop-up books come under a planar form that is then deformed into the desired 3-D object. The fabrication process is illustrated on Figure 2-2. The entire photonic device, with its lower cladding, optical components (waveguides, resonators, couplers, etc.), and upper cladding, is fabricated on top of a rigid handler substrate. Because the device is made on a rigid substrate instead of a pre-strained elastic substrate for the need of the photonic fabrication, it is then delaminated from the handler in order to be compressed and form a 3-D structure. The exact shape of the buckled strips is precisely controlled by the thickness profile of the strip and the relative displacement of the two ends during compression, as we will demonstrate in the following sub-sections for

the 1- and 2-thickness cases. The freedom in available buckle shapes and in location of the sensors (resonators) along the buckle translates to the ability to place sensors at arbitrary 3-D locations – our stated goal. Experimental details of this fabrication process are the subject of Section 3.2. Once the 3-D sensor has been fabricated following the process of Figure 2-2, it can easily be integrated with the material of interest using the process depicted on Figure 2-3: a well is placed around the sensor structure, and the material to study is poured into the well and around the 3-D structure, thereby embedding the sensors.

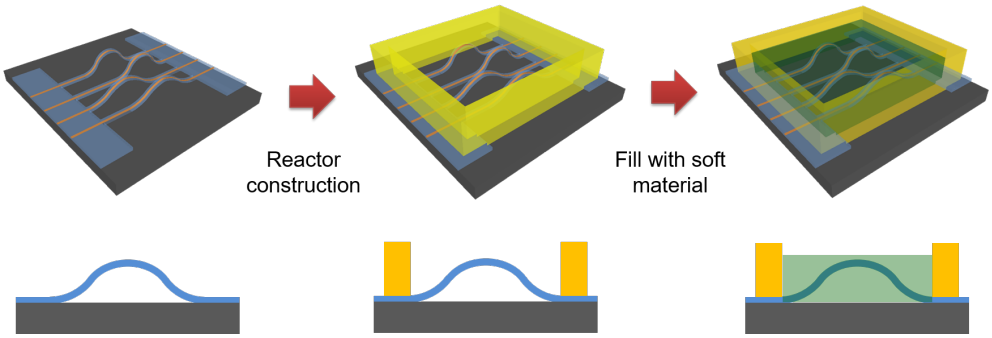

Figure 2-3: Schematic integration process flow of the 3-D sensor with a material of interest.

The buckling of a strip (typically called a "beam" in mechanics) has been studied since Euler in the 17th century and solved in a number of specific cases [83]. Our case corresponds to the buckling of a beam with uniform or piece-wise uniform thickness (i.e. cross-section) while controlling the position of its ends, as well as the tangent at the ends – also called "fixed ends". This configuration is represented on Figure 2-4 with the geometrical notations used in the following sub-sections. There we show that, given parameters that we control such as the buckle's total length and span, we can predict the shape of the buckle and therefore its curvature, which can be directly related to the strain experienced by the embedded resonator. The assumptions made throughout the derivations are as follows:

- The material of the beam is homogeneous and isotropic. Previous work in our group has shown that the presence of the glass could be neglected [2].
- The compressive load on the beam is axial only.
- The beam is free from initial stress.
- The weight of the beam (and any other lateral load) is neglected.
- The stress never exceed the yield strain.

The following notations are also used:

x: horizontal coordinate of points of the beam

h: vertical coordinate of points of the beam (i.e. height profile of the beam)

α_0: angle of deflection of the buckle

s: arc length along the buckle

L_{tot}: total length of the beam

L: length of the beam along the x-direction after buckling

E: Young's modulus of the beam material

I: moment of inertia of the beam (for a given cross-section). In particular, for a beam with rectangular cross-section of width w and thickness t, its moment of inertia with respect to its neutral axis is $I = wh^3/3$.

F: load applied at the end of the beam

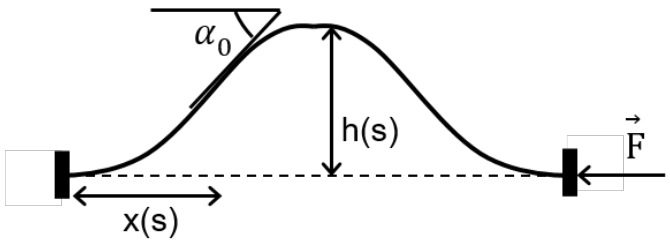

Figure 2-4: Schematic side-view of a uniform cross-section buckle. The notations are defined in the text.

2.2.2 Uniform cross-section beam

The shape of a uniform cross-section beam under buckling is typically solved using a small-deformation approach. The boundary conditions on the position and tangent at each end are:

$$\begin{cases} h(0) = h(L) = 0 \\ h'(0) = h'(L) = 0 \end{cases} \tag{2.1}$$

Based on these conditions, the end result of the derivation is a simple equation for the height profile:

$$h(x) = A\left[1 - \cos\left(\frac{2\pi}{L}x\right)\right] \tag{2.2}$$

where A is a constant whose value is given by the condition on the total length:

$$L_{tot} = \int_0^L \sqrt{1 + h'(x)^2}dx = \int_0^L \sqrt{1 + A^2\frac{4\pi^2}{L^2}\sin^2\left(\frac{2\pi}{L}x\right)}dx \tag{2.3}$$

Given the shape, the curvature can be calculated using the formula:

$$\kappa(x) = \frac{1}{R(x)} = \frac{h"(x)}{[1 + h'(x)^2]^{\frac{3}{2}}} \tag{2.4}$$

Plugging in actual numbers (our current design uses $L_{tot} = 10$ mm and $L = 7$ mm) yields $A = 1.66$ mm. The corresponding buckle shape and curvature are plotted on Figure 2-5(a). We however realized that these curves did not describe well the buckles obtained experimentally, shown on Figure 2-5(c). Going back and examining the hypotheses made, the small-deformation approach is based on d^2y/dx^2 representing the curvature of the beam. For this to be valid, we need to have $L \approx L_{tot}$, which isn't the case for us.

In the large-deformation approach, the curvature is described by its exact expression $d\alpha/ds$, with α the angle of deflection of the beam at each position. This modifies the differential equation governing the behavior of the beam [84]:

$$EI\frac{d^2\alpha}{ds^2} + F\frac{dh}{ds} = 0 \tag{2.5}$$

The value of F is unknown but will be determined later on. The profile of the buckle is then given by:

$$\begin{cases} x(\phi) = \dfrac{1}{k}\left[2E(\phi, p) - F(\phi, p)\right] \\ h(\phi) = \dfrac{2p}{k}\left[1 - \cos(\phi)\right] \end{cases} \quad for\ 0 \leq \phi \leq 2\pi \tag{2.6}$$

where $k^2 = F/EI$, $p = \sin(\alpha_0/2))$ with α_0 the angle of deflection at the inflection point, and $E(\phi, p)$ and $F(\phi, p)$ are the incomplete elliptic integrals of the second and first kind, respectively. The boundary conditions used to obtain these expressions are the same as in Equation 2.1.

The values of k and p are found by considering two additional conditions: the total

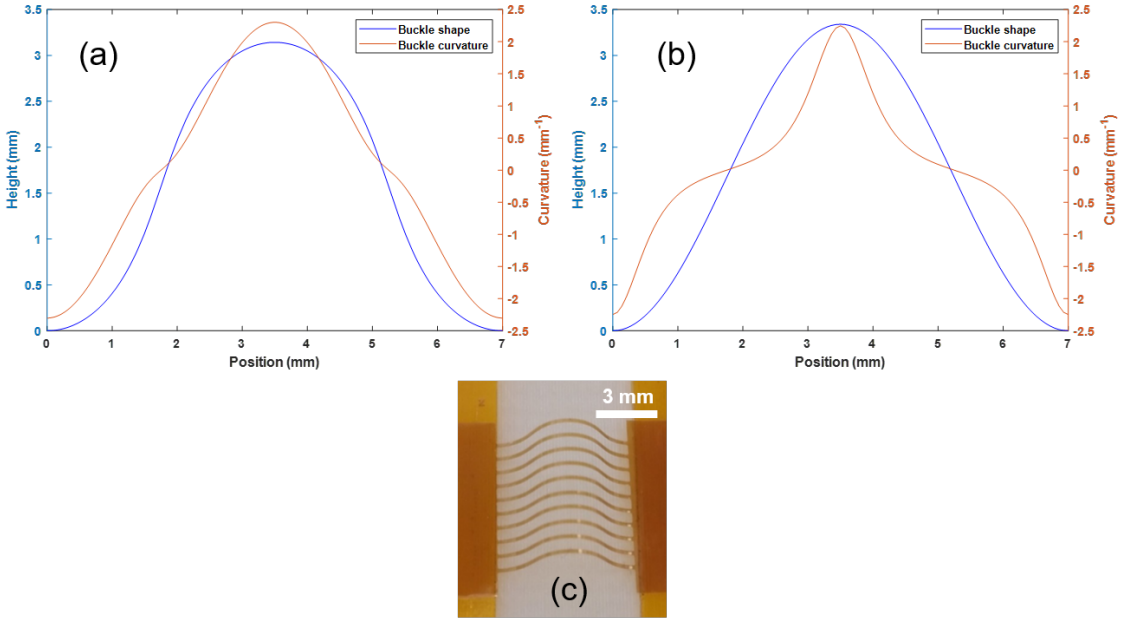

Figure 2-5: (a) Buckle height profile and curvature as calculated within the small-deformation approximation. (b) Buckle height profile and curvature as calculated with the large-deformation approach. (c) Actual buckles. The red color is due to a thin layer of glass remaining between the two polymer layers.

length L_{tot} of the device is conserved upon buckling, and the position $x(2\pi) = L$ of the right edge of the buckle is known. The total length of the buckle can be calculated as:

$$L_{tot} = \int_0^{2\pi} \sqrt{x'(\phi)^2 + h'(\phi)^2} d\phi \tag{2.7}$$

$$= \frac{4K(p)}{k} \tag{2.8}$$

where $K(p)$ is the complete elliptic integral of the first kind.

The conditions on k and p are therefore:

$$\begin{cases} L = \dfrac{1}{k}\left[2E(2\pi, p) - F(2\pi, p)\right] \\ L_{tot} = \dfrac{4K(p)}{k} \end{cases} \tag{2.9}$$

Because elliptic integrals have no analytical expression, this system needs to be solved numerically. Our design, with a total length of 10 mm and a span of 7 mm, yields $p = 0.5364$ (corresponding to a deflection angle $\alpha_0 = 32.4°$) and $k = 0.6827$ mm^{-1}. The profile and the curvature are plotted on Figure 2-5(b).

The need for the large-deformation equations is justified by the relative difference in calculated curvature between the two models: it is greater than 50% at some points, clearly demonstrating that the exact large-deformation model should be used.

2.2.3 Piece-wise uniform cross-section beam

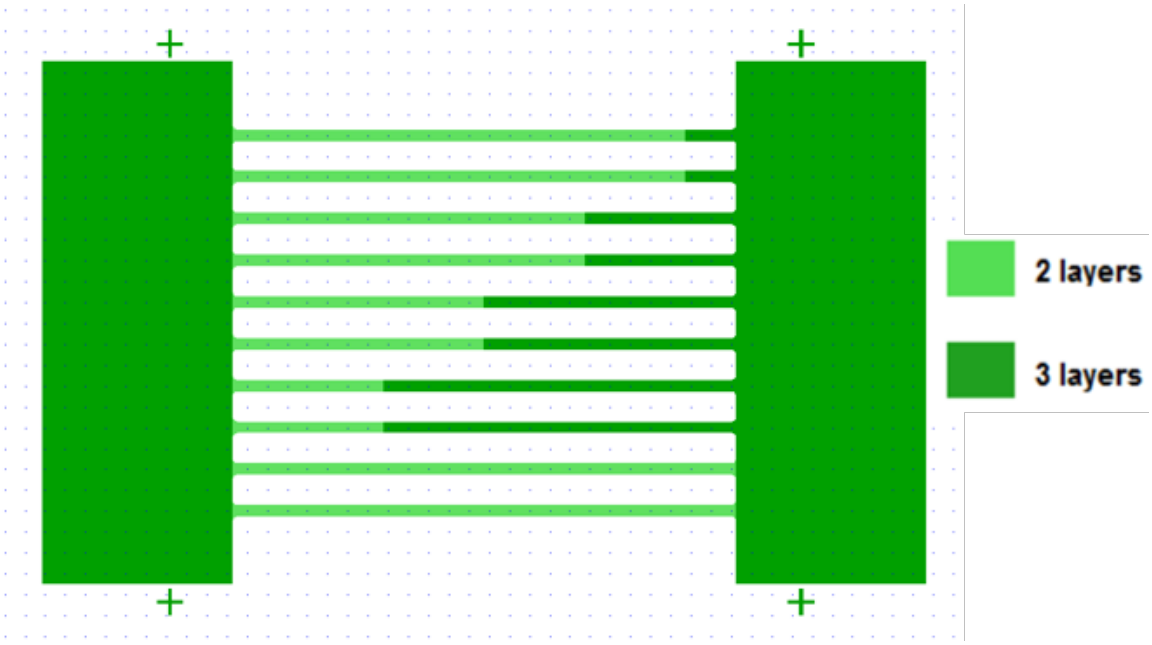

Figure 2-6: Mask file showing the thickness profile of the buckles in their planar configuration. The length ratios between the two segments are 1:9 (first 2 strips from the top), 3:7 (strips 3 and 4), 5:5 (strips 5 and 6), 7:3 (strips 7 and 8).

In the case of a constant cross-section, we showed in the previous sub-section that the shape was entirely determined once the final span of the buckle was chosen. It is thus the only degree of freedom. As the span is the same for all the buckles on a device, all of them end up with the same shape. Nonetheless, we want to be able to probe the full 3-D space and therefore need to be able to give different shapes to adjacent buckles.

To that end, we use thickness modulation of the strips. The thickness is simply controlled by the number and pattern of polymer layers used for encapsulation, as we will detail in Section 3.2. By using a 3rd layer on some areas of the strips but not others, as shown in the mask file presented on Figure 2-6, the cross-section and thus the moment of the inertia of the beam vary along its length. We show here that this case is also solvable analytically, and that it allows for many more buckle geometries. For the sake of simplicity, we detail

here the treatment for a beam made of only two segments of different thicknesses. Any more complicated case, with three or more segments of two or more thicknesses, could be solved in a similar way.

The two segments are described by their moment of inertia I_1 and I_2, and their length ℓ_1 and $\ell_2 = L_{tot} - \ell_1$. Solving Equation 2.5 for each segment yields two profiles of the form of Equation 2.6, for $0 \leq \phi \leq \Phi$ and $\Phi \leq \phi \leq 2\pi$, with Φ the (unknown yet) parameter giving the junction's position. We can write the horizontal position of the beam as:

$$x(\phi) = \begin{cases} \frac{1}{k_1}\left[2E(\phi, p_1) - F(\phi, p_1)\right], \text{ for } 0 \leq \phi \leq \Phi \\ \frac{1}{k_1}\left[2E(\Phi, p_1) - F(\Phi, p_1)\right] + \frac{1}{k_2}\left[2[E(\phi, p_2) - E(\Phi, p_2)] - [F(\phi, p_2) - F(\Phi, p_2)]\right] \\ \qquad\qquad\qquad\qquad\qquad\qquad\qquad\qquad\qquad\qquad \text{for } \Phi \leq \phi \leq 2\pi \end{cases} \quad (2.10)$$

Its vertical position is:

$$h(\phi) = \begin{cases} \frac{2p_1}{k_1}\left[1 - \cos(\phi)\right] & \text{for } 0 \leq \phi \leq \Phi \\ \frac{2p_1}{k_1}\left[1 - \cos(\Phi)\right] + \frac{2p_2}{k_2}\left[\cos(\Phi) - \cos(\phi)\right] & \text{for } \Phi \leq \phi \leq 2\pi \end{cases} \quad (2.11)$$

In both cases we used the continuity at Φ.

We have 5 parameters (p_1, k_1, p_2, k_2, Φ), we need 5 equations. These are given by the lengths of each segment, the boundary conditions at each end of the buckle, and the relation between k_1 and k_2 due to the force balance at the junction:

$$\begin{cases} \ell_1 = \frac{1}{k_1}F(\Phi, p_1) \\ \ell_2 = \frac{1}{k_2}\left[4K(p_2) - F(\Phi, p_2)\right] \\ x(2\pi) = L = \frac{1}{k_1}\left[2E(\Phi, p_1) - F(\Phi, p_1)\right] + \frac{1}{k_2}\left[2[4E(p_2) - E(\Phi, p_2)] - [4K(p_2) - F(\Phi, p_2)]\right] \\ h(2\pi) = 0 = \frac{2p_1}{k_1}\left[1 - \cos(\Phi)\right] + \frac{2p_2}{k_2}\left[\cos(\Phi) - 1\right] \\ \frac{k_1}{k_2} = \frac{I_2}{I_1} = \left(\frac{t_2}{t_1}\right)^3 \end{cases} \quad (2.12)$$

This system is then solved numerically. Sample buckle profiles calculated this way are shown on Figure 2-7(a) and (b). Figure 2-7(b) in particular demonstrates the ability to tune the shape of the buckle to access any desired point in the 2-D plane of the buckle. Figure 2-7(c)

presents an experimental demonstration of using thickness modulation to create different buckle shapes. As the length of the thicker segment is increased, the behavior predicted by Figure 2-7(b) is indeed observed, including the discontinuity at the junction between the two segments.

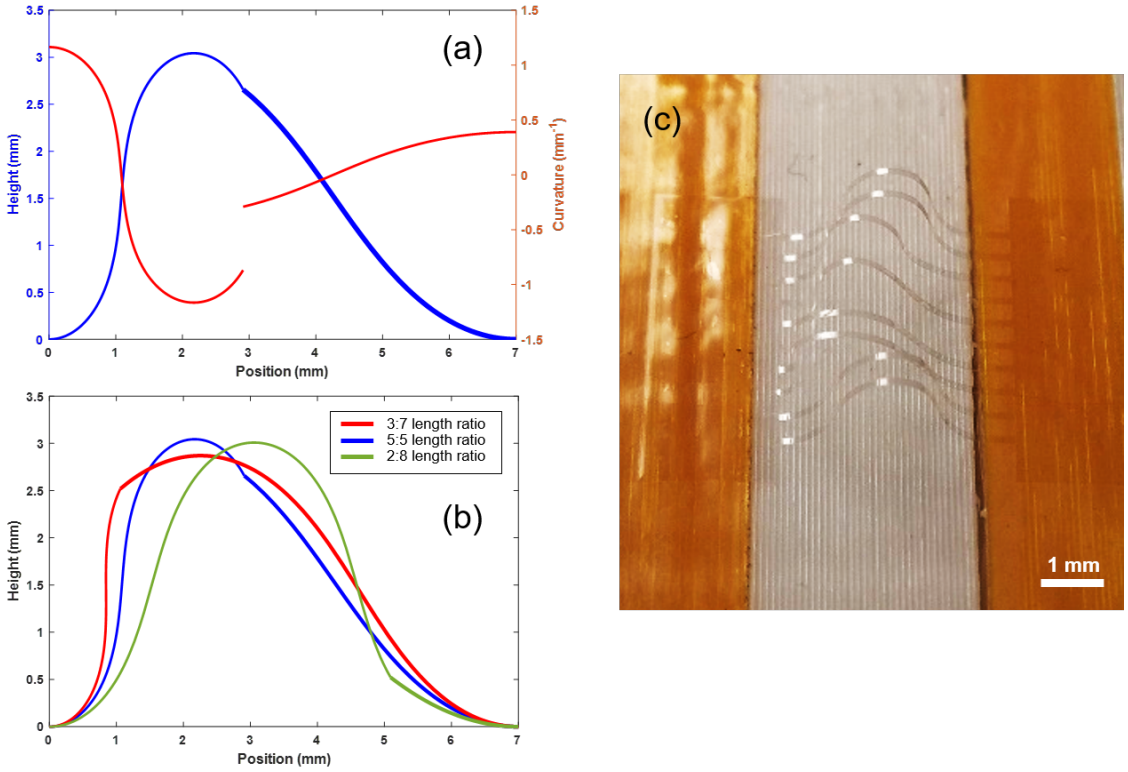

Figure 2-7: (a) Buckle height profile and curvature as calculated for a 2-segment beam, with 2 segments of length 5mm and thickness ratio 1.2 spanning 7mm. (b) Buckle height profiles for 2-segment beams of thickness ratio 1.2, spanning 7mm, with different thick/thin length ratios. (c) Actual sample fabricated using the mask of Figure 2-6.

The force balance at the junction causes a discontinuity in the derivative, which might seem counter-intuitive at first. This can be understood by considering the number of degrees of freedom for the system. Given the position and angle at each of its ends, each constant thickness segment has its shape entirely determined. In our case of two connected segments, the end where they join is free to move vertically and horizontally, making for 4 degrees of freedom. Continuity in both directions constrains two of those degrees. Force balance in both directions constraints the remaining two degrees. The angle therefore cannot be constrained to be continuous at the junction, as this would result in an overconstrained system. The same approach can be used for beams with more segments by applying the

continuity conditions (last equation in Equation 2.12) at each junction, and solving the resulting system for p, k, and Φ of each segment.

2.3 Stress sensing by optical measurement[1]

The ability to detect stress, or equivalently strain, through optical measurement is based on the strain-optical coupling that takes place at the optical resonator's location. Strain (or equivalently stress) affects the optical properties of a device in two concurrent ways. The photoelastic effect modifies the refractive index of materials. This well-known effect has been widely used in industrial photoelastic stress analysis of bulk and thin film samples [85,86]. In addition, stress causes mechanical deformation and changes the geometric dimensions of the photonic components. Following early work on these effects for tuning of silicon-on-insulator resonators [87] and stress sensing [88], we derived an equation describing this coupling and the two contributions just discussed [82]:

$$\frac{\partial(n_{eff}dL)}{\partial\sigma}\cdot\sigma=\left(n_{eff}\frac{\partial\epsilon_L}{\partial\sigma}+\frac{\partial n_{eff}}{\partial\sigma}+\frac{\partial n_{eff}}{\partial\lambda_0}\frac{\partial\lambda_0}{\partial\sigma}\right)\cdot dL \tag{2.13}$$

where dL denotes the length of the waveguide segment under consideration, λ_0 the operation wavelength, n_{eff} the effective index, σ the applied stress, and ϵ_L the normal strain along the waveguide segment. The three terms in the parenthesis on the right-hand-side correspond to waveguide length change, stress-induced effective index modification (which include both photoelastic material index change and waveguide cross-sectional geometry deformation), and dispersive effects, respectively. Integrating over the length of the resonator leads to the shift in operating wavelength due to stress:

$$\frac{\partial(n_{eff}dL)}{\partial\sigma}\cdot\sigma=\left(n_{eff}\frac{\partial\epsilon_L}{\partial\sigma}+\frac{\partial n_{eff}}{\partial\sigma}+\frac{\partial n_{eff}}{\partial\lambda_0}\frac{\partial\lambda_0}{\partial\sigma}\right)\cdot dL \tag{2.14}$$

The wavelength shift is found to scale linearly with both the magnitude of the perturbation σ and the segment length dL, which is consistent with the linear nature of the resonant condition:

$$\int_{L_{tot}} n_{eff}dL=N\lambda_0 \tag{2.15}$$

[1]Our work on this topic contributed to research that was published in: L. Li,..., J. Michon, *et al.*, "Monolithically integrated stretchable photonics", *Light: Science & Applications* **7**, 17138 (2018).

Real-time monitoring of local strain is possible by real-time monitoring of the characteristic wavelength of the optical device subject to the strain, with the accuracy of the optical measurement directly influencing this of the strain measurement. This motivated us to use optical resonators, whose resonant wavelength can be determined with high precision provided their quality factor (Q-factor or Q, a dimensionless quantity defined as the resonant wavelength normalized by the full-width-at-half-maximum of the resonance peak) is high enough. As Q-factors of 10^4 to 10^6 are readily accessible in state-of-the-art photonic devices, the operation wavelength can be measured down to the picometer level [89], corresponding to a strain measurement accuracy around 0.0001% given the expected strain-optical coupling coefficient in the 1 nm/% range (see Figure 2-8).

This sensing method was validated in our group with rings resonators embedded in a multilayer flexible membrane. The membrane was bent to different bending radii and the local strain at the resonator's location was calculated using finite-element modeling (FEM). The detected peak shift was then plotted against the strain as shown on Figure 2-8. This plot both validates our strain-optical coupling theory of Equation 2.14, and provides a straightforward way to determine strain (as well as stress which is trivially connected to local strain by the material's constitutive relations) from a measured wavelength shift.

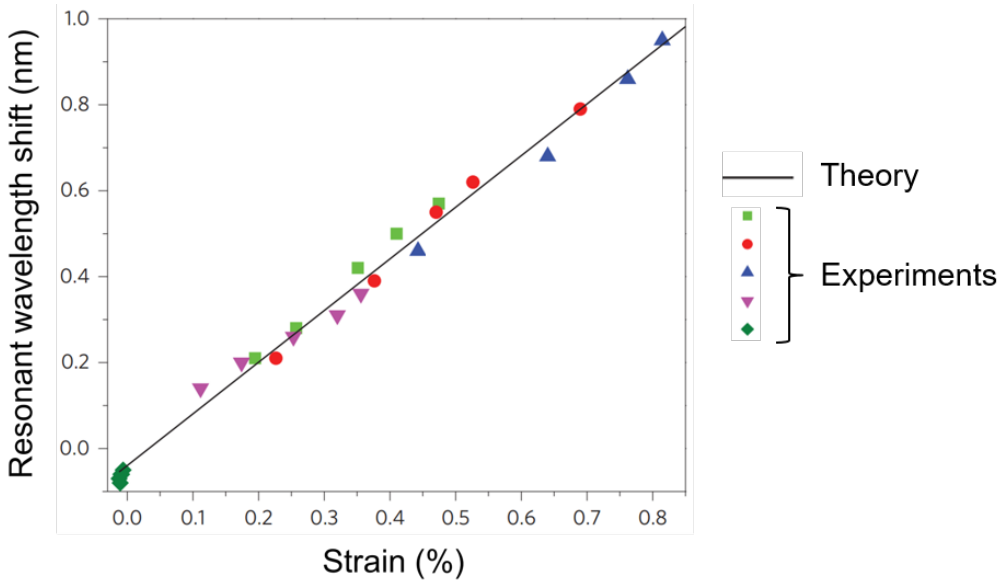

Figure 2-8: Resonant wavelength shift as a function of local strain at optical resonator devices. Symbols are experimental data, which each color corresponding to a different sample. The solid line is the prediction of Equation 2.14. Adapted from [2].

Furthermore, we can take advantage of the tensorial nature of stress and the different polarizations of light to perform direction-sensitive stress measurements. The scalar strain-optical coupling relation of Equation 2.14, which naturally takes into account the different components of stress through the sum on its right-hand side, can be rewritten to account for the effect on both polarizations. The first term corresponding to waveguide length change isn't affected, but the second term now reads:

$$\begin{pmatrix} \Delta n_{TE} \\ \Delta n_{TM} \end{pmatrix} = \begin{pmatrix} (\partial n_{eff}/\partial \sigma_x)_{TE} & (\partial n_{eff}/\partial \sigma_y)_{TE} \\ (\partial n_{eff}/\partial \sigma_x)_{TM} & (\partial n_{eff}/\partial \sigma_y)_{TM} \end{pmatrix} \cdot \begin{pmatrix} \sigma_x \\ \sigma_y \end{pmatrix} \tag{2.16}$$

$$= S \cdot \begin{pmatrix} \sigma_x \\ \sigma_y \end{pmatrix} \tag{2.17}$$

with S the stress-optic coupling sensor. From there, the effective index changes Δn_{TE} and Δn_{TM} can be determined from experimentally measured resonance shifts, and the biaxial stress components calculated by multiplying with the inverse of the stress-optic coupling tensor. This formalism therefore opens up the possibility to perform multi-directional stress quantification.

THIS PAGE INTENTIONALLY LEFT BLANK

Chapter 3

Proof-of-concept device

3.1 Materials choice

Selecting a set of materials is the natural first step in the process of realizing a proof-of-concept device, as it influences the fabrication route to be followed and the properties of the final device. A variety of materials have been explored over the past few years to enable flexible integrated photonics.

Polymers are inherently suited for flexible devices due to their intrinsic flexibility [90]. In addition to serving as the flexible substrate (regardless of the actual optical material), they can themselves be used as the waveguiding or active material: demonstrations of polymer-based devices include waveguides [91], filters [92], various sensing devices including strain sensors [93], accelerometers [93] and ultrasound detectors [94], but also of active devices such as light-emitting diodes [95] and modulators [96]. Besides their mechanical properties making them ideal for epidermal sensors, roll-to-roll processing techniques, and in-vivo applications, the main advantage of polymers lies in their versatility. A wide range of refractive indices is available by tuning the chemical composition, and they are easily processed through a variety of techniques, including molding, even at low temperature. Polymers, however, have one important drawback: they generally have low refractive indices and thus require larger waveguide dimensions, thereby preventing high-density integration.

Inorganic materials such as semiconductors, metals, and glasses, offer an attractive alternative to polymers as they often possess higher refractive indices (>2), allowing for small footprint and tight optical confinement. Additional properties available with some of these materials include increased thermal and chemical stability, and good electronic and/or mag-

netic properties. Crystalline materials however require epitaxial growth, which cannot happen on polymeric substrates. Heterogeneous integration is therefore needed in order to use such materials in flexible devices. The transfer printing method, also called stamp printing or epitaxial lift-off [97], was developed for that purpose [22]. Limitations of this technique include its limited throughput and yield due to restricted area, the use of a sacrificial substrate and the multiple steps involved in the transfer. It is also sensitive to the quality of the bonding surfaces. Amorphous materials such as glasses or amorphous semiconductors on the contrary are amenable to direct deposition on polymeric substrates. Glasses such as chalcogenide glasses [98], silicon dioxide [99] or titanium dioxide [100], amorphous semiconductors such as silicon [88], ceramics such as silicon oxynitride [101], have been used to monolithically fabricate photonic devices on flexible substrates.

Within glasses, chalcogenide glasses (ChGs) are inorganic amorphous semiconductors containing one or several of the group IV chalcogen elements, namely sulphur, selenium, and tellurium. Predominantly used as phase-change materials for memories, they have emerged as a very promising candidate for integrated optics due to their unique properties. The main feature of ChGs is their broad infrared transparency, ranging from 1 to 20 µm. This is due to the heavier atoms, having lower phonon energy, present in ChGs compared to for example silicon dioxide and other oxide glasses [102]. As shown on Figure 3-1, this transparency window covers most of the spectroscopic bands of interest for chemical sensing and thermal imaging. In addition, ChGs possess high refractive indices ($\sim$2.0-3.6) due to their high density and strong polarizability [103]. Other properties relevant to photonic applications include their high non-linear coefficients [104] and their photosensitivity [105]. All of these properties can moreover be optimized for a specific application thanks to the many composition alloying possibilities of the three chalcogen elements and the many different networks formers (such as arsenic, germanium, antimony, gallium, silicon or phosphorus). With regards to processing, their amorphous nature and low deposition temperature enable ChGs to be monolithically integrated onto polymer substrates. Possible techniques include evaporation, sputtering, pulsed laser deposition and spin-coating. They are also well resistant to crystallization. All these features make ChGs uniquely poised for diverse optical applications.

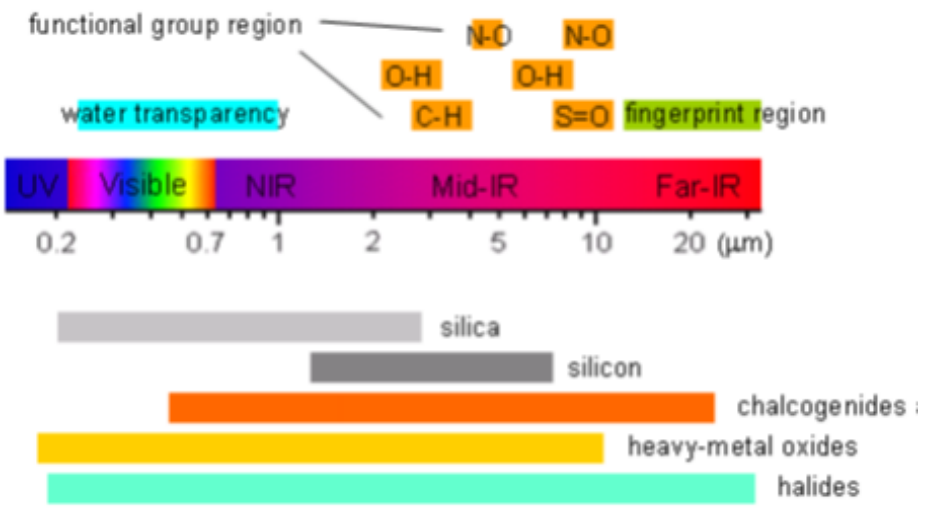

Figure 3-1: (Top) Atmospheric transmission spectrum showing two mid-infrared windows at 3-5 and 8-14 µm. (Middle) Spectral positions of characteristic absorption bands of common chemical groups. (Bottom) Transparency windows (represented by the light gray bars) of several materials, where chalcogenide glass shows excellent transparency across the entire mid-infrared. All three panels share the same horizontal wavelength scale. From [3].

We chose a germanium-antimony-sulfur glass of composition $Ge_{23}Sb_7S_{70}$ (GSS, optical index of 2.22 at 1550 nm, purchased from Irradiance Glass) since it is transparent in the near-infrared, has been shown to be non-toxic [106], resistant to oxidation, and has previously been used to fabricate low-loss devices with a diverse range of applications [107, 108]. Its mean coordination number is $<r> = 2.53$, slightly higher than the percolation threshold at $<r> = 2.4$, leading to a slightly overconstrained network and thus slower structural relaxation. This confers GSS a glass transition temperature (T_g) of 310°C, much higher than commonly used As-based ChGs (the T_g of As_2S_3 and As_2Se_3 are 210°C and 187°C, respectively). GSS aging at room temperature is therefore reduced compared to these other ChGs, which is essential for practical device applications.

SU-8 was used as the polymeric substrate for this initial study. This well-known epoxy verifies all our requirements for the encapsulating material: it has good chemical resistance notably to acids such as hydrofluoric acid (HF), it is optically transparent at 1550 nm with an optical index of 1.57, and importantly given the intended use of our device, it is cytocompatible [106]. Other practical advantages of SU-8 include its ease of processing via photolithography, its availability in a wide range of viscosity allowing for deposition of many different thicknesses (from hundreds of nanometers to hundreds of microns) via spin-coating.

With a stiffness of 4 GPa and a tensile strength of 60 MPa, it is also strong enough to sustain the deformations envisioned.

3.2 Fabrication route

As outlined in Section 2.2, our approach for the fabrication of our 3-D device was to first fabricate a planar device using well-known 2-D fabrication techniques and to then make it 3-dimensional. This section details the steps in that process.

3.2.1 2-D fabrication

For the fabrication of the planar device, we relied on standard, well-established processing techniques traditionally used in the semiconductor industry, in an effort to develop a fabrication route that can be easily scaled up to large-volume production. The general outline of the fabrication route is presented on Figure 3-2. An important feature of this chosen route is that the core material, GSS, is deposited and processed directly on its final polymer cladding. Another option would have been transfer printing of the core material, however this is a non-standard process that we wanted to avoid.

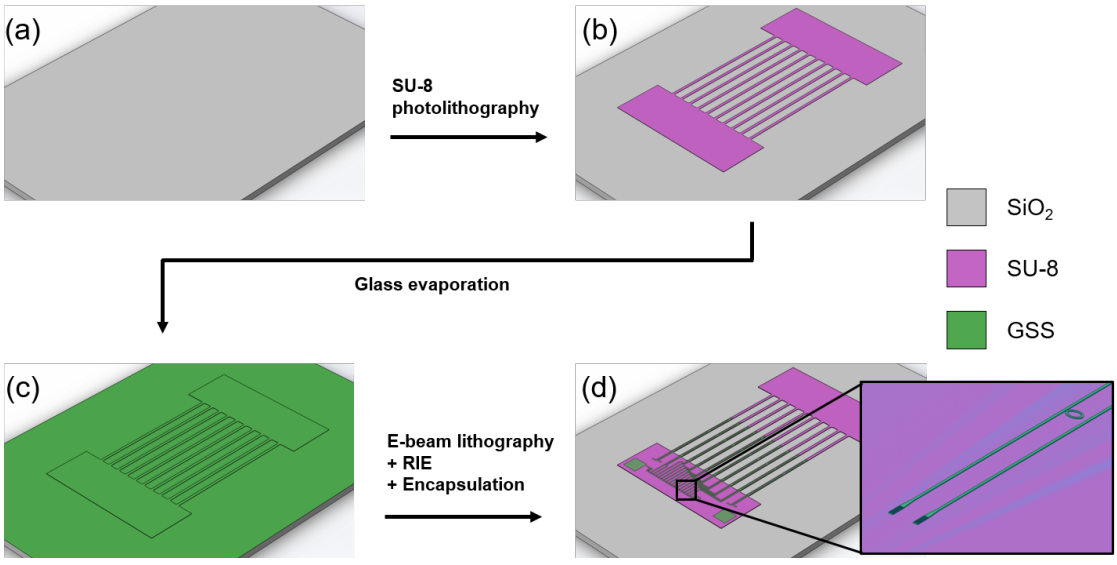

Figure 3-2: Schematic overview of the 2-D fabrication process. (a) Starting 3 µm oxide silicon wafer. (b) Deposition and photolithography of the bottom SU-8 layer. (c) Deposition of GSS. (d) E-beam lithography and RIE of GSS, and deposition and photolithography of the top SU-8 layer.

Fabrication starts with a silicon wafer with 3 µm thermal oxide, which is used as sub-

strate during the planar part of the process (Figure 3-2(a)). While silica-coated wafers are usually used in photonics to provide optical isolation from the high-index silicon, in our case the silica is destined to serve as a sacrificial layer, as will be discussed later in the peel-off step (see Section 3.2.3).

The first step consists in depositing and patterning the bottom layer of SU-8 (Figure 3-2(b)). For a 2µm-thick layer, SU-8 2002 (Microchem) is spun at 3000 rpm for 30 seconds after a 5-second, 500-rpm spreading step. Since SU-8 films are prone to stresses [109, 110], the more so the thicker they get, we use a temperature ramp for all baking steps: the sample is baked on a hotplate at 60°C for 1 minute or half of the datasheet time of the bake (whichever is greater), both before and after the bake. For the soft-bake of SU-8 2002, the samples are therefore baked at 60°C for 1 minute, then at 95°C for 1 minute, then at 60°C for 1 minute. The resist is then exposed with 100 mJ/cm^2 on a photolithography system (MA-4, 10-second exposure at 10 mW/cm^2), and hard-baked: 1 minute at 60°C, 2 minutes at 95°C, 1 minute at 60°C. Finally, it is developed by dipping in propylene glycol monomethyl ether acetate (PGMEA) for 30 seconds and rinsed with deionized (DI) water. As the critical dimensions of this step are large (over 100 µm), the process parameters did not require careful optimization. The mask for photolithography was also created in-house to allow for flexibility in the design. A 5in chrome-covered soda lime mask coated with 5300 Å AZ 1518 resist (Nanofilm) was exposed on a direct-write system (MLA-150, Heidelberger), developed for 90 seconds in CD26, and rinsed with water. The chrome is etched with a chrome etchant solution (CR-7, KMG) for 90 seconds and the resist is stripped with a stabilized piranha solution (Nano-Strip, KMG) for 10 minutes.

The glass is then deposited onto the entire sample (Figure 3-2(c)). While ChGs in general and GSS in particular can be deposited using a variety of techniques, we choose thermal evaporation as it has been shown to provide good quality films over a wide range of thicknesses, good conformality. It is also compatible with most other ChGs, offering options in case the use of another ChG would be desired, for example PbTe for photodetectors, or GSSe for increased index contrast. In the evaporator system used (PVD Inc.), the samples are loaded upside-down over a Tantalum boat that contains the crushed ChG in two side pockets and has a circular hole in the middle to allow for evaporation of the sublimated

glass. Once a pressure below $5x10^{-6}$ Torr is reached in the chamber, the current level in the boat is brought within 2% of the level needed to start evaporation for the previous user. The system is given 5 minutes to stabilize at this power level. Then the power is gradually increased by 0.1% every 10 seconds until the quartz crystal monitor shows the onset of deposition. This power is recorded for use by the next user. Then the power is increased until the deposition rate reaches 10-15 Å/s, at which point the shutter blocking the samples is open. For conformal deposition, the samples are rotated during deposition at 6 rpm. Once the desired thickness (450 nm) on the sample has been reached, the shutter is closed and the power is turned back to 0.

Patterning of the waveguides in GSS is done using lithography followed by dry etching. This choice of techniques (over lift-off, wet etching, ion milling, or nanoimprint) will be justified in the following section. We first use electron-beam (e-beam) lithography to pattern a resist on top of the GSS layer. Advantages of e-beam lithography include its very high resolution that allows for smooth waveguide sidewalls and the writing of small features such as sub-wavelength components, and the flexibility of changing masks. Conventional photolithography presents opposite features. In the first iteration of the fabrication process, SU-8 was used as the resist for it is negative (which decreases writing time and leads to removal of the ChG everywhere on the sample), requires a low dose of around 300 $\mu C/cm^2$ (which also decreases writing time), and doesn't require stripping given that another layer of SU-8 will eventually be added on top. It also has chemical resistance and therefore provide a good mask for reactive ion etching of the ChG. The samples underwent 1 minute of oxygen plasma (100 W, 100 mTorr) to enhance adhesion of the resist, especially on top of the relatively thin buckles where the step profile would cause poor coverage due to edge effects. SU-8 2000.2 was then spin-coated at 2000 rpm for 30 seconds, baked for 1 minute at 95°C, exposed at 300 $\mu C/cm^2$ (300 pA, 0.1 µs/dot, 10 nm^2 dots), and developed for 1 minute in PGMEA. We notably found that following strictly the manufacturer's recommendations of adding a post-exposure bake (PEB) resulted in over cross-linking of the resist in the high-density pattern areas such as the grating couplers. Also, as the resist was aging, the dose required recalibration, and eventually proximity effect correction (PEC) was added to ensure proper writing of the high-density and narrow features. However, for unclear reasons SU-8 stopped giving good results as an e-beam resist and we switched to using

ZEP, causing several changes to the process flow, as will be described in the following section.

A key specificity of our e-beam write, regardless of the resist used, was the need to account for the topography of our sample: the writing fields are located on top of the bottom SU-8 pattern, which lies 2 µm above the surface of the substrate. This point is of importance because of the way the e-beam system focuses on the area to write. In standard operation, the user focuses at a reference point whose height is known to the system. The system then relies on a laser-based height sensor to track the height of the area under the beam, and adjust the vertical position of the stage to ensure that the sample remains in focus. But the laser beam, which is reflected off the sample and collected back by the e-beam system to deduce the height, actually hits the sample a few microns away from the writing area that is directly under the e-beam. Two issues might arise with non-planar samples like ours: the laser beam might reflect off the step between the two heights, causing an error that stops the write, or the laser beam could reflect off a plane at a different height than the writing field, resulting in an out-of-focus e-beam at the writing field height. The first case obviously needs to be prevented. The second case is problematic if the height difference between the two planes is greater than the depth-of-field (DOF) of the system. In our case, the two planes lie 2 µm apart, while the DOF of the e-beam system used (ELS F-125, Elionix) is estimated to be around 1 µm. To circumvent both issues, we took advantage of the possibility offered by the system software to bypass the laser height sensor by defining a height map of the sample. To do so, one needs to focus manually on three points of the sample. The software then interpolates between these points and creates a height map for the sample, which can be given as input for the write. The system then disables its height sensor and uses the height values from the map. Because we have no features on our glass at this point that we could use for focusing, we deposited droplets of gold nanoparticles in suspension at each corner of our device (see Figure 3-3) prior to e-beam. We could then focus on the $\sim$100 nm particles located on top of the glass on top of the SU-8, at the correct writing height. The error on the height of each of these focusing points is the size of the DOF of the system, 1 µm. The error on the height of any interpolation point therefore is within the DOF of the system as well.

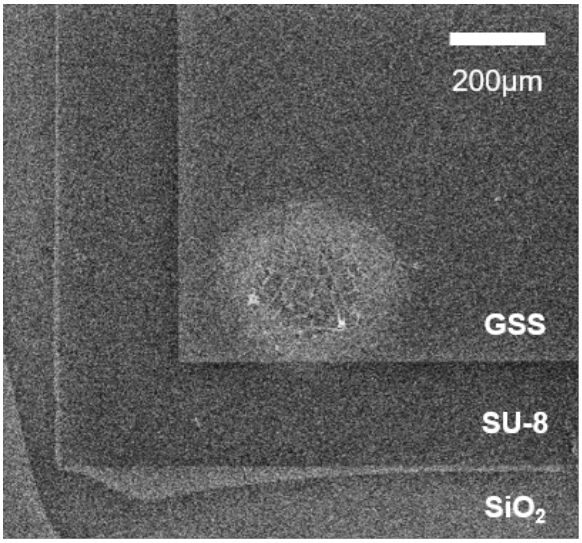

Figure 3-3: SEM image of a corner of the device before e-beam write. The clear halo corresponds to the droplet of gold nanoparticles in suspension used for focusing at the right height.

Reactive ion etching (RIE) of the GSS layer using the e-beam-patterned resist layer as a mask (Figure 3-2(d)) is treated in detail in the next section. Finally, the top layer of SU-8 is deposited to encapsulate the waveguides. SU-8 2005 (Microchem) is spun at 1000 rpm for 30 seconds. The same temperature ramp as previously described is applied for the bake: 60°C for 1 minute, 95°C for 2 minutes, 60°C for 1 minute. Follow a 13 mJ/cm^2 exposure (13 seconds on the MA-4), hard bake at 60°C for 2 minutes, 95°C for 3 minutes, 60°C for 2 minutes, and development in PGMEA for 30 seconds. Just like with the lower layer, no precise process optimization was carried out for this step given the large critical dimensions.

3.2.2 $Ge_{23}Sb_7S_{70}$ reactive ion etching[1]

Dry etching is chosen as the patterning method for the GSS waveguides for it is the only method that fulfills our requirements of smooth, vertical sidewalls, and compatibility with very small features down to a couple hundreds of nanometers, for grating couplers for example. Smooth sidewalls are required because sidewall roughness scattering is expected to be the predominant loss mechanism in ChG waveguides [111], given the much lower material attenuation measured in ChG microsphere (Q-factor of 7.2x10^7 [112]). Ion milling

[1]Our work on this topic contributed to research that was published in: Q. Du,..., J. Michon, *et al.*, "Low-loss photonic device in Ge-Sb-S chalcogenide glass," *Optics Letters* **41**, 3090-3093 (2016).

isn't scalable to large areas and high volume. Nanoimprint requires a ChG that can be processed in solution, such as As_2Se_3 [113] which is however very prone to oxidation, and typically only produced ridge waveguides. Lift-off can produce very high quality sidewalls but realization of small features requires careful optimization and typically several-layer processes.

Both fluorine-based [114] and chlorine-based [115] chemistries have been used to define low-loss GSS waveguides. Early work in our group showed that, while both could be used to achieve high-quality waveguides thanks to passivation during etching, the chlorine-based chemistry relied on silicon contamination of the chamber to form a silica protective coating. Because such a contamination isn't repeatable, we focused on the fluorine chemistry, demonstrating record quality factors of $1.2\text{x}10^6$ [116]. Fluorine chemistry was then used throughout this work. The exact recipe (CHF_3/CF_4 3:1, 45/15 sccm, 5 mTorr, 200 W RF power) developed on a PlasmaTherm system was tweaked as new equipment came into use: CHF_3/Ar 15/35 sccm, 5 mTorr, 300 W ICP power, 60 W HF power was used on a Cobra inductively coupled plasma (ICP) system from Oxford Instruments, giving smooth vertical sidewalls as shown on Figure 3-4(b).

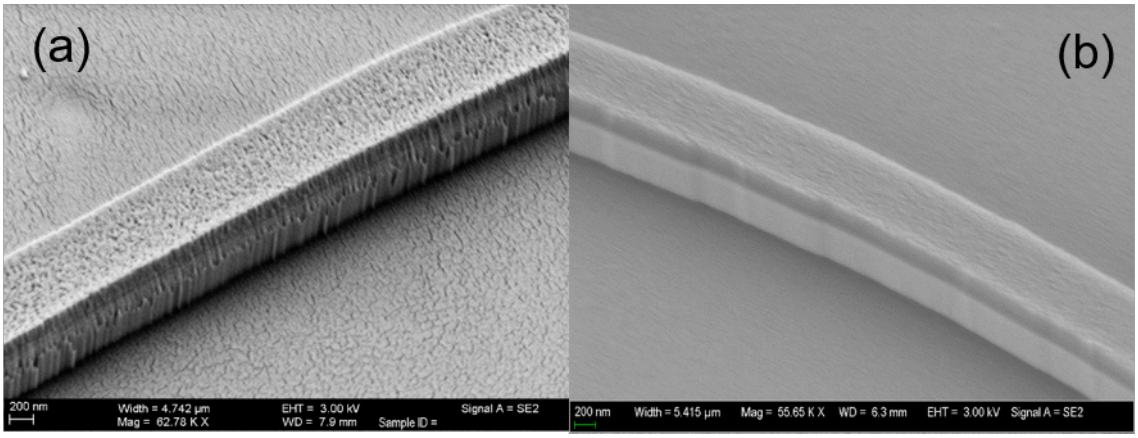

Figure 3-4: SEM images of waveguides after RIE (a) Using SU-8 as e-beam resist. (b) Using ZEP as e-beam resist.

As mentioned in the previous section, we initially used SU-8 as an e-beam resist. However, for unclear reasons SU-8 started giving rise to very rough sidewalls, despite the presence of a protective coating, as can be seen on Figure 3-4(a). This roughness caused both high propagation losses (which is particularly detrimental in our case since our waveguides are ~1cm long) and lower coupling efficiency, making it impossible to measure the devices.

We thus looked for another negative e-beam resist. Another popular choice is MaN 2403 (Futurex Inc.), but its developer is based on tetra methyl ammonium hydroxide (TMAH), a strong base that attacks ChGs. Unable to find a suitable negative resist, we turned to ZEP 520A (ZEON Chemicals) since a processing route using this resist had already been developed in our group. Yet ZEP is a positive resist, meaning a typical write would consist in exposing and etching only the area nearby the waveguide, leaving behind most of the glass layer away from the waveguide. This proved problematic for two reasons: it would prevent access to the substrate's SiO2 layer as needed for peel-off (see following section), and would prevent good adhesion of the upper SU-8 layer. We therefore modified our process to include a GSS removal step, done by either RIE or lift-off as shown on Figure 3-5, before waveguide patterning. The photoresist used for that extra step was AZ P4110 (Microchem). It was spun at 4000 rpm for 40 seconds, baked at 95°C for 1 minute, exposed with 110 mJ/cm^2, and developed with AZ 421K for 30 seconds, resulting in a 1.2 µm layer thick enough both for acting as a mask during RIE or for lifting off 450 nm GSS after a few minutes dipping in acetone. After RIE or for lift-off, the resist is removed by dipping in acetone for 1 minute. ZEP is then spun at 5000 rpm for 1 minute, baked at 180°C for 1 minute, exposed at 2000 µC/cm^2 (10 nA, 0.02 µs/dot, 10 nm^2 dots), developed in ZED N-50 (ZEON Chemicals) for 1 minute, methyl isobutyl ketone (MIBK) for 5 seconds, and stripped overnight in N-methyl-2-pyrrolidone (NMP).

3.2.3 Peel-off

Particular care needs to be taken when releasing the device from its fabrication substrate. The sample indeed loses the protection of the substrate during this step and becomes vulnerable to mechanical failure. In this regard, a distinguishing feature of our device compared to other demonstrations of flexible integrated photonics lies in its patterned structure, instead of being a full film (say spanning the entire substrate area). Larger structures, made of one single piece with large critical dimensions, are more resistant to cracking as stresses are spread over the entire area. Inversely, more complex structures with smaller critical dimensions present many points likely to concentrate stresses and thus reach the onset for cracking, which can then spread over the device. Cracking in the structure material, SU-8 in our case, would render the device non-functional mechanically as it would prevent proper buckling as predicted in Section 2.2. In addition, it would of course spread to the core

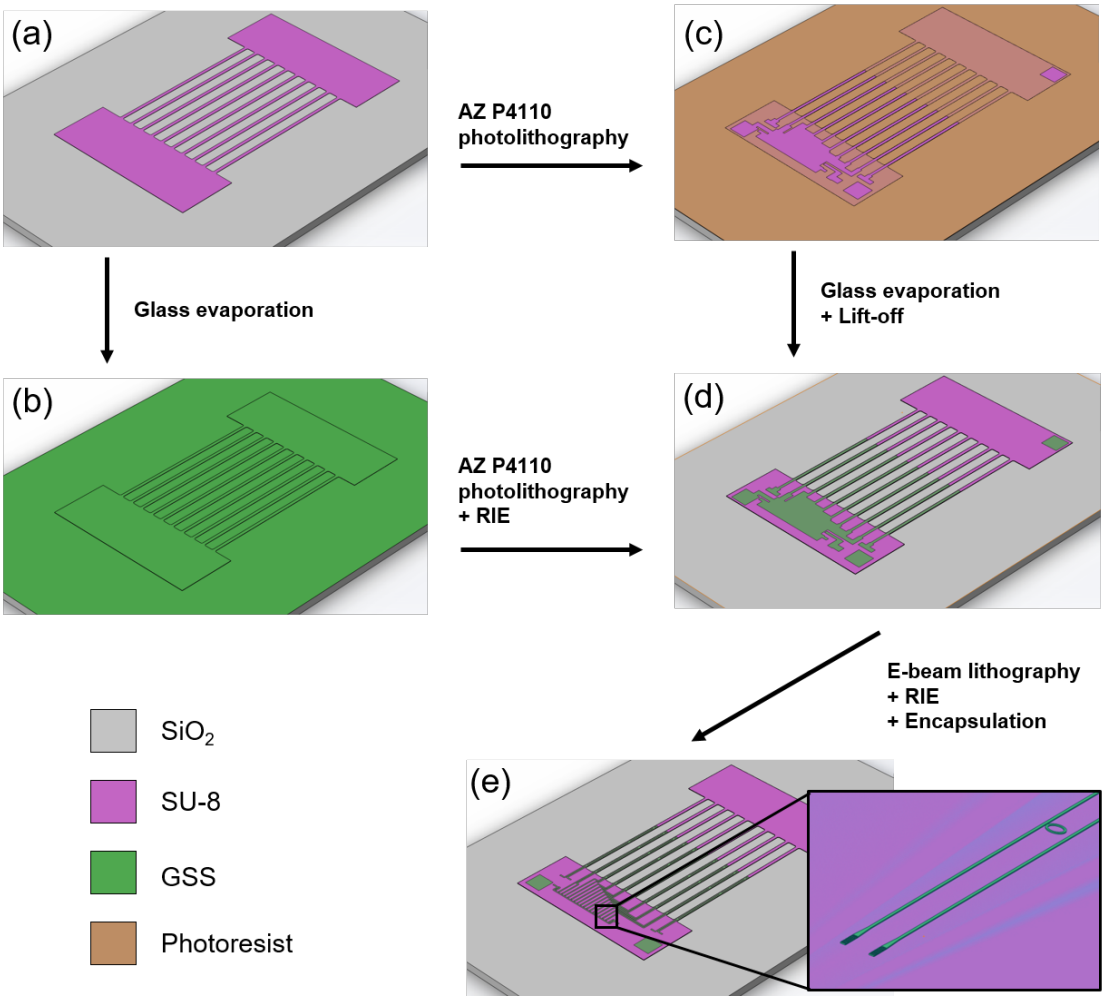

Figure 3-5: Schematic overview of the 2-D fabrication process using ZEP as e-beam resist. (a) Deposition and photolithography of the bottom SU-8 layer. (b) Lift-off route: deposition and patterning of AZ P4110. (c) RIE route: deposition of GSS. (d) Large-scale patterning of GSS by lift-off or RIE. (e) E-beam lithography and RIE of GSS, and deposition and photolithography of the top SU-8 layer.

material, which is embedded in the structural material, making the device non-functional optically as well.

This causes a more involved release step for our devices, as additional care has to be taken to preserve the integrity of the device. The common release technique of directly picking up the flexible structure with a stamp or tape, which works well for full films and/or thick films [109,110], proved to generate too much stress for our structure and caused cracks to appear at the junction between the "islands" and the buckles. We believe the issue to take place at the peel-off front, where the structure detaches away from the substrate, as this is where forces are concentrated and the device undergoes bending. Another common

method consist in releasing the flexible device by removal of a sacrificial layer underneath the structure, and picking up the sample that is then a freestanding membrane. This however is limited to thick samples with large features, as thin membranes wrinkle when freestanding in solution. Other more complex possibilities exist for creation of a flexible or stretchable sample from a rigid 2-D substrate, for example patterning the back of the substrate wafer to open up windows for wet etching of the substrate from the back, leaving only the protected areas rigid on the substrate, yet we stayed away from these precisely because of the added number of steps and complexity.

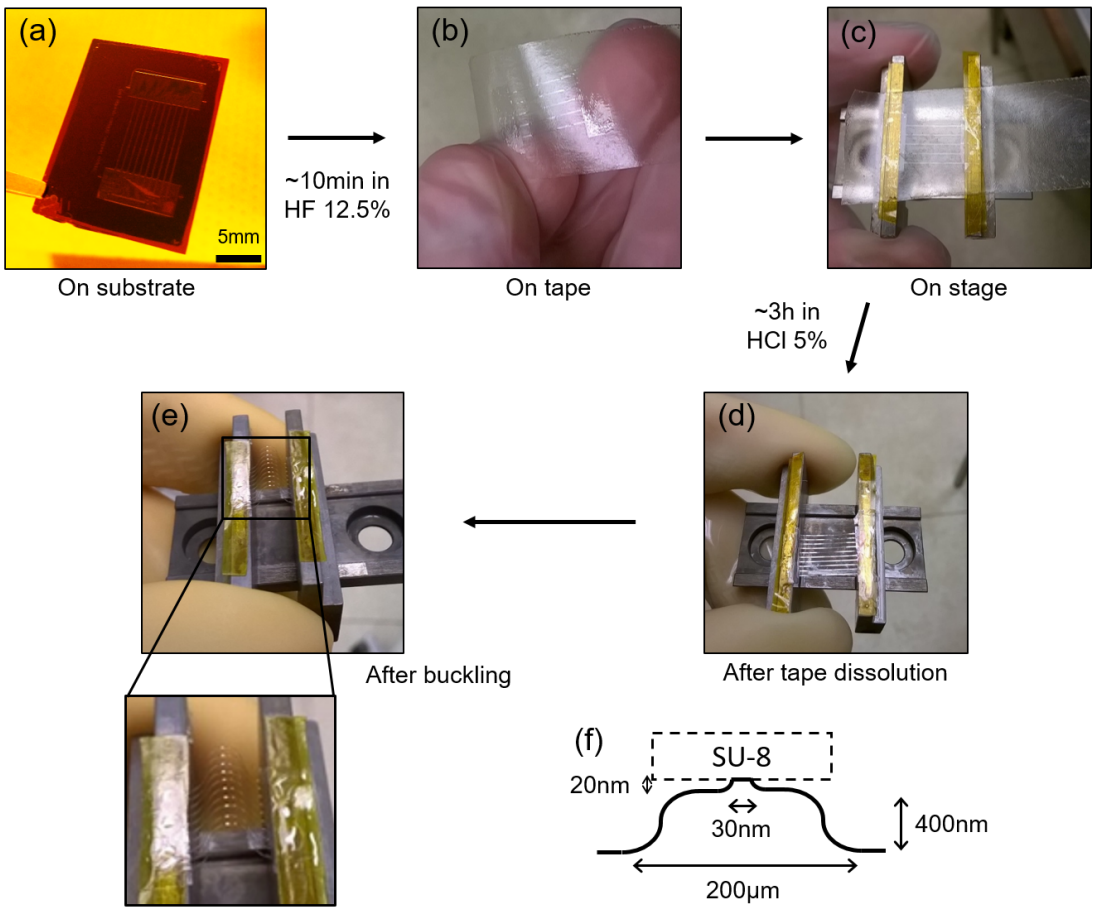

Figure 3-6: Pictures of our devices at different steps of the peel-off process. (a) On its substrate after 2-D fabrication. (b) On water-soluble tape (Kapton tape is usually used too) after delamination from the substrate. (c) Placed on stage. (d) On stage after dissolution of the water-soluble tape. (e) On stage after buckling by bringing the two ends closer together. (f) Schematic of the profilometer profile of the SiO_2 substrate under a buckle after delamination of the device.

We use a combination of the two most common techniques to enable the release of our

device from its substrate. Because it is too thin to be picked up from solution after sacrificial layer removal, we use tape to delaminate it; because its shape and thinness would cause damage if too much force is applied by the tape, we undercut a sacrificial layer underneath it to help with its delamination. Our optimized process is shown on Figure 3-6. The final 2-D sample on its substrate (3 µm SiO_2 on Si, Figure 3-6(a)) is dipped in diluted hydrofluoric acid (HF) for about 5 minutes, until the sample can be visually seen to start lifting off. We use 12.5% HF (1:3 in water), although higher or lower concentrations would theoretically be possible as well if a shorter or longer peel-off time were desired, respectively. However the etch rate for wet thermal oxide in diluted HF is reported to range from 20 nm/min to 2 µ/min for 5% to 49% HF respectively [117], which hints at an etch rate of several hundreds of nm/min in our case. Yet the height profile (see Figure 3-6(f)) of the SiO_2 surface after delamination of the device points at a release mechanism independent of the vertical etch rate of oxide: etching appears to happen preferentially horizontally along the SiO_2/SU-8 interface, extending over 100 µm laterally while only 20 nm vertically in the region under the SU-8. Outside of the SU-8 region, etching happens vertically as usual, at a much slower speed (tens to hundreds of nm/min). Once the structure is seen to detach from the substrate (water can be seen flowing under the buckles, which are of course released first, then the edges of the "islands" are seen moving as well), the sample is taken out from the HF solution, carefully rinsed in DI water without washing the device away, and gently blow-dried with nitrogen. Tape is then applied onto the sample. Kapton tape is a common choice for this step, as polyimide has a high Young's modulus of 2.5 GPa preventing excessive bending and therefore stresses during peel-off. Yet our device requires the tape to be removed in order to allow for different buckle shapes and behaviors once integrated in a system to be measured (otherwise they would all be constrained by the tape). We thus use water-soluble tape (3M) to peel off our device. We found that using water-soluble tape alone led to cracks in the device after peel-off, probably because of the low rigidity of the polyvinyl alcohol backing of the tape. We optimized the peel-off step and found that we needed to add a layer of Kapton tape to provide structural rigidity during peel-off. Once on tape (Figure 3-6(b)), the integrity of the sample can be verified with an optical microscope, and it is placed onto the stage (Figure 3-6(c)) in its flat configuration, with the islands resting on the flat ends of the stage. Both ends are prepared with double-sided Kapton tape. The entire stage is then dipped in 5% hydrochloric acid (HCl) for a few hours to dilute the tape away. Diluted HCl

is used instead of pure water to accelerate the process as we found that a longer dipping time could lead to failure of the adhesion at the Kapton tape/SU-8 interface before the tape was fully dissolved. Once removed from solution and rinsed in IPA, the flat device on stage (Figure 3-6(d)) can be buckled by bringing the two ends closer together (Figure 3-6(e)).

3.3 Packaging and measuring[2]

Once fabrication is over, comes the time to measure the device. The optical transmission measurement setup used to characterize the device is schematically illustrated on Figure 3-7. We used an optical vector analyzer with built-in tunable cavity laser (OVA-5000, Luna Technologies) in conjunction with an erbium-doped fiber amplifier (EDFA, Amonics) as the light source and detector, that allow us to sweep the wavelength and record the output power through the device from 1525 nm to 1620 nm. The most critical point (where the largest optical losses occur) of this setup is the coupling of light from/to the fiber to/from the device waveguides, as it directly influences the amount of power collected at the detector and therefore the ability to "read" the optical signal. Coupling is also the limiting step timewise when it comes to measuring the devices. A scalable coupling scheme is therefore required if one desires to measure many sensors at several time points, as is the case in our envisioned biological studies. Finally, our project presents the added constraint of requiring the devices to be shipped to our collaborators at University of Delaware where they will be used: this requires a packaging that both is robust enough to survive the 500-mile journey and ideally enables easy usage in a biological laboratory by optics non-specialists. We tried three different ways of doing fiber-to-device coupling to find one that satisfies all our requirements.

Our first approach, based on the available capabilities in our laboratory at that time, was to fire-end coupling (also called "butt-coupling" or "edge coupling"), shown on Figure 3-8(a). In this method, end facets are created for the waveguide by cleaving the sample along a crystallographic direction of the substrate, thereby resulting in (theoretically) straight and smooth facets. A fiber is then brought in close proximity (less than 1 µm) to the facet and light is coupled to/from the fiber from/to the waveguide. To mitigate the large mode field

[2]Our work on this topic contributed to research that was published in: D. Kita,..., J. Michon, *et al.*, "High-performance and scalable on-chip digital Fourier transform spectroscopy", *Nature Communications* **9**, 4405 (2018).

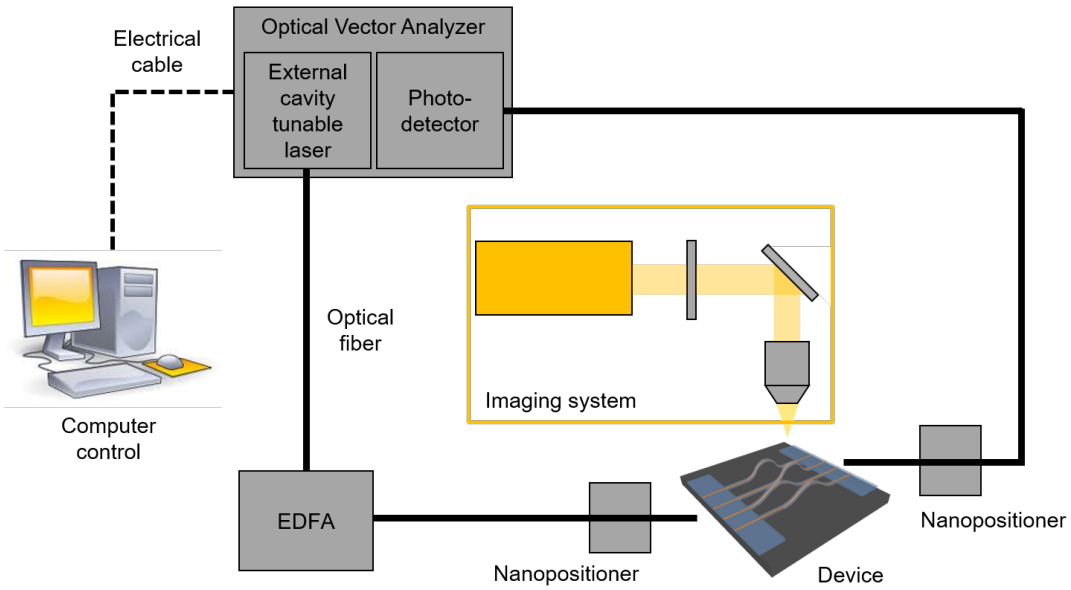

Figure 3-7: Schematic diagram of the measurement setup.

diameter (MFD) difference between the standard single-mode fiber for C band (around 10 µm) and our waveguides (around 1 µm) that would result in a large mode mismatch and poor coupling, we used tapered-lens fibers (Nanonics Imaging), that is, fibers whose end was tapered down from its usual 125 µm diameter to form a lens, resulting in a MFD at the focal point of 1.7 µm, much closer to this of the waveguide. The waveguides were also tapered from their usual width of 0.8 µm to 2 µm near the facets, again in order to bring the MFD closer to this of the fibers. While mode converters have been developed to reduce losses and increase tolerances in end-fire coupling schemes by expanding the waveguide mode through e.g. inverse tapers [118, 119], metamaterial-like features [120], or dual- or several-waveguide geometries [121], we did not spend time optimizing this coupling configuration because of the several drawbacks of this approach. First, even with the aforementioned mode expansion techniques, the alignment tolerance for fire-end coupling remains very tight: the 3dB tolerance of our configuration was simulated to be about 1 µm, as shown on Figure 3-8(b). This requires very precise positioning of the fiber tip to get maximum coupling and therefore longer and more difficult alignment. This also means a greater sensitivity to vibrations, which more easily bring the device and fiber out of coupling. This last point is particularly problematic as the edges of the device are freestanding, and a 10 µm-thick membrane is obviously very prone to vibrating. Another issue lies in cleaving the samples to create the facets. This method works very well for devices fabricated right on top of the

substrate like usual integrated photonic components, since the fracture in the crystalline silicon transfers well to the other materials right above it, resulting in a clean, smooth waveguide facet. However, it can be problematic for components cladded in thick polymer layers that wouldn't necessarily transfer the stresses to the waveguiding material. This could cause not-vertical and rough facets, which would incur additional losses. This wasn't an issue in our proof-of-concept device as the bottom SU-8 layer was only 2 µm thick, but wouldn't be broadly applicable to any monolithically fabricated optical component. Lastly, the way fire-end coupling was done in our lab wasn't scalable. A single fiber was aligned at a time, thus requiring $2 * \#waveguides$ alignment steps. The fibers also weren't attached to the device. This removed the worry about fiber integrity and coupling conversation during shipping, but meant that our collaborators would have to have their own alignment setup (which is expensive) and redo alignment (which takes time). The alignment setup would also have constrained the form factor and volume of any environmental control system needed to ensure proper conditions for the biological studies performed. There exist ways of bonding butt-coupled fibers to optical chips, for example using fiber arrays, however this option wasn't available to us because of the freestanding edges of our device. Overall, fire-end coupling proved not to be robust, scalable, and easy-to-use enough for our purposes.

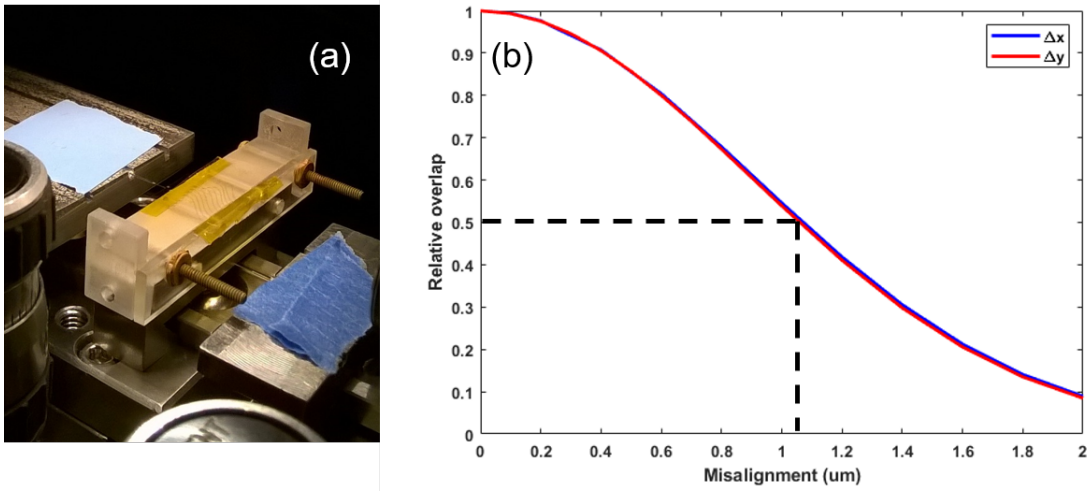

Figure 3-8: (a) Picture of a buckled device measured with fire-end coupling, with horizontal tapered-lens fibers positioned near the cleaved facets of the device. (b) Alignment tolerance along the horizontal (x), and vertical (y) directions simulated by calculating the overlap between the waveguide mode and a 1.7 µm -waist Gaussian beam.

The other popular way of coupling light from a fiber to an integrated waveguide is

with a grating coupler. This method relies on a grating placed at the termination of the waveguide to diffract light into or out from the waveguide. Compared to fire-end coupling, grating coupling presents the advantages of relaxed alignment tolerances thanks to the possibility of defining a larger MFD by using a larger grating region [122, 123], the possibility for higher integration density by using 2-D arrays of fiber terminations instead of 1-D for butt-coupling [124]. Usual drawbacks of grating couplers include lower coupling efficiency and reduced bandwidth. We were however less interested in transmitted power than in resistance to vibrations. We therefore switched to a grating coupling setup with flat-cleaved fibers angled at 75°(Figure 3-9(a)). This approach indeed proved much more convenient for measurements, with faster alignment and greater resistance to vibrations: we measured a 3dB alignment tolerance of around 6 µm, as shown on Figure 3-9(b). The measured insertion losses of ∼10 dB (estimated from the 20 mW EDFA power, the 2 µW output power, and the 20 dB waveguide loss) and bandwidth of >50 nm (see Figure 3-9(c)) were enough for our purposes. Yet the fibers coming from the top of the sensing device reduced even more the space available for any control system needed for the biological studies. Furthermore, our collaborators did not have a setup ready for this type of coupling. We therefore decided not to send the device alone, but to first bond the fibers to the device so as to make it a "plug-and-play" device for them: once received, the fibers would just need to be plugged into the laser and detector, without any alignment step required. Besides saving time, this also allowed our collaborators to place the device in the environment of their choice instead of being constrained by the alignment setup. Notably, they were now able to place the sensing device and the biological sample grown around it in an incubator to control precisely the growth conditions, while remotely monitoring the sensors (the laser and detector can be located far away from the incubator, with optical fibers making the link). The procedure for fiber bonding is quite straightforward: after getting the device and the fiber aligned, the device was lowered, a drop of UV-curable epoxy was placed over the grating coupler, the device was brought back up and put in alignment again. Our choice of epoxy was based on two criteria: we wanted a low viscosity (to not perturb the fiber too much with flows), low thermal expansion (to not move the fiber during curing), and minute-range curing time (to have time to make corrections to the fiber position). We selected the epoxy UV15TK (Masterbond) that has a 2 $\%.K^{-1}$ thermal expansion coefficient (CTE), cures in about 1 minute under exposition to 365 nm light, and has a viscosity of 6,000 cP. Other epoxies had

lower CTE (down to 0.01 %.K^{-1}) and/or lower viscosity (down to 480 cP) but were either curing too fast (in 1 second) or too viscous (25,000 cP). We found that curing the epoxy right away with a high-power UV lamp resulted in irreversible misalignment, as the epoxy undergoes shrinkage and thermal expansion/contraction during curing, whose overall effect we couldn't control: for a 2 %.K^{-1} CTE, the change of size of a 0.5 mm drop is 10 µm, which is much greater than the alignment tolerance of the grating coupler and can misalign the fiber. After alignment, we would therefore wait for 30 to 60 minutes while monitoring the transmitted power and adequately realigning the fiber, allowing the epoxy to flow as the fiber was moved, and slowing starting to cure. Once the power had stabilized, the device was left to cure overnight with a low-power UV lamp, and fully cured the following day with a high-power UV lamp (Loctite CL32 Curing Wand). While we did manage to successfully bond several devices this way [125], several issues arose with this process. First, only one fiber was aligned and bonded at a time, therefore again requiring $2*\#waveguides$ alignment and bonding steps for a single device. Moreover, because a substantial amount of epoxy is needed to ensure strong adhesion, a $\sim$1 mm diameter epoxy blob was used on top of each grating coupler, thereby limiting the density of grating couplers on the device. This method thus isn't scalable. In addition, since the epoxy isn't optimized for adhesion to polymers, the adhesion remained quite weak even after plasma treatment of the device prior to bonding (it happened several time that the entire solidified drop of epoxy, with the fiber embedded in it, detached from the device). The sturdiness is also compromised by the fact that fibers have to be stripped in order to be flat-cleaved (see the bare fibers in Figure 17(b)). Despite using stress-relieving supports, the likeliness of this packaged device to support transport and handling is quite low. This method thus doesn't yield a robust product.

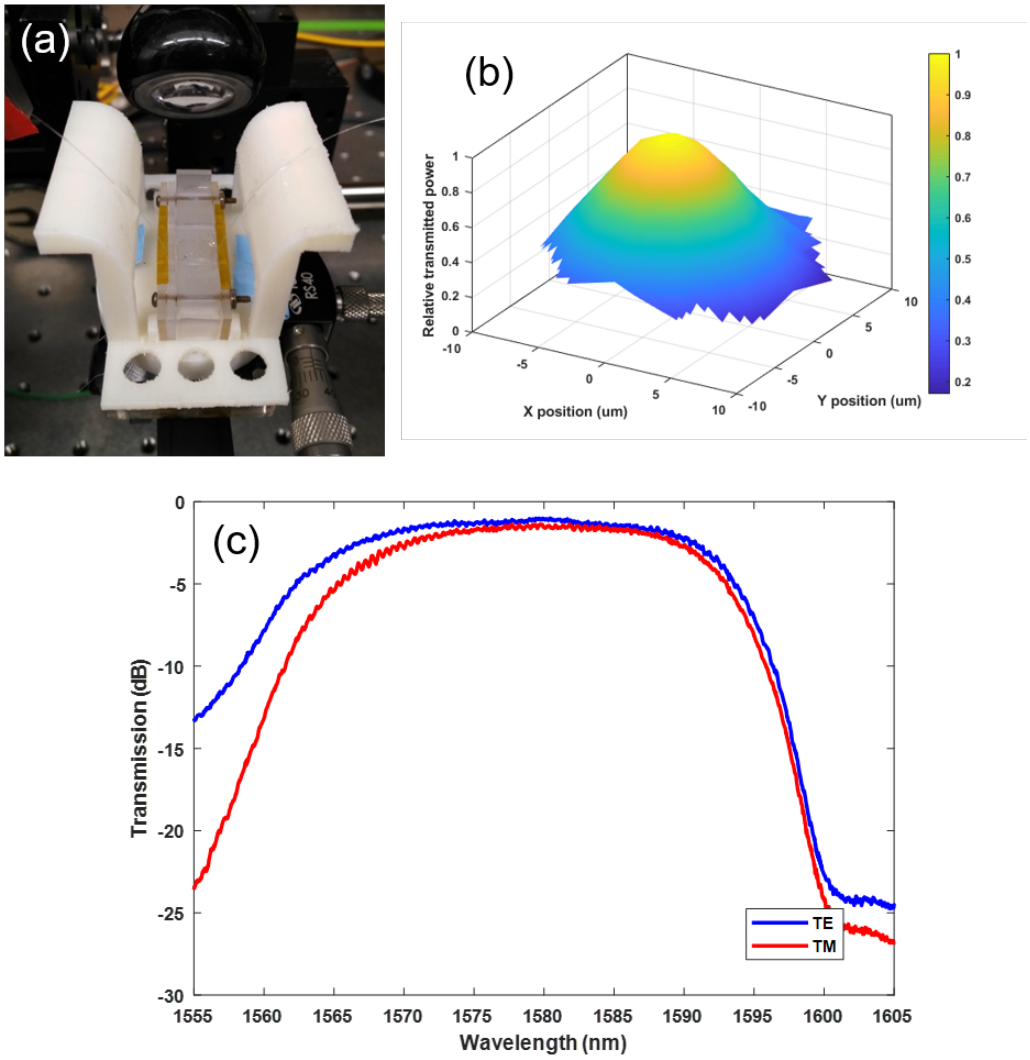

Figure 3-9: (a) Picture of a buckled device measured with single-fiber grating coupling, with flat-cleaved fibers coming at 75° on top of grating couplers on the surface of the device. On this picture, the fibers were bonded to the device and to stress-relieving structures. (b) Measured relative transmitted power as the fiber is moved around the grating coupler's location. (c) Transmission spectrum of a device consisting in two grating couplers linked by a waveguide.

Scalability and robustness are problems often encountered in industrial setting and solutions have therefore been developed to deal with these issues. One way to overcome both at once is to use fiber arrays (FAs): several fibers are secured next to one another between two blocks typically made of glass. The fibers are placed in V-grooves etched into the lower block, allowing for precise control of the pitch between fibers – 125 µm and 250 µm are standard

pitch values, providing high integration density. More importantly, because the position of the fibers is known within 1 µm, designing the waveguides to match these positions means that all waveguides can be aligned at once to their respective fibers, finally making for a scalable coupling scheme. Robustness is greatly improved thanks to the increased surface area of the block end face, which is several millimeters wide and tall. The fibers emerge from the fiber array in their cladding, so are less likely to break at another point as well. Bonding is also made easier by the fact that the fiber array is less sensitive to the movement of the epoxy during alignment and curing, thereby allowing for faster bonding and better coupling efficiency. We ended up using a 8-channel fiber array at first, then a 18-channel fiber array (SQS Vlaknova Optika) with 250 µm pitch. The outmost two fibers were used to align the fiber array using a shunt waveguide (see the device waveguide layout on Figure 3-14(a)), with the remaining 16 being automatically aligned to the middle 8 waveguides. We were able to bond such a fiber array to a device (Figure 3-10(a)), send it over to University of Delaware, and have it used there (Figure 3-10(b)). This approach therefore satisfies all our requirements.

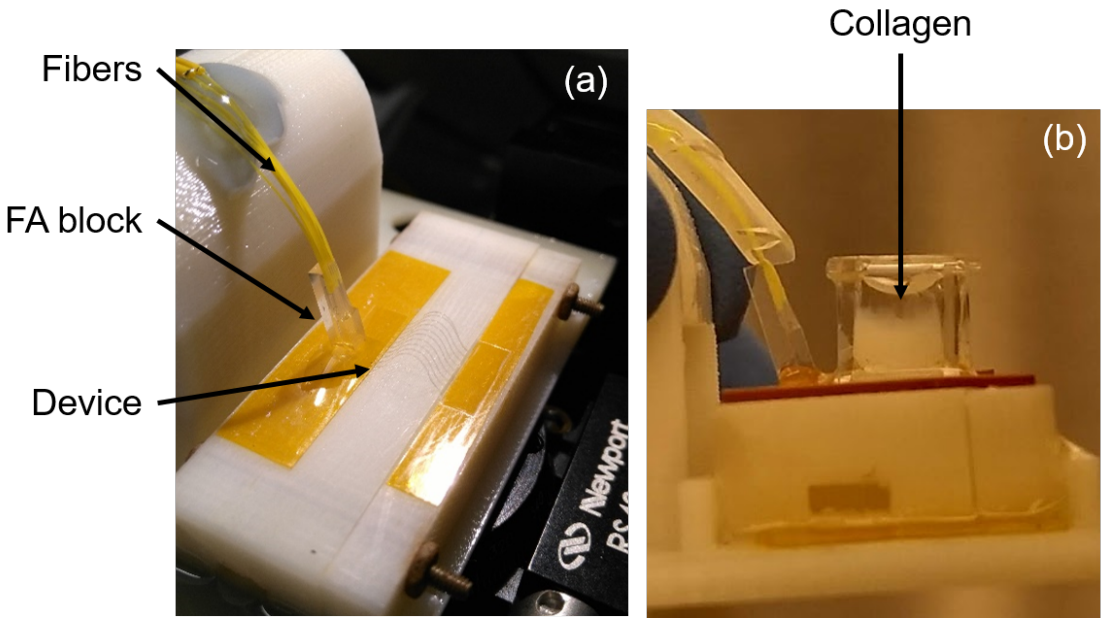

Figure 3-10: (a) Picture of a buckled device measured with fiber-array grating coupling, with a 8-channel 15°-flat-faced array. On this picture, the fiber array is bonded to the device and to a stress-relieving structure. (b) Picture of a device integrated in collagen using the process described in Figure 2-3. Courtesy S. Geiger.

After optical coupling, the device can be measured. A sample output spectrum is presented on Figure 18. Despite the overall optical pathlength being quite lossy with a baseline between -20 and -40 dB, we can clearly distinguish resonant peaks and the device can be used for sensing. An important characteristic of resonant peaks is their quality factor (Q-factor), that directly influences the precision of the resonant wavelength reading [89]. Our devices typically exhibit loaded Q-factors around 40,000, corresponding to intrinsic Q-factors of 20,000 given that we operate at critical coupling.

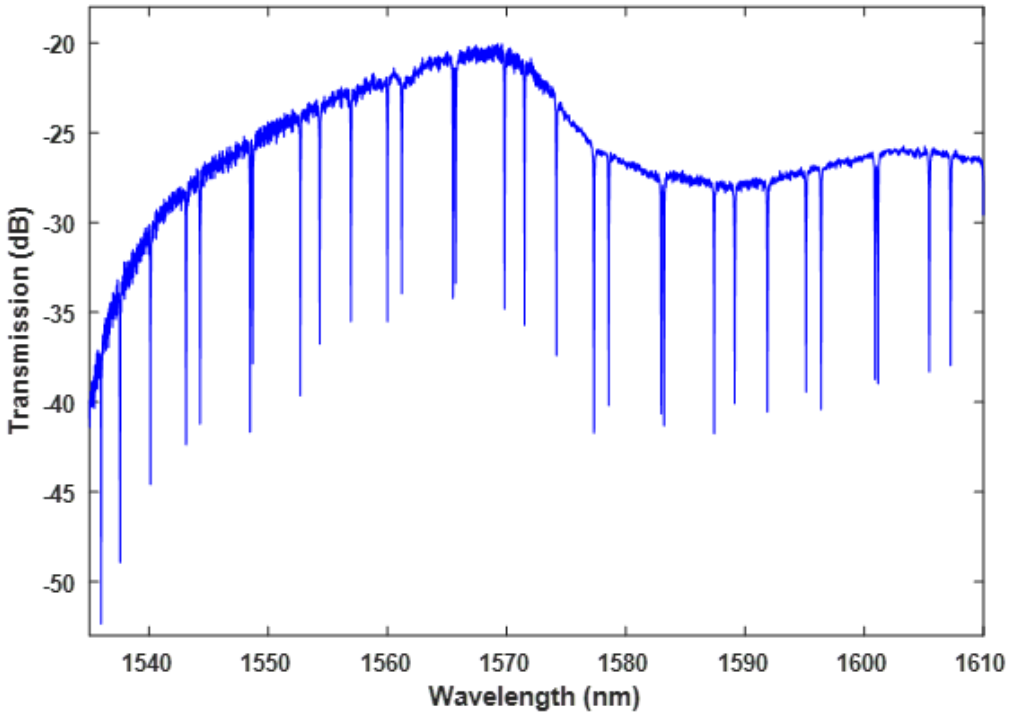

Figure 3-11: Transmission spectrum of a waveguide coupled to two rings resonators of different diameter, showing resonant peaks with loaded Q-factor $\sim$4x10^4.

This value is much lower than our previously demonstrated record intrinsic Q-factor of 1,000,000 for GSS waveguides at 1550 nm [116], using the same waveguide geometry, resist and etching. Several factors can explain this difference. The substrate probably plays a role: these waveguides are fabricated on spin-coated SU-8 whereas GSS was evaporated directly on the wafer's SiO_2 in the record devices. This has two potential effects. First the SU-8 may not be perfectly planar and may have accumulated imperfections during processing, while the SiO_2 surface can be thoroughly cleaned using HF and piranha before processing. Second this forced us to use a 3-point height correction during e-beam writing (see Section 3.2.1)

instead of constantly monitoring the focus with the laser height sensor. Slightly out-of-focus patterning of our waveguides could lead to rougher sidewalls, where scattering due to roughness takes place. Also related to roughness scatering is the fact that the record devices were clad in air against SU-8 for our devices, providing a higher index contrast (Δn = 1.16 vs. (Δn = 0.59) and therefore a stronger confinement of the optical mode in the waveguide core. This results in a lower overlap of the optical mode with the sidewalls of the waveguide. Sidewall roughness scattering is expected to be the predominant loss mechanism in ChG waveguides [111], given the much lower material attenuation measured in ChG microsphere (Q-factor of 7.2x10^7 [112]). The potentially rougher sidewalls and the lower overlap with the sidewalls are thus the likely reasons for lower losses of air-clad, on-substrate written devices.

We can estimate the wavelength resolution of our setup based on this Q-factor value. With a Q-factor of $\sim 10^4$, a wavelength noise amplitude of 0.1 pm, and a light source spectral width of 2.6 pm, the wavelength resolution of the setup is below 1 pm [89]. As we will see in the following section, this is an order of magnitude lower than temperature-induced fluctuations of the resonant peak position. This thus validates both the fabrication process, that yields good enough resonators, and the measurement setup.

3.4 Accounting for temperature and aging

We showed in the previous section that we are able to measure the resonant peak position with precision. Before using this for sensing, we needed to ensure that the only factors influencing the peak position would be these we want to measure – in our case, mechanical deformation. We also wanted to get an idea of the repeatability of the measurement, which will eventually influence the sensitivity of the sensor. We therefore took several measurements of the same device at different time points. A collection of sample transmission spectra is shown on Figure 3-12. We can see that the peak position shifts significantly, over several hundreds of picometers, over the course of as little as an hour. Given an expected sensitivity on the order of 1 nm/% strain [2], such a shift would correspond to strains in the range of 0.1% to 1%. These are however levels of strain we hoped to detect with our device. We therefore need for compensate for that unwanted noise that could hide our signal of interest.

The position of a resonant peak is given by the resonance condition:

$$\lambda_r = \frac{n_{eff}L}{N},\ N \in \mathbb{Z}^* \tag{3.1}$$

A change in resonant wavelength must be due to a change in the effective index of the waveguide, or a change of the cavity length. Looking at the behavior of the peaks over time, we identified two possible causes for the peak shift. The large day-to-day variability can be explained by temperature variations in the laboratory. Short-term variability could also be explained by temperature changes, in particular after the lamp needed for alignment is turned on and shone in direction of the device. However, we would expect the environment to reach steady-state quickly and no more variations would be seen after a few minutes of transient behavior. Yet the peak keeps on shifting even after 40 minutes. We attribute this effect to the photosensitivity of the device – the change in optical properties as a result of exposure to light.

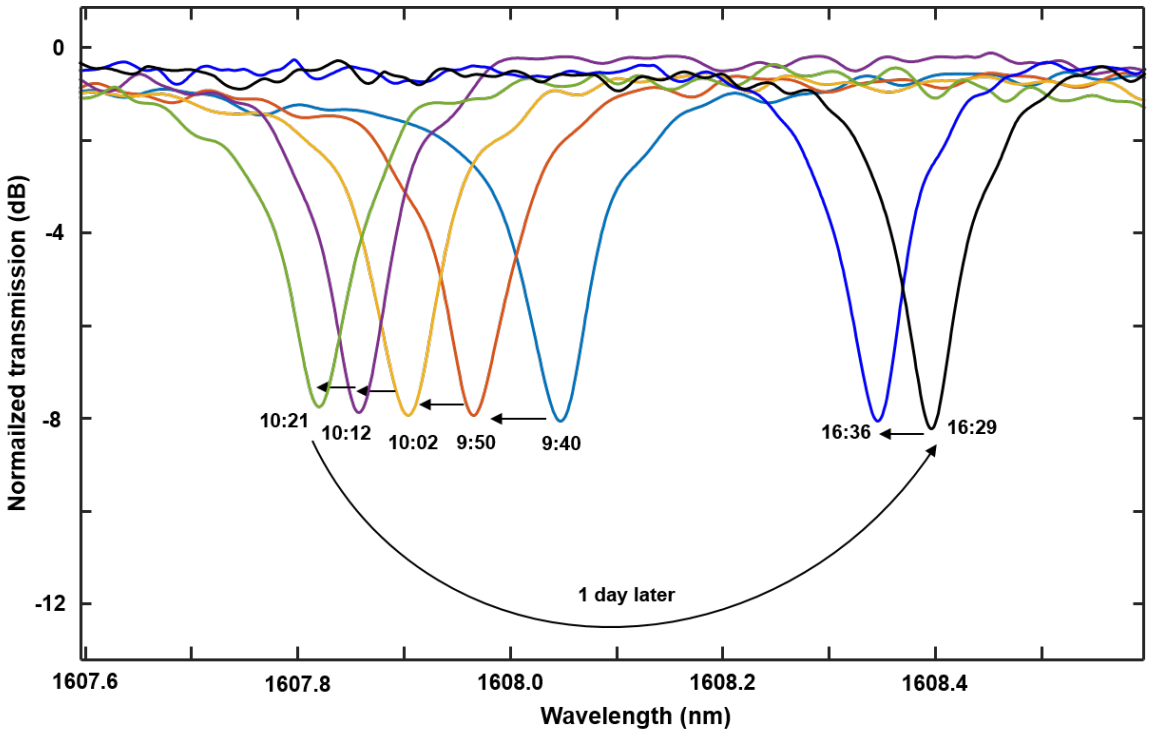

Figure 3-12: Superposed transmission spectra of the same device at different times. The change in baseline level is due to coupling variations over time, which do not affect the resonant peak position.

3.4.1 GSS aging[3]

ChGs in general and GSS in particular have long been known to exhibit photosentivity [126–128]. While this effect can be very useful for some applications, it is undesirable when materials stability is necessary, as in our case. We therefore looked for ways to suppress it.

Because glasses are inherently thermodynamically metastable, they are subject to aging effects as their structure relaxes towards a more stable state. This structural change induces changes in the glass' mechanical, optical, and thermal properties. Its control is therefore of paramount importance to practical applications involving glass materials. It is known that the processing history of ChGs strongly influences their aging behavior. Exposure to light at a wavelength near the band-edge of the glass causes photobleaching or photodarkening [129], and similar effects have been achieved with exposure to heat, radiation, or electron/ion beams. Given the nature of our device, the most practical way to accelerate aging of our devices was to expose them to light. We wanted to reach photosaturation – the point where no further change could be detected. In our initial experiment, we exposed a buckled device to a halogen lamp over 20 days and measured it at intervals of several days (Figure 3-13(a)). We found a change in the free-spectral range (FSR) of the device of ∼10% over the course of the measurements. Since the FSR is related to the group index and therefore the waveguide's optical properties through:

$$\mathrm{FSR} = \frac{\lambda_r^2}{n_g L} \tag{3.2}$$

this indeed meant that a large change was happening in the device's materials. After 15 days, no further change in the device response could be seen.

To better quantify the aging behavior of our device, a separate study [4] was undertaken to look at the response of our stack of materials (GSS waveguide clad in SU-8) to a variety of processing routes. Three groups of identical devices were fabricated. All were covered with opaque tape during aging measurements, to isolate the aging effects from GSS photobleaching. One group was left as is after fabrication. It exhibited a large refractive index change on the order of 10^{-2} with a time constant of 32.5 days, confirming the unstable nature of as-processed GSS and its slow relaxation kinetics. The second group was exposed to a calibrated broadband halogen lamp and exhibited a refractive index change on the order

[3]Our work on this topic initiated a research project that was published in: S. Geiger,..., J. Michon, *et al.*, "Understanding aging in chalcogenide glass thin films using precision resonant cavity refractometry", *Optical Materials Express* **9**, 2252 (2019).

of 10^{-2} during exposure (Figure 3-13(b)), then relaxed over 10^{-3} with a time constant of 12.4 days. This already represents a time to equilibrium cut almost by a factor of 3, while also decreasing the magnitude of the change. This result is also consistent with the initial measurement of ∼2 weeks to reach photosaturation using a less powerful lamp. Finally, the third group was annealed for 2 hours at 130°C and then displayed a much smaller change in refractive index (on the order of 10^{-4}) with a much shorter time constant of 1.4 days (Figure 3-13(c)). We concluded that the best treatment to avoid parasitic aging effects during our measurements was to both photosaturate the devices and anneal them.

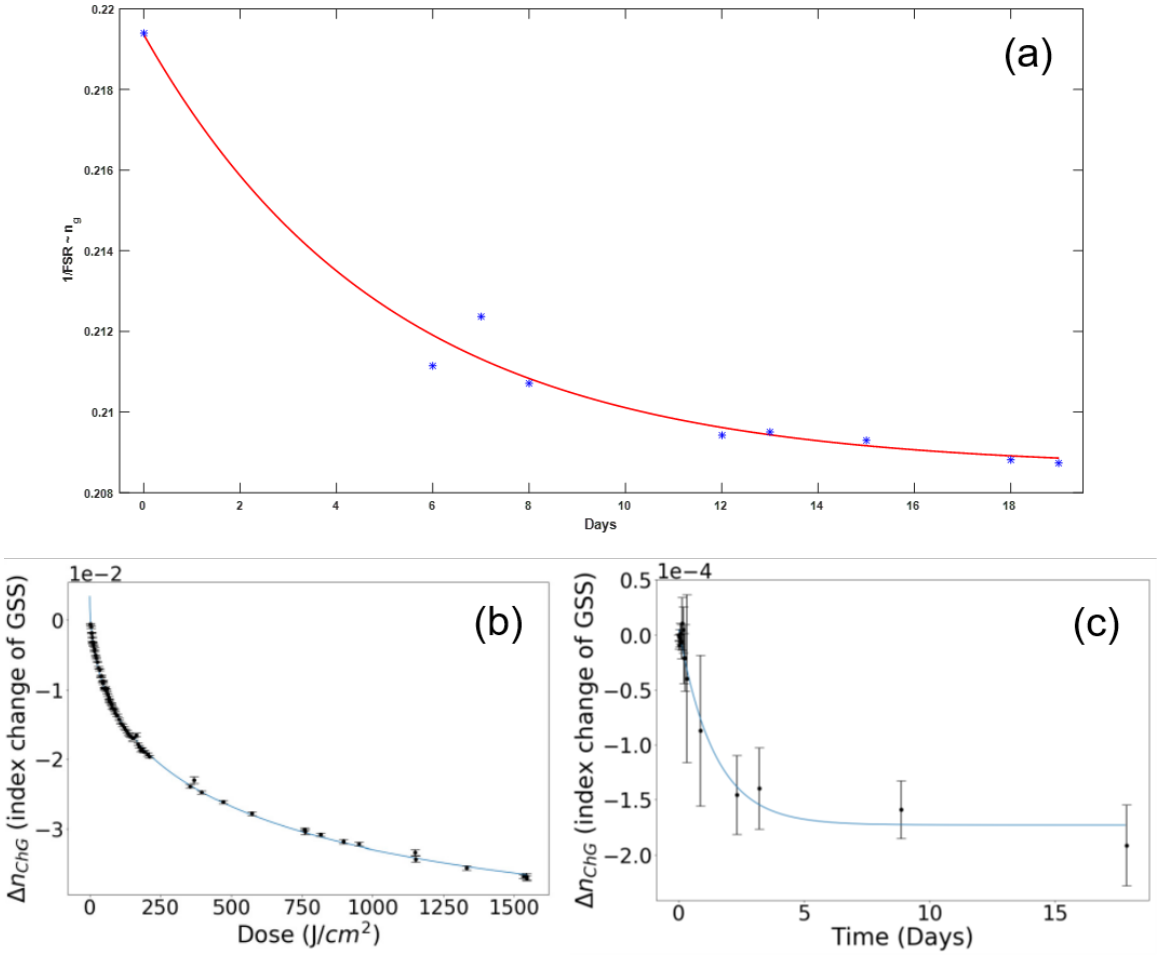

Figure 3-13: (a) Behavior of 1/FSR as a function of time during exposure to a halogen lamp. (b) Refractive index change of GSS during photoexposure. (c) Refractive index change of GSS during aging of annealed devices. The exponential fit gives a time constant of 1.4 days. (b) and (c) from [4].

3.4.2 Temperature

Temperature influences the optical index of materials, which in turn affect the effective index of the waveguide, through their thermo-optic coefficient. Work in our group has measured the thermo-optic coefficient of GSS and SU-8 to be 6.16x10^{-5} /°C and -2.13x10^{-4} /°C, respectively, leading to a temperature-dependent wavelength shift (TDWS) of around -0.072 nm/°C for TE modes in a planar configuration [4]. The deformed geometry of in-buckle resonators slightly changes the confinement factors and hence the TDWS for these resonators, but its magnitude would stay of the same order. This value of the TDWS is consistent with the shift of several hundred picometers observed between measurements on different days, corresponding to a difference of several degrees.

Several methods have been developed to deal with the effect of temperature on the resonant condition of integrated optical cavities. The most straightforward way is to place the sample on a thermostat. However, this wouldn't work for our buckled devices, whose waveguides sit several millimeters above the surface of the stage. Another technique is to use athermal waveguides, designed such that the thermo-optic effect on the core material (usually positive) and the cladding material (usually negative) cancel out [130, 131]. While this isn't technically very challenging to realize, we decided we didn't need to go to such lengths for the proof-of-concept demonstration of our device, notably because the eventual device will be used in an incubator where temperature is kept constant within 0.01°C resulting in a TDWS of less than 1 pm, below our measurement accuracy (see Section 3.3).

We nonetheless needed to be able to correct for the effect of temperature during our calibration measurement, before embedding the sensors in a matrix and placing it in an incubator. We decided to rely on a referencing technique: in addition to the resonator in the buckle aimed at stress sensing, we place a second, "temperature-tracking" resonator along each waveguide, in the "island" region of the device, that doesn't undergo deformation (see Figure 3-14(a)). This second resonator only responds to temperature and can be used as a reference to detect temperature changes. Assuming the temperature uniform in space between the two resonators, we can then calculate the TDWS of the stress-sensing resonator in order to eventually deduce it from the overall measured wavelength shift. To validate this approach, a device with both sets of resonators is measured without any mechanical

constraint applied. The equation giving the TDWS is:

$$\Delta\lambda_{TDWS} = \alpha\frac{n_{eff}}{n_g}\lambda\Delta T + \frac{1}{n_g}\frac{\partial n_{eff}}{\partial T}\lambda\Delta T \tag{3.3}$$

$$= \frac{\alpha n_{eff} + \sigma}{n_g}\lambda\Delta T \tag{3.4}$$

$$= \beta\Delta T \tag{3.5}$$

with $\alpha = \partial n_{eff}/\partial T$ and $\beta = (\alpha n_{eff} + \sigma)/n_g$. Over a small range of temperature, we can neglect the dependence of the coupling coefficient beta on temperature (through the wavelength, the effective index, and the group index), leading to a linear relationship between TDWS and temperature. This equation can be applied to both resonators, with different values for beta as the local geometry varies between the reference resonator on the flat "island" and the sensing resonator in the bent buckle. The two equations can then be combined to yield a linear relation linking the TDWS of the two resonators:

$$\Delta\lambda_{TDWS,sensing} = \frac{\beta_{sensing}}{\beta_{reference}}\Delta\lambda_{TDWS,reference} \tag{3.6}$$

As shown on Figure 3-14(b), a linear relationship is indeed observed between the resonant wavelengths of the sensing resonator and of the reference resonator. This method therefore allows us to correct for the effect of temperature by calculating a value for the TDWS of the sensing resonator with an accuracy of below 10 pm (typical observed standard deviations are around 5 pm). Once again, this uncertainty will be greatly reduced once the sensing device is placed in an incubator where the expected TDWS is less than 1 pm.

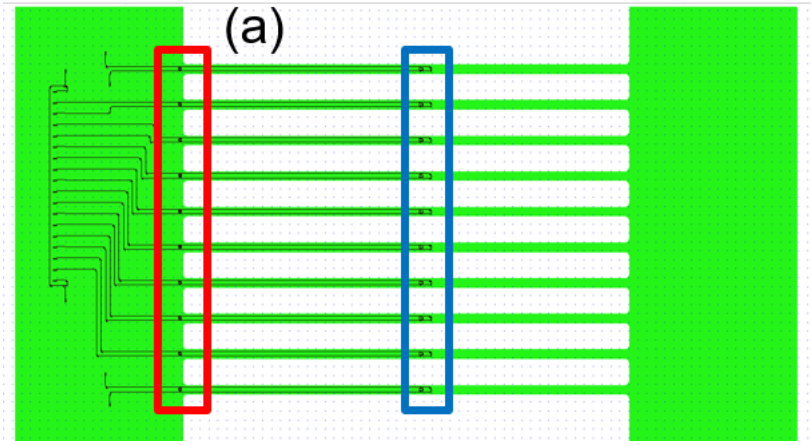

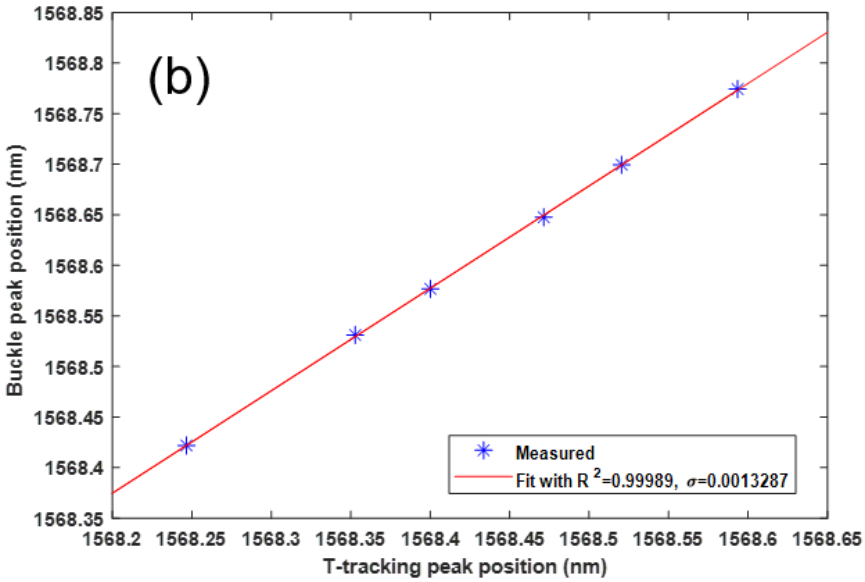

Figure 3-14: (a) 2-D layout of the photonic device on top of the base SU-8 layer. The temperature-tracking, reference rings are boxed in red and the stress-sensing rings are boxed in blue. (b) Resonant wavelength of the sensing resonator as a function of the peak of the reference resonator, without any stress applied to the device. The error bar on the wavelength readings (both vertically and horizontally) are 1 pm, too small to be seen.

3.5 Resonator design

Another unique advantage of integrated optical sensors is the ability to multiplex measurements along a single waveguide – something that isn't possible, for example, along a single electrical wire whose conductivity constitutes the measurable signal. By using several resonators designed to have different resonant wavelengths, all resonators can interrogated at once through a wavelength sweep and their overall response treated to isolate the individual response of each resonator.

While we decided early on in this project to integrate multiple resonators in order to track the local temperature, as described in the previous section, this ability proves critical when it comes to providing a thorough understanding of the mechanical effects at play in the system of interest. One single resonator provides information, through its measured peak shift, about the change in curvature of the buckle at its location. Many steps and assumptions are then required to link this measured local change to the overall mechanical effects in the system under study that caused it: the overall buckle response responsible for the local curvature change needs to be reconstructed (for example through mechanical

simulations), and then used to deduce the forces responsible for the buckle deformation. This process requires assumptions about e.g. the isotropy of the system or the uniformity of the forces, thereby limiting the range of materials, systems, and configurations that can be effectively measured. Multiplexed sensors enable to overcome this limitation. In the limit where resonators would be placed all along the buckle and their individual responses could be perfectly isolated, the change in curvature at each resonator's location could be measured and the new buckle shape reconstructed using:

$$\begin{cases} \theta = \int \kappa ds \\ x = \int \cos(\theta) ds \\ y = \int \sin(\theta) ds \end{cases} \tag{3.7}$$

where κ is the curvature, s is the arc length, θ is the angle between the local tangent and the horizontal, and x and y are the horizontal and vertical position, respectively. In this case, no assumption are needed anymore to find the overall buckle shape and arbitrary deformations can be measured. In particular, this allows for detection of lateral forces even without the implementation of the polarization-resolved sensors introduced in Section 2.3 and additional knowledge about the buckle's and resonator's behavior. The buckle shape is first reconstructed based on the measured peak shift, then its validity is verified by calculating its supposed overall length. If the calculated length matches the actual length, the shape is physical and the curvature changes deduced from the measured peak shifts indeed described the deformation of the buckle. If the calculated length doesn't match the actual length however, we know that this shape cannot describe the reality, as our device isn't stretchable. This points at an incorrect shape reconstruction due to incorrect curvature values, meaning the 1-D model used to calculate the curvature change from the peak shift doesn't apply in this case. Given the large range of validity of our 1-D model, from small to large bending, the likeliest explanation for the departure from the model is the presence of lateral forces causing additional stresses in the buckle due to twisting. Unfortunately, no good model exists for the stresses in a buckle (or beam) undergoing both bending and twisting, thereby preventing from coming up with an analytical model for the twisting-induced peak shift. Our model therefore wouldn't be able to quantify these lateral forces, but would be able to detect their presence.

3.5.1 Ring resonators

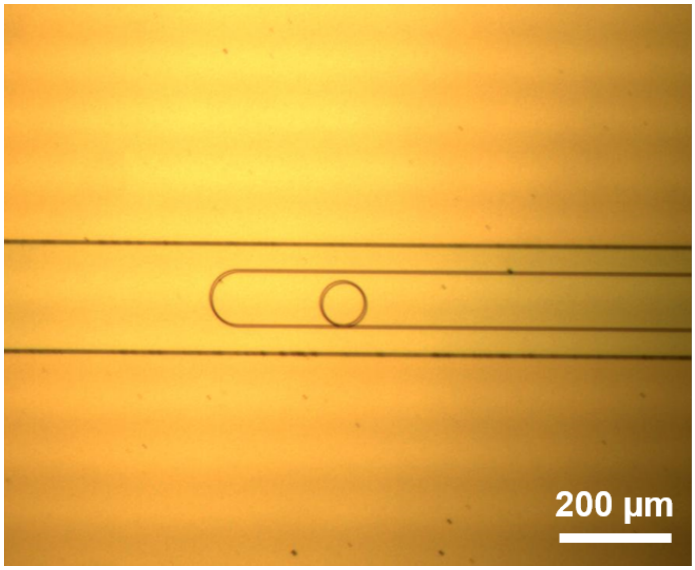

Figure 3-15: Optical microscope image of a ring resonator, in the middle of a strip that will eventually be buckled (device still on its substrate at this point).

Our initial devices used ring resonators, as shown on Figure 3-15. This well-understood resonator design [132, 133] boasts several features that prove advantageous for our purposes. First, it doesn't involve any very small or high-aspect ratio feature, making its fabrication easier. The smallest critical dimension is the gap between the ring and the bus waveguide, typically a few hundred nanometers in our case. Second, its design is easily optimized by varying a couple of factors. The performance parameters of interest for ring resonators are the intrinsic Q-factor, the critical coupling condition (that influences the loaded, or measured, Q-factor), and the free-spectral range (FSR). The Q-factor of a resonant peak is given by:

$$\mathrm{Q} = \frac{2\pi n_g}{\alpha \lambda_r} \tag{3.8}$$

with n_g the group index of the waveguide, α the propagation loss of the waveguide, and λ_r the resonant wavelength. The resonant wavelength is set by the resonant condition:

$$N\lambda = n_{eff} L,\ N \in \mathbb{Z}^* \tag{3.9}$$

with n_{eff} the effective index of the waveguide and L the length of the resonator. The main control parameter for the Q-factor is thus the propagation loss. Inversely, measurement of

the intrinsic Q-factor allows for easy determination of the losses. Assuming the waveguide properties to be set by the fabrication process, we want to ensure that our resonators are operating at critical coupling as the measured Q-factor incorporates both the intrinsic and the external Q-factors:

$$\frac{1}{Q_{loaded}} = \frac{1}{Q_{intrinsic}} + \frac{1}{Q_{external}} \tag{3.10}$$

Critical coupling corresponds to the external Q-factor being equal to the intrinsic Q-factor, such that the loaded Q is maximized. This condition can be numerically found by simulating the coupling region between the bus waveguide and the resonator. In the case of a standard ring (pure circle of fixed radius), the single parameter influencing the coupling is the gap between the ring and the bus waveguide. However, the coupling coefficients are extremely sensitive to fabrication imperfections that influence wave propagation in this region. A practical way of finding critical coupling therefore consists in doing a calibration run by sweeping the coupling gap, measuring the Q-factor of the resonators, and selecting these with the highest Q value – that are thus at critical coupling. Finally, we need to be able to tune the FSR of our resonators as this is what allows us to distinguish between them. The FSR is given by:

$$\text{FSR} = \frac{\lambda_r^2}{n_g L} \tag{3.11}$$

The FSR can be adjusted simply by changing the length, i.e. the radius, of the ring. Our final optimized parameters were: radii of 30, 40, and 45 µm for the three different sets of rings (one for temperature tracking and two for curvature sensing), and a gap of 500 nm.

Ring resonators nonetheless present certain drawbacks. Isolating the response from multiplexed sensors, identified by their unique FSR due to their different radius, requires post-processing of the optical data. This process becomes more and more complex as the number of sensors grows, as can be seen on the spectrum shown on Figure 3-16 where three ring resonators with different FSRs are integrated on a single waveguide. With just three rings, manual processing already becomes insufficient to distinguish the FSR and identify the peaks as belonging to each resonator. Calculating the power spectral density (PSD) of the spectrum gives the values of the FSR. Then the wavelength difference between peaks can be extracted to identify them. This computerized process however also has its limits when going to a large number of resonators, as the FSRs get closer in value since the available range of ring radii is constrained by the minimum bending radius of the waveguide (around

30 µm in our case) on one end and by the width of the buckle on the other end.

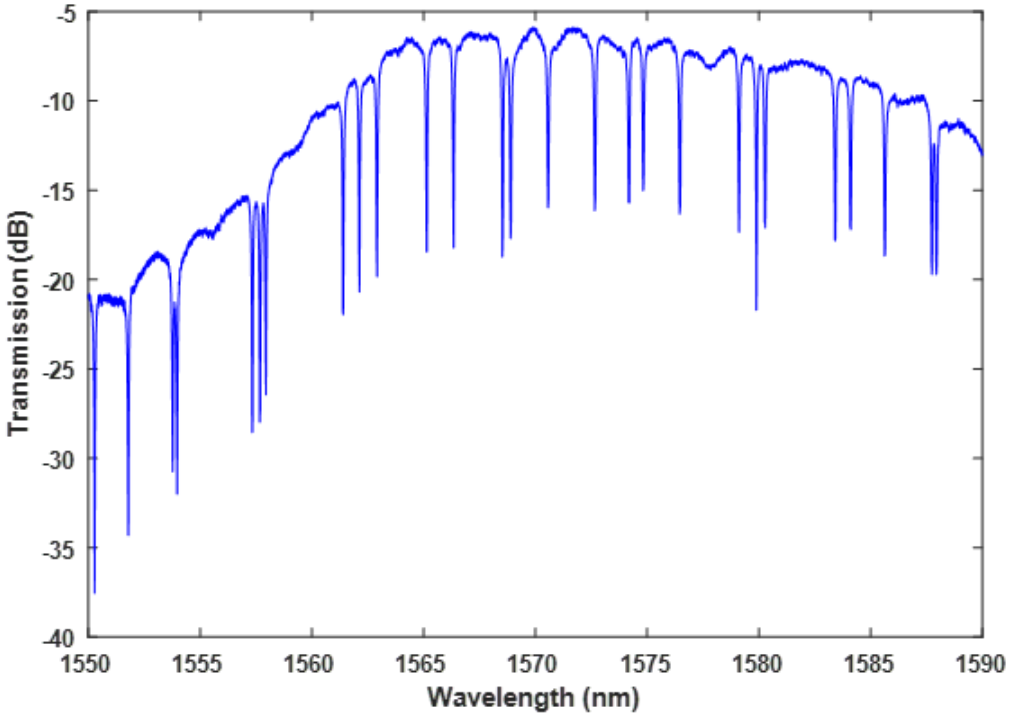

Figure 3-16: Transmission spectrum of a waveguide coupled to three rings resonators of 30, 40, and 45 µm radius, leading to FSR ratios (relative to the smallest FSR of all three rings) of 1, 1.33, and 1.5.

3.5.2 Side-coupled photonic crystal cavity

We turned to another type of photonic resonator to solve the issues caused by multiplexing ring resonators, namely photonic crystal cavities. Photonic crystals owe their name and working principle to their similarity with actual crystals. When a portion of space, or an area if in 2-D, of an otherwise optically transparent material is patterned with a regular lattice, a photonic bandgap is created, preventing propagation of light whose wavevector lies in the bandgap [134]. Along a waveguide, this can be done by e.g. periodically varying the width of the waveguide, or by inserting a periodic array of holes in the waveguide [135]. As light within the bandgap cannot propagate in the waveguide, the photonic crystal acts as a mirror at the bandgap frequencies.

Photonic crystal cavities are particularly poised for multiplexed sensing thanks to their ability to produce a single peak in their transmission spectrum. This is realized by intro-

ducing a defect in their lattice of a photonic crystal, thereby creating a state in the bandgap that allows for light propagation. This gives rise to a peak in the transmission spectrum of an in-waveguide cavity, that is, a low transmission at all wavelengths but the resonance. This is not only inconvenient in practice as it makes for example aligning to the waveguide difficult since alignment is done precisely by maximizing the transmitted power, but also prevents from having another such cavity along the same waveguide – as no power would reach it. For a side-coupled cavity, located next to the waveguide, this however translates to a peak in absorption (i.e. a dip in transmission) as only light at the wavelength of the defect state is able to couple out of the waveguide into the photonic crystal. The exact position of the peak in the spectrum is determined by the defect state, that is, by the geometrical defect introduced in the lattice. We can therefore control the position of the peak by changing the geometrical parameters of the cavity. Placing several of these resonators, designed to have their peaks at different wavelengths, along a single waveguide realizes the intended multiplexing.

Photonic crystal cavities however present several drawbacks. First, their fabrication is trickier than ring resonators as the critical dimensions involved as smaller, down to tens of nanometers. This requires precise optimization of the e-beam dose to obtain the intended dimensions, as well as of the RIE process to etch the high aspect ratio features. Photonic crystals also involve repeating patterns, which at this small lengthscale cause issues during e-beam writing due to proximity effects, thus requiring further optimization. Second, optimizing their geometry is more complicated because of the many parameters involved and the high computational cost of their simulation [136–138]. Finally, the relatively low index contrast ($n_{wg}/n_{clad} = 1.41$) of our set of materials makes it more difficult to achieve a photonic bandgap and thus increasing the sensitivity to fabrication imperfections [139,140].

As previously said, there are several ways of creating a photonic crystal along a waveguide. Following Mandal *et al.* [141] and relying on an approach to get ultra-high Q-factor [142], we initially wanted to use nanoholes periodically defined in the waveguide. However, these demonstrations were all made on a silicon photonics platform with an index contrast of 2.47 at 1550 nm. We realized through simulations that the low index contrast of our set of materials (Δn = 0.65 between GSS and SU-8) resulted in a much smaller photonic bandgap, making it difficult to experimentally hit the right parameters needed to give rise to the bandgap. Also, small nanoholes are particularly challenging to realize because of the

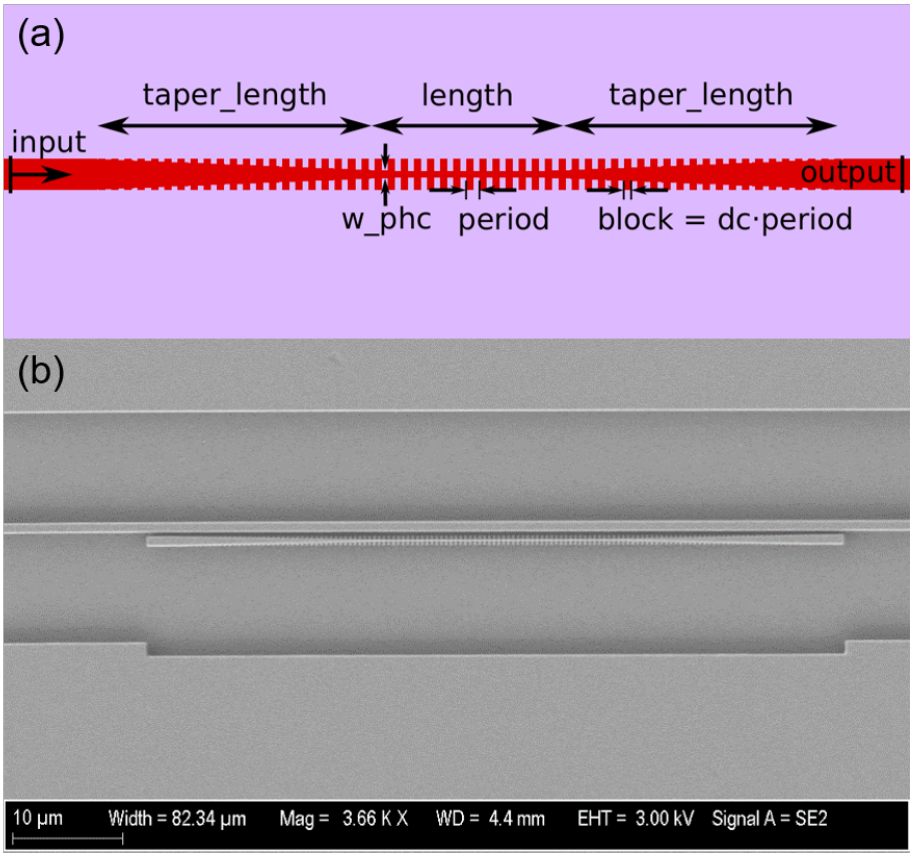

Figure 3-17: (a) Schematic of the corrugated sidewall waveguide design used, with the parameters defined. "dc" stands for "duty cycle". For a side-coupled cavity, an additional parameter would be the gap between the cavity and the bus waveguide. From [5]. (b) Scanning electron microscope (SEM) image of a fabricated side-coupled photonic crystal cavity resonator.

high aspect ratio etching they require, with only the top area of the nanoholes available for the gases to diffuse in and out to the surface being etched. In contrast, a design previously demonstrated in our group relies on periodic modulation of the waveguide width. There, small features are easier to realize as gases can also get to the surface being etched from the side. We therefore used this design sometimes called a corrugated waveguide, as its in-waveguide version has been shown to work for our combination of materials [82]. The geometry of such a photonic crystal is shown on Figure 3-17(a). Given the different fabrication process between the previous demonstration and our device, we couldn't directly reuse the exact same parameters previously optimized, yet we were able to use these as a starting point for our own optimization. The difference, if any, would be caused by the fabrication, therefore we did not need to simulate the device anew and focused instead on sweeping

through values of the parameters involved in the cavity. Namely, we varied the period and the duty cycle around 455 nm and 0.5, the width of the photonic crystal region around 150 nm, the taper length around 20 µm, and the gap around 100 nm. As expected, designs with longer taper lengths showed higher Q-factors thanks to better mode matching [143]. The resonance was also found to blue-shift as the width of the photonic crystal increases. Eventually, we were able to find parameters yielding a single resonant peak in the wavelength range of interest, as shown on Figure 3-18(a). Figure 3-18(b) shows that integrating two such resonators with different photonic crystal widths (thus different resonances) along a single waveguide gives the expected two separate peaks, thereby enabling the intended multiplexing. We note that the peak of Figure 3-18(a) isn't located exactly at the same wavelength as any of Figure 3-18(b). This can be attributed to slight fabrication differences even within a single chip: for example the e-beam current may drift during the write, resulting in features of different size even though they were supposed to be the same, or etching might happen at different rates near the edges or the center of the chip. This however isn't an issue as we are only interested in the peak shift on the one hand, to measure the influence of external stimulations, and the relative position of peaks within a single spectrum on the other hand, to identify the resonators that created them. As long as the relative position of peaks induced by varying a parameter is conserved, we can link each peak to a resonator. This is indeed the case on Figure 3-18(b).

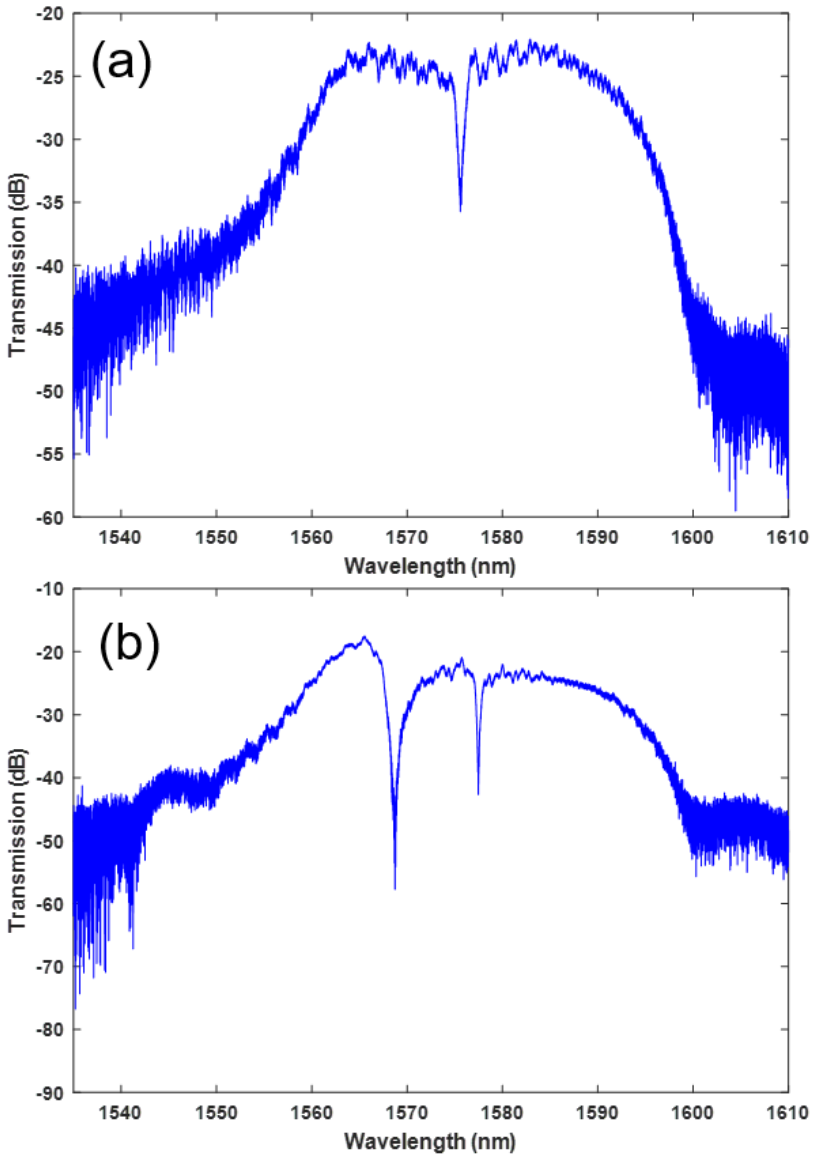

Figure 3-18: Transmission spectra of devices with (a) a single side-coupled photonic crystal cavity resonator, yielding a single resonance peak, (b) two side-coupled cavity resonators with different photonic crystal widths, yielding two peaks at different wavelengths.

Chapter 4

Sensor calibration and sensitivity

4.1 Calibration by comparison with mechanical simulations

The end goal of a measurement using our sensors is a value for the strain or stress in the matrix of interest. For our sensors to provide this information, we need to be able to relate the measured optical peak shift to the deformation of the buckle. Determination of this relationship is the purpose of the calibration, in which we need to measure the sensor's response to a known perturbation. An optical measurement as described in Section 3.3 suffices for the optical characterization. For the perturbation however, we need a way to deform the buckles in a controllable and measurable way, such that the strain at the sensor's location is known.

4.1.1 Controlled mechanical deformation

Our initial thoughts involved calibrating the sensors in a configuration similar to the one they would be used in eventually, that is, embedded in a matrix. As explained in Section 2.2, in a process similar to what would be used for cell culture, we would place an enclosure around the buckle to define a micro-reactor volume. The matrix of interest, for example a hydrogel, could then be poured in the enclosure and around the buckles. This process is represented on Figure 2-3. We thought that we would perturb the matrix, for example by exerting a known force at a given point of its top surface. We would then measure the response of the sensors and simulate the mechanical deformation induced by the perturbation, yielding the desired strain-optical relationship. We quickly realized however that there were

several issues associated with this approach. The main issues had to do with the matrix. Its elastic modulus had to be known such that the simulations results be accurate. The matrices we were considering, at first polydimethylsiloxane (PDMS) and then agarose gel, are created by mixing several components whose ratio determine the stiffness of the resulting soft material [144–146]. We couldn't however be sure that we were getting the same moduli as reported in literature for the ratios we used, and it proved difficult to measure their stiffness by ourselves. Additionally, both PDMS and agarose (which, as a hydrogel, is mostly made out of water) have high CTE of 310 and 207 ppm/°K, respectively. For a sample of about 1 cm, this only represents an expansion or contraction of a few micron, which wouldn't impact our measurements. But a lamp is used during the measurement to look at the coupling region and align the fibers to the grating couplers – this lamp can induce a temperature inhomogeneity in the matrix up to tens of degrees we estimate, which would deform the matrix in ways difficult to reproduce in simulations and therefore to control.

We therefore decided to abandon this route and deform the buckles directly. To choose the deformation to apply, we kept in mind that this configuration would then need to be simulated in order to extract the mechanical effects. Also, position is easier to measure precisely than force using commonly available motion control equipment. We relied on a simple deformation: the linear displacement of a rigid boundary (practically speaking, a block of stiff material) to press down on top of the buckles. The picture and arrows on Figure 4-1 depict this configuration.

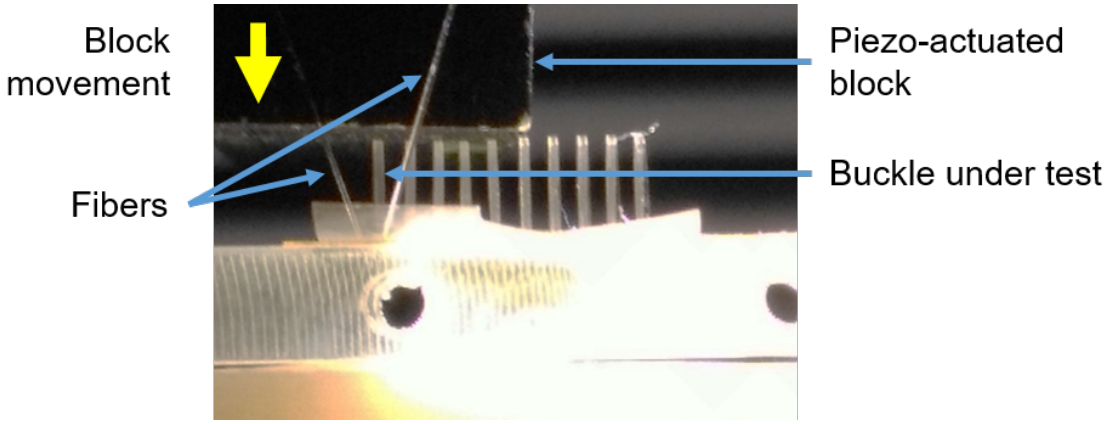

Figure 4-1: Side-view picture of the calibration setup, with fibers for grating coupling into the waveguide in the buckle under test, and a block to press down on the buckle. The picture is taken along the axis of the buckle.

In order to get repeatable and precise deformation, we used a piezoelectric actuator (TRA25CC, Newport) to control the vertical position of the block. The initial position was chosen such that the block would barely not touch the top of the buckle. It was then lowered in steps of 0.1 or 0.2 mm. After each block movement, an optical spectrum was acquired. The block was lowered down to 1.3 mm below its original position, then brought back up in the same increments, and several such rounds of lowering and raising were performed. The acquired spectra were analyzed to extract the peak shift of the buckle resonators. However, this peak shift included both the deformation-induced and temperature-induced shifts. The spectra acquired at the initial position, when no deformation is applied to the buckle, were thus used to calibrate the relationship between the temperature-dependent wavelength shifts of the temperature-tracking resonator and the pressure-tracking resonator, as described in Section 3.4.2. This relationship was then applied to the other spectra to calculate the temperature-induced peak shift, subtract it from the total measured peak shift, and thereby isolate the deformation-induced peak shift. This last value could finally be linked to the height change of the block that caused the deformation causing the peak shift, as shown on Figure 4-2.

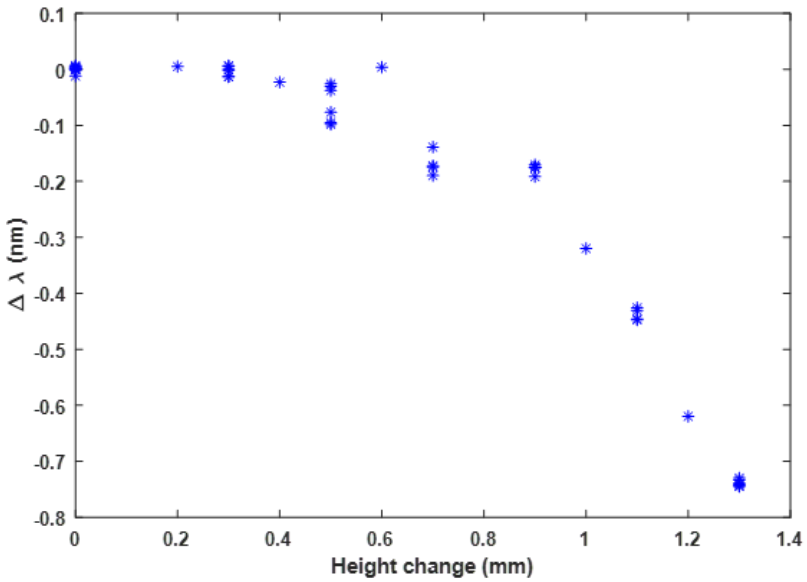

Figure 4-2: Deformation-induced peak shift as a function of the height change of the block. Positive height change means the block was lowered. The error bar on the wavelength measurement is 10 pm (0.01 nm), too small to be seen on the graph.

4.1.2 Mechanical simulations

The other side of the calibration process consists in calculating the value of the strain at the sensor's location when the deformation is applied. The configuration used, with the buckle constrained between the stage and an upper block as described in the previous section, is commonly referred to as "the constrained elastica" – a beam under buckling constrained in the vertical direction. Its treatment has been the subject of a number of numerical and analytical studies [147–150]. Yet no analytical solution was found in a general case. We therefore also rely on numerical simulations to study this problem. We used the finite element modeling (FEM) software COMSOL, specifically its Solid Mechanics module, to simulate the behavior of the system under the applied constraints. Thanks to the symmetries of the problem, with the block moving only vertically and the buckle standing in a plane, we were able to use a 2-D model, thereby reducing the time needed for the simulations.

The first step was to define the geometries involved, namely the stage (lower block), the buckle, and the upper block. The shape of the buckle is known thanks to our treatment of the large-deformation beam-buckling problem, as discussed in Section 2.2.2. The geometrical inputs needed for determination of the shape's parameters, the total length of the buckle and its span, are controlled by our experiment design: the total length on the buckle depends on the initial pattern fabricated in 2-D and thus defined lithographically, while the span is determined by the spacer used in the buckling process. Nonetheless, a problem here is that this exact solution for the buckle shape involves the elliptic integrals of the first and second kind, which are unknown to COMSOL. Instead, we used the linearized expressions of the elliptic integrals to define the buckle shape. For the incomplete elliptic integral of the first kind around $p = 0$, we have, to the 6th order in p:

$$E(\phi, p) = \phi + \frac{-2\phi + \sin(2\phi)}{8} p^2 + \frac{1}{256} \left[-12\phi + 8\sin(2\phi) - \sin(4\phi)\right] p^4 + \frac{1}{3072} \left[-60\phi + 45\sin(2\phi) - 9\sin(4\phi) + \sin(6\phi)\right] p^6 + O(p^7) \quad (4.1)$$

Similarly for the incomplete elliptic integral of the second kind:

$$F(\phi,p)=\phi+\frac{2\phi-\sin(2\phi)}{8}p^2+\frac{3}{256}\left[12\phi-8\sin(2\phi)+\sin(4\phi)\right]p^4 + \frac{5}{3072}\left[60\phi-45\sin(2\phi)+9\sin(4\phi)-\sin(6\phi)\right]p^6+O(p^7) \quad (4.2)$$

We need to verify that this approximation yield values for the shape of the buckle that are accurate enough, that is, the curvature difference caused by the approximation needs to be smaller than the sensitivity of the sensor. Given the 10 pm peak position accuracy set by the temperature correction (see Section 3.4.2) and a strain-optical coupling around 1 nm/% strain (based on previous works in our group [82]), we expect a sensitivity around 0.01% strain at the resonator's location. This translates to a 0.02 mm^{-1} difference in curvature, assuming a resonator 5 µm away from the neutral axis of the buckle (as is the case in our proof-of-concept device). A plot of the error on the curvature of the buckle using either the 4th order or 6th order expansion is given on Figure 4-3. We can see that the error induced by the linearization to the 4th order is adequately small for our purposes, as the difference with the exact curvature value never exceeds 0.02 mm^{-1}. If a greater sensitivity were to be needed however, using the 6th order approximation would bring down the error to below 0.005 mm^{-1}. We therefore used the 4th-order linearized expression of the elliptic integrals to define the buckle shape in COMSOL. The geometry of the simulated system is shown on Figure 30 (with its mesh): the lower block represents the fixed stage, onto which the buckle is fixed at its ends, and the upper block is brought down and makes contact with the buckle.

We then need to specify the materials used and their mechanical properties. Previous work has shown that the influence of the GSS waveguides embedded in SU-8 on the overall properties of the structure is negligible. We therefore model the buckles as being purely SU-8, with a Young's modulus of 4.02 GPA [151], a Poisson ratio of 0.22, and a density of 1190 kg/m^3. The blocks just need to be assigned a much harder material âĂŞ we chose aluminum, with a Young's modulus of 70 GPa. The mechanical constraints of the system are mostly straightforward. The lower block (i.e. the stage) is fixed. The upper block has a prescribed vertical displacement, and is fixed otherwise. The buckle has both ends fixed to the lower block, but is otherwise free to move. One constraint however required careful definition: the contact between the blocks and the buckle, to ensure that lowering the upper block would indeed deform the buckle, while the lower block would indeed prevent the buckle to move

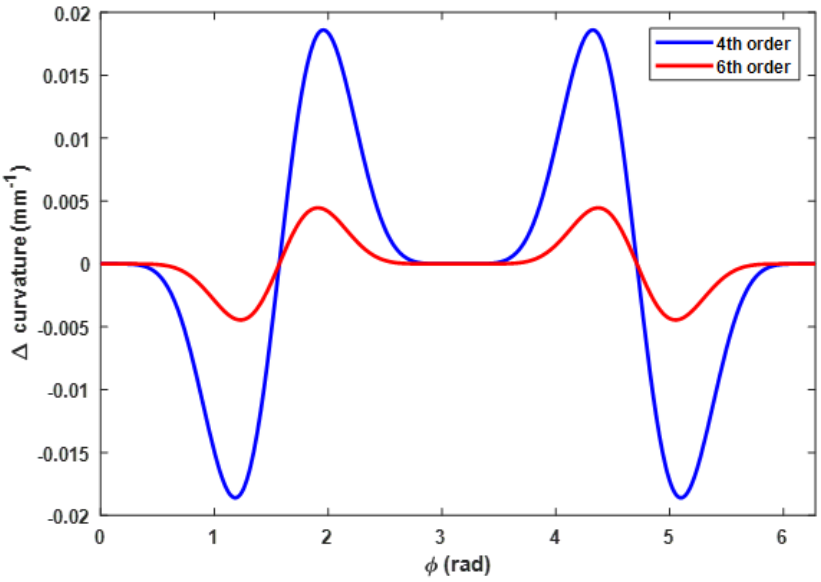

Figure 4-3: Curvature difference along the buckle with respect to the exact curvature (calculated using the exact values of the elliptic integrals) when using the elliptic integrals expressions linearized to the 4th or 6th order.

downwards. In COMSOL, the contact constraint is defined by two parameters, a "contact penalty factor" and an "initial contact pressure". The penalty factor represents the stiffness of the interface but also influences the convergence of the simulations. A low penalty makes it easier for the simulation to converge, but might lead to interpenetration of the surfaces. Inversely, a high penalty prevents interpenetration but might prevent convergence. The default value for the penalty factor is:

$$\min(1e-3*5segiter,1)*solid.Eequ/solid.hmi \tag{4.3}$$

where the first part of the expression (within the "min") is a scaling function that gradually ramps up the contact penalty earlier in the iterations of the simulation solver, and the second part is a function that estimates the average Young's modulus of materials at the interface and divides it by an estimate of the average mesh size at the contact interface. Using $\min(3e-3*5segiter,1)*solid.Eequ/solid.hmin_dst$ proved to work for our entire range of deformations. For the initial contact pressure, we cycled values from 10^{-3} to 10^{8} $\mathrm{N/m^2}$ looking to have the simulation converge. 1 $\mathrm{N/m^2}$ worked for the deformations we considered.

Finally, the vastly different lengthscale of the different objects in this system required us to adapt the mesh for each region of the simulation. The blocks, top and bottom, are several millimeters wide and tall, and their displacements are simple (the lower one is fixed, the upper one moves down by a set distance). They therefore do not require a very fine mesh. On the other hand, the buckle is only 10 µm thick and undergoes a large deformation that we wanted to track accurately. We used a very fine mesh for the entire buckle domain. In addition, as mentioned in the previous paragraph, the forces at the contact points between the buckle and the blocks heavily influence the results of the simulation. We thus wanted these regions to be simulated as accurately as possible, which we ensured by also meshing these boundaries with the finer mesh. Figure 4-4 displays a zoomed-in image of the mesh, showing the difference between the coarse and fine mesh regions. The mesh precision is controlled by the maximum element size allowed. We verified that setting it to 0.0575 mm (the value for "extremely fine", the highest predefined mesh precision in COMSOL) yielded the same results as smaller values, while 0.115 mm (the value for "extra fine", the second highest predefined precision) caused convergence issues. The simulations were thus run with the "extremely fine" setting for the buckle and boundary regions.

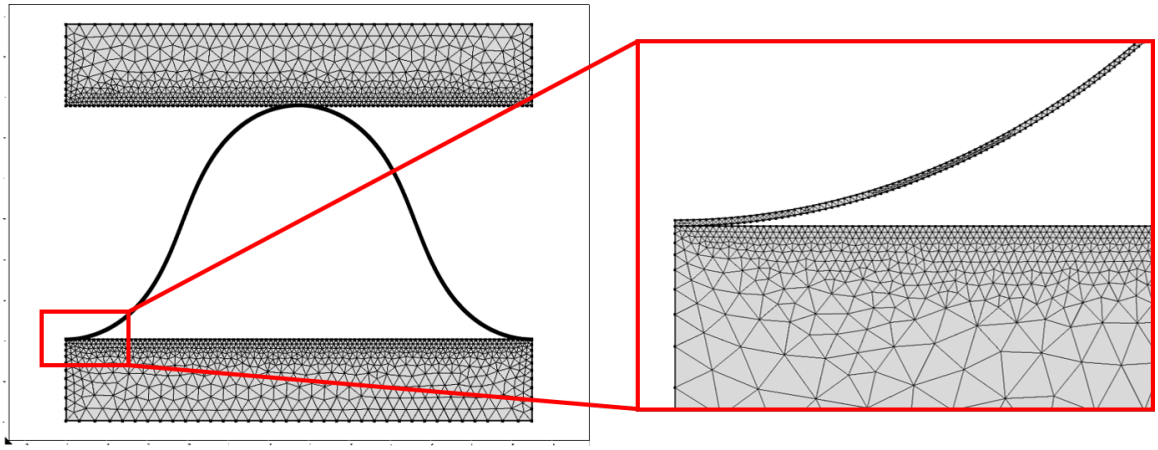

Figure 4-4: Screenshot of the mesh generated in COMSOL for the FEM simulation. The inset shows the finer mesh in the buckle and at the contact points.

The results of the simulations include the displacement field of the buckle. An example of such a displacement is shown on Figure 4-5. We then had COMSOL calculate the curvature of the buckle in its deformed state, and exported that data to compare it to the curvature in the initial state. We could thus calculate the change in curvature along the buckle due to the deformation. Finally, knowing the position of the sensor along the buckle, and using the

relationship between curvature and strain, we calculated the change in stress as a function of the magnitude of the deformation (in this case, the height change of the upper block) – our objective for these simulations (see Figure 4-6).

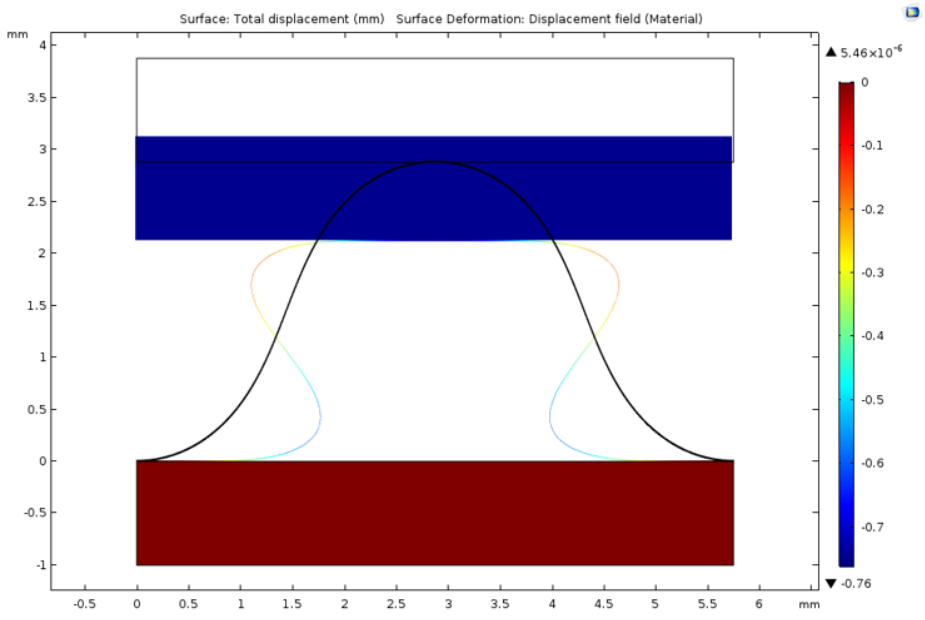

Figure 4-5: Screenshot of a COMSOL simulation output. The black lines correspond to the initial geometry; the colored bodies correspond to the final geometry. The color represents the amount of displacement (in mm) in the vertical direction.

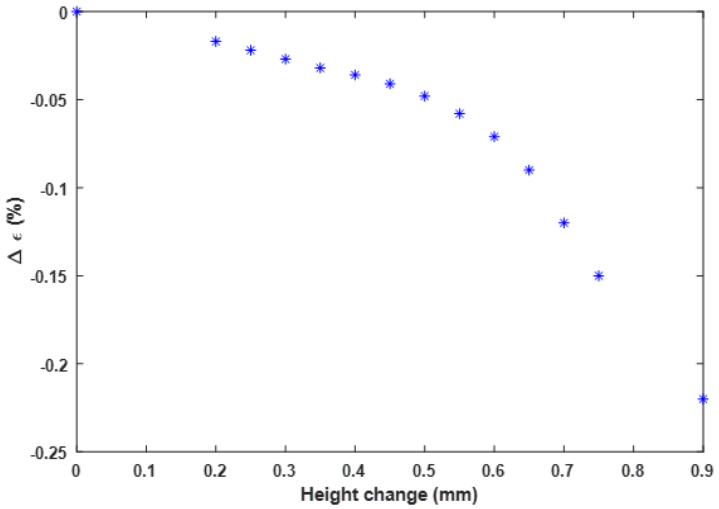

Figure 4-6: Plot of simulated change in strain as a function of the displacement of the upper block.

4.1.3 Strain-optical coupling coefficient

The experimental measurements and simulation results were finally brought together in order to calculate the strain-optical coupling calibration curve for the sensor under consideration. Figure 4-7 plots together the measured peak shift and the simulated strain change as a function of the displacement of the upper block. As will be discussed later on, the "zero" height point, at which the block supposedly starts to press down on the buckle, had to be adjusted between the two curves.

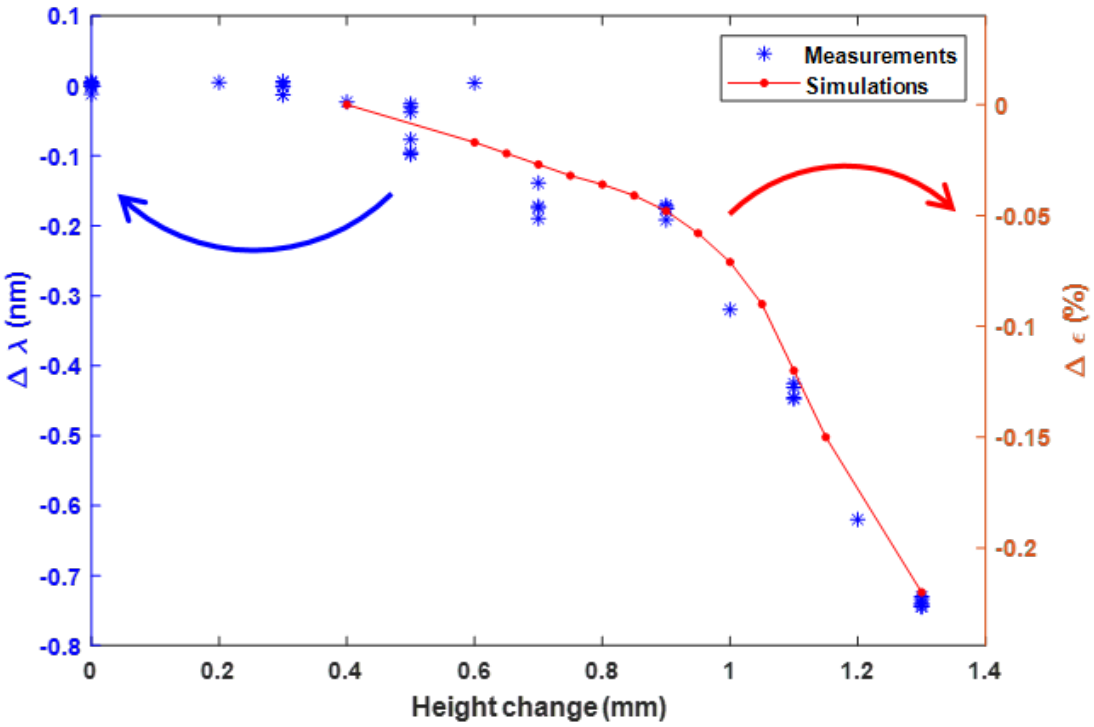

Figure 4-7: Common plot of measured peak shift and simulated stress change versus upper block displacement.

The measurement and simulations results can finally be combined to yield the desired strain-optical relationship, as shown on Figure 4-8. The relationship is linear as expected, with a slope of 3.2 nm/%. This value should apply to all sensors with a similar geometry and a similar set of materials. In that respect, it is notably independent of the exact buckle shape and of the position of the resonator with respect to the neutral axis, as both these contributions are accounted for in the value of the strain at the resonator's location.

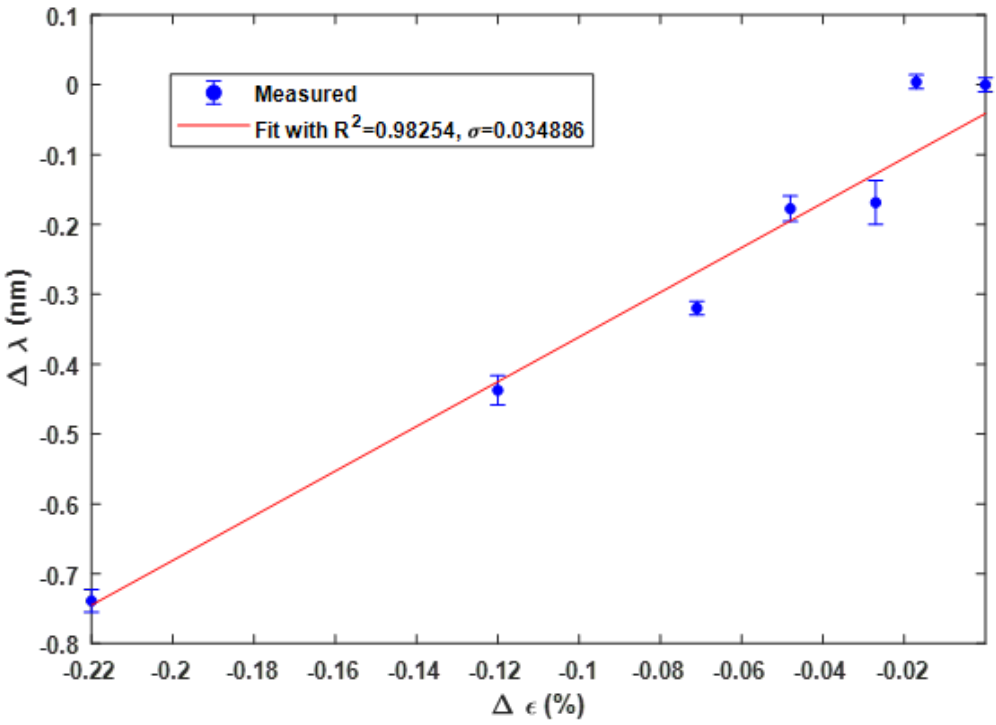

Figure 4-8: Strain-optical calibration curve The linear fit equation is $\Delta\lambda = 3.2 * \Delta\epsilon - 0.04$nm.

While this calibration procedure yields the desired information, it relies on several parameters that are determined visually or semi-visually. The shape of the buckle, taken as an input by the mechanical simulations, and the position of the sensor, used to calculate the strain at the sensor's location, depend on the exact values of the buckle's total length and its span. These are theoretically defined lithographically, yet we can see on Figure 4-9(a) that the edges of the buckle do not always coincide with these of the tape, making for effectively shorter buckles. The tape also may not be parallel to the edges of the stage, making for a span varying from the intended one. Most importantly, not knowing the exact onset of buckling means an imprecise knowledge of the sensor's position along the buckle. Considering the increased difficulty to perform these visual measurements on actual devices that are transparent (see Figure 4-9(b)), we estimate their uncertainty at 0.2 mm at minimum. Given the rate of variation of the curvature along the buckle (see Figure 2-5), this translates to uncertainty in the strain at the sensor's location on the order of 1%, much greater than the predicted 0.01% accuracy given by optical measurements. Another parameter determined visually is the "zero" height position of the block used to process down on the buckle. As

can be seen on Figure 4-7, as we lower the block by steps of 0.1 mm from the apparent point of contact, no peak shift is detected for the first few steps, until approximately 0.2 to 0.4 mm height change. Where the block effectively starts pushing down on the buckle influences the correction to be applied when comparing the simulation results to the experimental data: in practice, the red curve depicting the simulated strain on Figure 4-7 can be shifted left or right to have the zero-height of the experiment match the no-deformation point of the simulations. As the strain and thus the peak shift only increase slowly at the onset of deformation, figuring out the position of that onset cannot be done with precision.

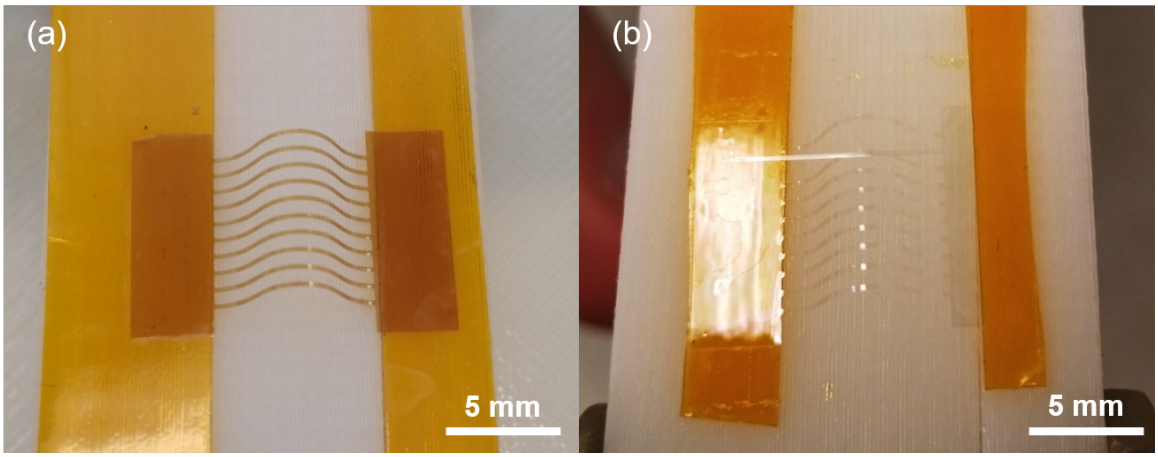

Figure 4-9: Pictures of buckled devices. (a) The red color is due to a blanket layer of GSS remaining between the two layers of SU-8. (b) Functional device. The 2nd buckle starting from the top is broken.

4.2 All-optical calibration

We designed a calibration procedure based solely on optical measurements. This method relies on measuring the peak position for two sensors along the buckle for two different buckle spans (buckle compressed more or less). Even if the original span is unknown, because of non-parallel tape edges for example, the difference in spans can be precisely controlled by adding a spacer of known thickness. Using the notations from Section 2.2, we start with 9 unknowns in such a configuration: total length of the buckle L_{tot}, spans L_1 and L_2, parameters for each span k_1, p_1 and k_2, p_2, and positions of the two sensors ϕ_a and ϕ_b.

We know the difference in spans, and we can use the previous conditions on the total

length and the spans:

$$\begin{cases} L_1 - L_{tot} = \Delta span_1 \\ L_1 = \dfrac{1}{k_1}\left[2E(2\pi, p_1) - F(2\pi, p_1)\right] \\ L_{tot} = \dfrac{4K(p_1)}{k_1} \\ L_2 - L_{tot} = \Delta span_2 \\ L_2 = \dfrac{1}{k_2}\left[2E(2\pi, p_2) - F(2\pi, p_2)\right] \\ L_{tot} = \dfrac{4K(p_2)}{k_2} \end{cases} \tag{4.4}$$

Two more equations are given by the known distance between the two sensors ΔL_{a-b}, defined lithographically, and that must hold true in both buckling configurations:

$$\begin{cases} \Delta L_{a-b} = \int_{\phi_a}^{\phi_b} \sqrt{x_1'(\theta)^2 + h_1'(\theta)^2} d\theta \\ \Delta L_{a-b} = \int_{\phi_a}^{\phi_b} \sqrt{x_2'(\theta)^2 + h_2'(\theta)^2} d\theta \end{cases} \tag{4.5}$$

The final equation is provided by the optical measurements. Measuring the absolute position of the resonant peak of a sensor doesn't provide any information, however the peak shift between two different configurations is related to the difference in strain by a linear relation, as proven by our previous works and in the previous section:

$$\Delta\lambda = \alpha\Delta\epsilon \tag{4.6}$$

The strain itself is linearly related to the curvature, which can be computed from the buckle shape, by:

$$\epsilon = \delta \cdot \kappa \tag{4.7}$$

with δ the position of the resonator with respect to the neutral axis of the buckle, and κ the curvature. We therefore have, with on the left-hand side the analytical expressions and on the right-hand side the measured values:

$$\begin{cases} \Delta\kappa_a = \alpha'\Delta\lambda_a \\ \Delta\kappa_b = \alpha'\Delta\lambda_b \end{cases} \tag{4.8}$$

with $\alpha' = 1/\alpha\delta$ the coefficient linking peak shift to curvature. Because the value of α is still

unknown at this point – its determination is precisely the goal of the calibration process – we take the ratio of these two equations:

$$\frac{\Delta\kappa_a}{\Delta\kappa_b} = \frac{\Delta\lambda_a}{\Delta\lambda_b} \tag{4.9}$$

To summarize, we have a system of 9 equations with 9 unknowns:

$$\begin{cases} L_1 - L_{tot} = \Delta span_1 \\ L_2 - L_{tot} = \Delta span_2 \\ L_{tot} = \dfrac{4K(p_1)}{k_1} \\ L_{tot} = \dfrac{4K(p_2)}{k_2} \\ L_1 = \dfrac{1}{k_1}\left[2E(2\pi, p_1) - F(2\pi, p_1)\right] \\ L_2 = \dfrac{1}{k_2}\left[2E(2\pi, p_2) - F(2\pi, p_2)\right] \\ \Delta L_{a-b} = \int_{\phi_a}^{\phi_b} \sqrt{x_1'(\theta)^2 + h_1'(\theta)^2}\, d\theta \\ \Delta L_{a-b} = \int_{\phi_a}^{\phi_b} \sqrt{x_2'(\theta)^2 + h_2'(\theta)^2}\, d\theta \\ \dfrac{\Delta\kappa_a}{\Delta\kappa_b} = \dfrac{\Delta\lambda_a}{\Delta\lambda_b} \end{cases} \tag{4.10}$$

Solving this system not only allows for determination of the buckle shape parameters but also for calculation of the calibration constant itself: once the shape parameters are known, Equation (4.10) gives a value for α' and thus α.

The precision of this method is this of the peak position measurement. With $\Delta\lambda \leq 1$ pm and a peak shift between configuration on the order of 100-1000 pm, this precision is below 1%. Finally, solving this 9-equation system might prove difficult for the computer. However, this method can be used in conjunction with any other calibration technique (that could rely on geometrical measurements, for example) to confirm the results.

4.3 Sensitivity analysis

The strain-optical relationship obtained in the previous sections relates the optical measurement to the local strain at the resonator's position. However, the information of interest for the end-users of our device is the strain in the matrix. These two strain values,

at the resonator's location and in the matrix, need to be linked. This can be done by considering the force needed to change the bending radius of the buckle around the sensor – which is what the sensor effectively measures. The detailed derivations of the following results are presented in Appendix A. The expression for the force needed to bend the buckle is (geometrical notations are defined on Figure A-1):

$$F = \frac{-E_b L w t^3}{12R^3} \cdot \frac{1}{-\frac{L}{R}\cos(\frac{L}{2R}) + 2\sin(\frac{L}{2R})} \tag{4.11}$$

We then use this expression to evaluate several performance metrics of our sensors. First, we can calculate the range of materials that are amenable to sensing with our device. To that end, we look at the condition for the buckle to follow the matrix's deformation: the additional force needed to bend the buckle further must be less than the force applied by the matrix. This results in a condition on the modulus of the matrix:

$$E_{matrix} \geq \frac{48}{5}\frac{Rt^3}{L^4}E_{buckle} \tag{4.12}$$

For a device made of SU-8 with $E_{buckle} = 4.02$ GPa, a spacing between resonators $L = 1$ mm, a bending radius $R = 1$ mm, and a buckle thickness $t = 2$ µm, this yields a minimum modulus of 300 Pa for the matrix. This means that our sensors are well able to perform sensing within usual biological matrices, that typically have moduli greater than 1 kPa. We can also estimate the sensitivity of our device in a given matrix. In this case, we link the smallest detectable peak shift, $\Delta\lambda = 1$ pm according to Section 3.4.2, to the corresponding force on the buckle, and change in strain in the matrix that must have caused it:

$$F = \frac{-E_b L w t^3}{12R^3} \cdot \frac{1}{-\frac{L}{R}\cos(\frac{L}{2R}) + 2\sin(\frac{L}{2R})} \tag{4.13}$$

$$\Delta\epsilon_{matrix} = \frac{4}{5}\frac{t^3}{\delta L^2} \cdot \frac{E_{buckle}}{E_{matrix}} \cdot \frac{\Delta\lambda}{\alpha} \tag{4.14}$$

where δ is the distance from the resonator to the neutral axis of the buckle, and α is the strain-optical coupling coefficient defined in Section 4.1.3. All of the parameters in the above equation relate to the buckle properties, with the exception of the modulus of the matrix. As expected, a lower modulus leads to a worsened resolution due to the weaker strain transfer from the matrix to the buckle. Using δ=1 µm and α=3.2 nm/%, our current design yields

$\Delta F_{buckle} = 10$ µN and $\Delta \epsilon_{matrix} = 804\text{kPa} \cdot 1/E_{matrix}$, corresponding to a sensitivity of 0.1 to 0.8% in matrices of modulus 50 to 1 kPa. These values aren't satisfactory, as state-of-the-art techniques are able to measure down to piconewtons and hundredths of percent. We note however that both these values are linearly dependent on the modulus of the buckle material. While SU-8 was used for this proof-of-concept device, softer polymers could be used instead. PDMS for example has been used as substrate and cladding for fabrication of flexible and stretchable photonic devices [82]. It boasts a Young's modulus of around 500 kPa, that is, 4 orders of magnitude lower than this of SU-8. Using PDMS, our analysis expects a force sensitivity of 1 nN corresponding to 0.001% strain in a 1 kPa matrix. Beyond its additional advantages discussed below, these values alone place our device amongst the most precise methods to quantify stresses in soft materials.

4.4 Performances comparison

Having quantified the mechanical performance of our device, we look back at the requirements for a method for 3-D stress monitoring in soft materials, the performances of currently available techniques, and are now able to benchmark our method against them. Table 4.1 summarizes this comparison. We have demonstrated in Section 2.2 the ability to fabricate a 3-D device, and more importantly to deterministically choose the position of the sensors within the plane of the buckle. Placing buckles side-by-side then enables to span the entire 3-D space. A limitation of our model of sensing stress by measuring the change in curvature of the buckles lies in that it only applies to stresses in the plane of the buckles. However, we have explained in Section 3.5 how a multiplexed measurement would allow for qualitative detection of out-of-plane stresses, and multidirectional stress measurement is theoretically possible with photonic resonators.

We showed in the previous section a strain and force resolution of 0.001% and down to 1 nN, respectively. These values are well within the range of relevant forces in cell cultures, as single cells typically exert from 100 pN to 10 nN of force. Our device's resolution also corresponds to the lengthscale of tens of cells: with the resonator spacing only limited by the size of the resonators themselves, they could be placed every 100 µm. Our device is therefore well suited for measuring the constraints due to tens or more cells, which is the

Method	Dimensionality	Force resolution	Spatial resolution	Transparency?	Sampling volume	Speed	Complexity
Requirements	3D	<100 nN	<100 µm	No	cm^3	sec	Low
Ours	3D	1 nN-10 µN	100 µm	No	cm^3	sec	Low

Table 4.1: Performances of our proposed method for mechanical sensing at the cellular or few-cells scale.

relevant amount of precision when studying large-volume cell cultures. In that respect, our device also isn't limited in the size of the sample it measures as its fabrication and the principles underlying its functioning are all scalable to greater sizes. Since light is brought to the point of detection by waveguides instead of free space, the opacity of the sample doesn't affect the measurement in any way. Finally, the speed and ease-of-use also compare favorably with other techniques. The measurement speed is this of an optical wavelength scan – which takes a few seconds at most using an OVA system like ours. After the optical results have been collected, a simple peak-finding program is sufficient to extract the position of the peaks, and the value of the strain is obtained straightforwardly by using the provided linear strain-optical calibration relationship.

Overall, while not offering record performances in any specific performance metric, our device represents the only method demonstrated thus far capable of precise monitoring of strain in a truly 3-D sample, down to the level of tens of cells, without requiring transparency of the matrix and while remaining fast and user-friendly. The ability to precisely monitor mechanical constraints in 3-D cell cultures promises to enhance the understanding of the mechanisms at work in such systems, hopefully leading to the development of new therapies for diseases involving cellular stresses.

Chapter 5

Limit to the Raman response of nanoantennas[1]

5.1 Local density of states-based bound to the Raman enhancement

5.1.1 Limits to the local density of states

Surface-enhanced Raman spectroscopy (SERS) consists in performing Raman spectroscopy on chemicals in contact with or near an optically active structure such as a rough surface or nanoparticles. It owes its success to the much higher sensitivity it provides compared to traditional Raman spectroscopy, thanks to signals up to 12 orders of magnitude stronger. While both chemical and electromagnetic effects are commonly recognized to contribute to this enhancement, the role of the nanoparticles in concentrating the incoming field and enhancing the Raman-shifted emission is much larger than this of the charge-transfer mechanisms between the molecules under test and the nanoparticles. Many efforts have therefore focused on the electromagnetic effect to further enhance the efficiency of SERS. In that case, the available tuning parameters are the material of the SERS substrate and its geometry.

The SERS substrate (called "scatterer" in all of the following) interacts with the electromagnetic field at different points in the Raman process. It first concentrates the pump

[1] Our work on this topic will be summarized in a paper entitled: "LDOS limits to the Raman response of nanoantennas".

(incoming) field near its surface. Then, after a Raman-shifted field has been emitted by the chemical under test, the scatterer interacts with this emitted field as it is radiated out to the far field where it can be collected. Our work originated when we noticed that these processes closely resemble what is described by the local density of states (LDOS). As suggested by its name, the LDOS is a spatially resolved version of the density of states: it represents the density of modes weighted by the relative energy density of each mode's electric field at a given position [152]. Yet a more intuitive way to understand this concept consists in considering the well-known Purcell, in which a dipole near a metallic surface or within a cavity sees its emission rate depend on its position [153]. This is a direct manifestation of the LDOS, which can thus also be thought of as the enhancement in the total power emitted by an electric dipole [154, 155]. Clearly, the SERS configuration looks very much alike this of the Purcell effect and LDOS must play a role in its description.

Another starting point of our work are the recently derived limits to the LDOS near lossy, absorptive bodies of arbitrary shape by Miller *et al* [156]. Using energy conservation principles, they found that the LDOS components (radiative, non-radiative, total), or equivalently the scattered, absorbed, and extracted powers by a scatterer, could all be bounded with expressions depending solely on a material's metric and the distance between the point of interest and the surface of the scatterer. To do so, this derivation assumes that the scatterer is contained within a half-plane, such that integration is performed over that volume instead of the scatterer's volume – which would give a tighter, although not shape-independent, bound. For metals at optical frequencies, the material metric takes the simple form:

$$\frac{|\chi(\omega)|^2}{\operatorname{Im}\chi(\omega)} \tag{5.1}$$

Other expressions useful for our purposes are the LDOS limits for an scatterer contained within a volume V:

$$\frac{\rho_{tot}}{\rho_0} \leq 1 + \frac{2\pi}{k^3}\frac{|\chi(\omega)|^2}{\operatorname{Im}\chi(\omega)}\int_V |G|_F^2 \tag{5.2}$$

$$\frac{\rho_{rad}}{\rho_0} \leq 1 + \frac{\pi}{2k^3}\frac{|\chi(\omega)|^2}{\operatorname{Im}\chi(\omega)}\int_V |G|_F^2 \tag{5.3}$$

where $\rho_0 = \omega^2/2\pi^2c^3$ is the free-space electric LDOS, $\mathbf{k}$ is the wavevector of the light, G is the free-space Green's function, and $|.|_F$ is the Frobenius norm. Miller then proceeded

to compare the performance of several scatterer geometries and materials to these limits in order to find optimal shapes for enhanced performances. These limits and the apparent connection between LDOS and SERS enhancement suggested the possibility of a bound to the SERS enhancement. In a thought process similar to [156], existence of such a bound would allow for benchmarking of commonly used SERS substrates in order to select the best performing ones, and would open up the possibility of optimizing scatterers towards higher efficiencies.

5.1.2 Raman bound derivation

To derive a specific bound for SERS enhancement, we consider the configuration shown on Figure 5-1. The pump field is incident onto a scatterer made out of a material with susceptibility $\bar{\bar{\chi}}(\mathbf{x}, \omega)$. Near the scatterer lies the chemical of interest (called "Raman material" in all of the following), which upon interaction with the pump field behaves as a dipole emitting another field, Raman-shifted in frequency. This Raman field further interacts with the scatterer and can be collected in the far field for measurement.

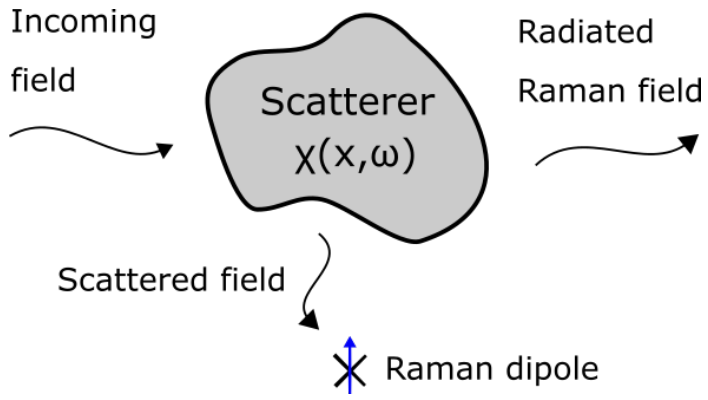

Figure 5-1: Schematic of the configuration under consideration.

To derive a bound to the overall Raman enhancement, we broken down the overall Raman process into three steps that can be treated separately:

1. We derived a bound for the value of the incident field at the Raman material's location. This value is a combination of the incident field itself and of the field that was scattered by the scatterer.
2. We calculated the magnitude of the Raman dipole excited by this incoming field.

3. We derived a limit to the power radiated to the far-field by this dipole.

The full derivation of step 1 is given in Appendix B. Using the reciprocity theorem, we show that the magnitude of the scattered component of the incident field is bounded by:

$$|\mathbf{E_{scat}}(\mathbf{x_0})|^2 \leq \left(\frac{|\chi(\omega_P)|^2}{\operatorname{Im}\chi(\omega_P)}\right)^2 \cdot V \cdot |\mathbf{E_{inc}}|^2 \cdot \int_V |G(\mathbf{x}, \mathbf{x_0})|^2 = g_{max} \tag{5.4}$$

where ω_P is the frequency of the pump light. The presence of different factors in this bound can be understood by considering that the scattered field is in essence an overlap integral between the incoming field and a dipole field. It is thus proportional to the intensity of the incident wave, the volume, and the material metric on one end, and to the integral of the Green's function (giving the dipole strength) and the material metric again on the other. The bound on the total field of the Raman material's location is thus:

$$|\mathbf{E}(\mathbf{x_0})|^2 \leq |\mathbf{E_{inc}}|^2 \left(1 + \sqrt{g_{max}}\right)^2 \tag{5.5}$$

In step 2 we used the classical treatment of spontaneous Raman emission to calculate the magnitude of the Raman dipole excited by the incoming field. The moment of the Raman dipole is related to the incident field by the Raman polarizability Îś of the material:

$$\mu = \alpha \mathbf{E}(\mathbf{x_0}) \cos(\omega_P t) = \left[\alpha_0 + \left(\frac{\delta\alpha}{\delta q}\right)_0 q_0 \cos(\Delta\omega t)\right] \mathbf{E}(\mathbf{x_0}) \cos(\omega_P t) \tag{5.6}$$

where α is expanded around the equilibrium position of the oscillator $q = q_0 \cos(\Delta\omega t)$ describing the Raman-active material. We singled out the frequency-shifted (Stokes and anti-Stokes) components of the dipole moment to calculate the average power expanded by this dipole in free space:

$$\mu(\omega_P \pm \delta\omega) = \frac{1}{2}\left(\frac{\delta\alpha}{\delta q}\right)_0 q_0 \mathbf{E}(\mathbf{x_0}) \cos\left((\omega_P \pm \Delta\omega)t\right) = \alpha_1 \mathbf{E}(\mathbf{x_0}) \cos(\omega_R t) \tag{5.7}$$

$$P_{tot} = \frac{\mu_0 \omega_R^4}{12\pi c} |\mu(\omega_R)|^2 \tag{5.8}$$

where $\omega_R = \omega_P - \Delta\omega$ is the Stokes-shifted frequency.

Step 3 corresponds exactly to the configuration described by the definition of the LDOS. We therefore used the limit to the radiative LDOS (Equation 5.3) directly to bound the

radiated power:

$$P_{rad} = P_{tot}\frac{\rho_{rad}}{\rho_0} \leq P_{tot}\left(\frac{\rho_{rad}}{\rho_0}\right)_{max} \tag{5.9}$$

Finally, all three steps were brought together to yield the overall Raman bound:

$$\frac{P_{rad}}{|\mathbf{E_{inc}}|^2} \leq \frac{\omega_R}{24\epsilon_0}\cdot\alpha_1^2\cdot\left(\frac{|\chi(\omega_P)|^2}{\operatorname{Im}\chi(\omega_P)}\right)^2\cdot\frac{|\chi(\omega_R)|^2}{\operatorname{Im}\chi(\omega_R)}\cdot V\cdot\left(\int_V |G|_F^2\right)^2 \tag{5.10}$$

Several contributions can be identified in this final bound. One comes from the material of the scatterer, through a metric consisting in this of Equation 5.1 at both the pump (twice) and Stokes-shifted frequencies. The scatterer's geometry contributes through the volume and the integral of the Green's function. Finally, the polarizability of the Raman material is the only factor that is independent of the scatterer. In order to compare different scatterers, we can thus normalize this bound by the coefficient α_1^2 to yield a metric that depends solely on the scatterer's properties.

This limit is easy to evaluate. Using tabulated susceptibility (or equivalently, optical index and absorption) values, the materials metric can be plotted to highlight its influence (Figure 5-2(a)). We see that silver exhibits the strongest response at visible frequencies (400 to 800 nm), where common pump sources lie. While for most geometries an analytical expression doesn't exist for the integral of the norm of the Green's function, it is easily calculated numerically (see Figure 5-2(b)) for any parametrizable shape, given the expression of the Frobenius norm:

$$|G|_F^2 = \frac{k^6}{8\pi^2}\left[\frac{3}{(kr)^6}+\frac{1}{(kr)^4}+\frac{1}{(kr)^2}\right] \tag{5.11}$$

5.2 Simulation of the response of typical antennas

5.2.1 *scuff-em* simulations

Having calculated the limit to the Raman enhancement of a scatterer, we wanted to compare it to the performances of antennas commonly used as SERS substrates. Several methods exist for solving electromagnetic scattering problems, where some known incident field such as a plane wave is scattered by some known geometry (objects of known shapes and materials) but the scattered fields are unknown. Expanding the field into sets of known

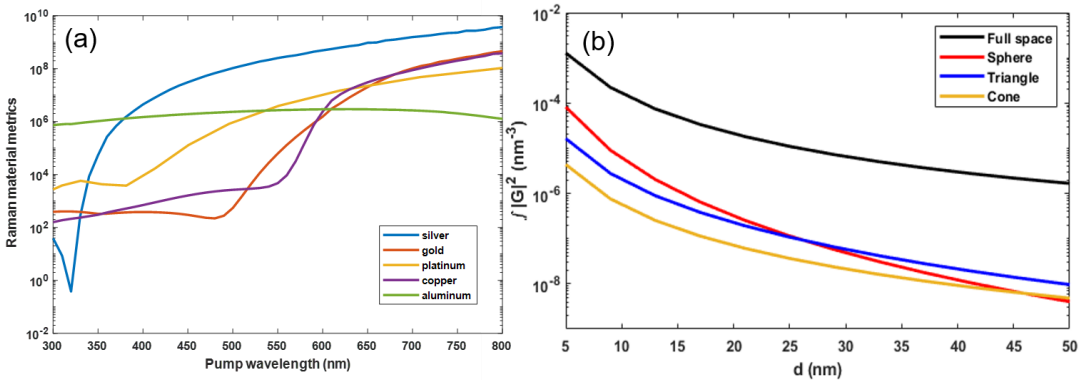

Figure 5-2: (a) Plot of the Raman material metric in the visible range for common SERS metals. The Raman shift is fixed at 400 cm^{-1}. (b) Plot of the integral of the norm of the Green's function over different sample geometries. The sphere has a radius of 30 nm, the triangle is equilateral with a side of 80 nm and a height of 30 nm, the cone has a base radius of 105 nm and a length of 40 nm.

Maxwell solutions is efficient as it exploits known solutions, yet only works for very specific geometries where such solutions are known. Inversely, the finite-difference method, consisting in discretizing the space onto a grid and solving for the value of the field at each point using finite-difference approximations, is very general yet computationally expensive as it requires the solutions to be computed over the entire space, not just the locations of interest. In the surface-integral-element method, only the scatterer's surface is discretized and currents calculated there (using the boundary-element method), in order to then calculate fields at the locations of interest using known Maxwell solutions (the Green's function). This method is both general and efficient. Notably, its speed doesn't depend on the size of the simulation space, as fields are only computed at the locations of interest. We therefore used a free, open-source software implementation of this method called scuff-em [157] to simulate the optical response of antennas.

scuff-em is a computational physics suite for analysis of electromagnetic phenomena, with modules adapted to the computation of each mechanism. We will see below that we used two of these modules: *scuff-scatter*, to perform scattering simulations, and *scuff-ldos*, to compute LDOS values. All *scuff* simulations share two common inputs: a "scuffgeo" file, giving the scatterer's geometry under the form of a mesh (see Figure 5-3) and the scatterer's material as a list of values of its susceptibility at different frequencies, and frequency file with the list of the frequencies at which to perform the simulation. The same steps as in the previous section could be used for the simulations. Step 2 however depends only

on the Raman polarizability coefficient, which is normalized to compare different scatterer materials and geometries, and therefore didn't need simulation. We thus focused on steps 1 and 3.

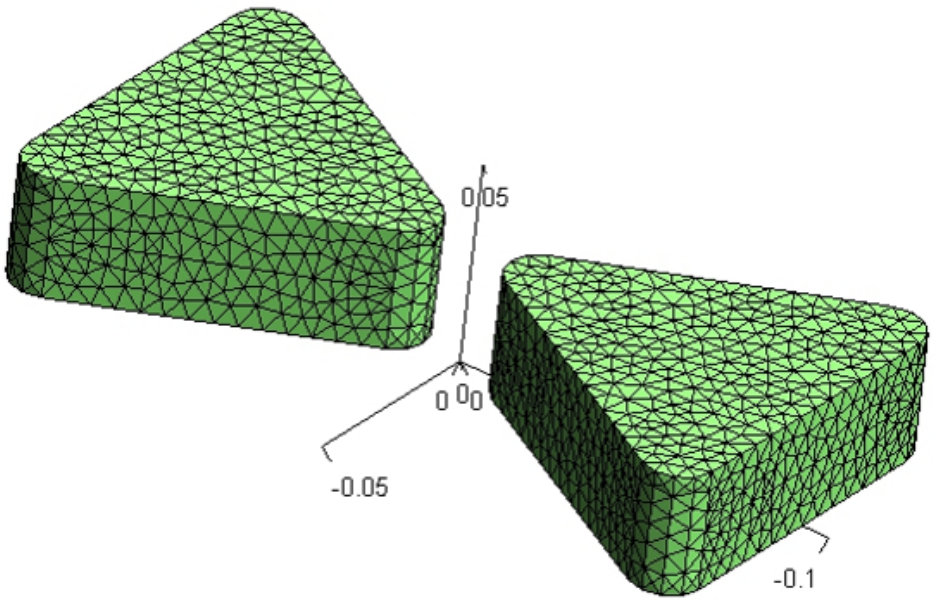

Figure 5-3: Sample mesh file describing a bowtie nanoantenna, taken as input for scuff-em simulation. The mesh size can be varied to tune the precision of the simulations.

Simulation of step 1 happened to be straightforward given the capabilities of the *scuff-scatter* module. Given an incident field (either a plane wave, a Gaussian beam, or a point source), this module outputs the power absorbed and the power scattered by the scatterer. In addition, if provided with an evaluation point, it will also provide the components of the total and scattered fields at this point – exactly the goal of step 1. A single *scuff-scatter* simulation with an incident plane wave and the location of the Raman material as evaluation point was therefore enough for this step. A sample result is shown on Figure 5-4.

Step 3 consists in calculating the power radiated into the far-field by a dipole located nearby a scatterer. Unfortunately, scuff-em doesn't output that quantity directly. Instead,

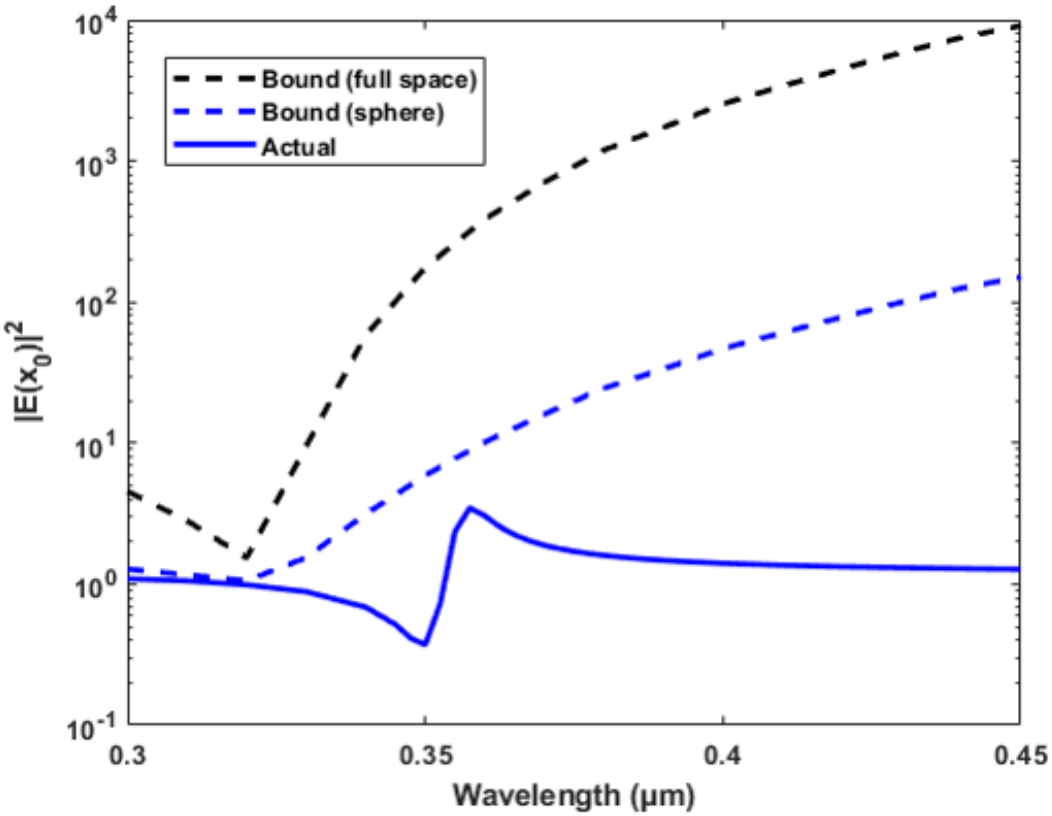

Figure 5-4: Plot of the simulated incoming field for a silver sphere of radius 20 nm. The evaluation point $\mathbf{x_0}$ is located 10 nm away from the surface of the sphere, along the direction of the polarization of the incident plane wave (point of maximal intensity). The black dashed line represents the half-space limit, the blue dashed line represents the limit calculated over the volume of the sphere.

we have:

$$P_{tot} = P_{ext} + P_{non-ext} \tag{5.12}$$

$$P_{ext} = P_{abs} + P_{scat} \tag{5.13}$$

$$\Rightarrow P_{tot} = P_{abs} + P_{scat} + P_{non-ext} = P_{abs} + P_{rad} \tag{5.14}$$

where $P_{non-ext}$ is the power not affected by the presence of the scatterer. But P_{abs} and P_{scat} can be obtained from a *scuff-scatter* simulation, and P_{tot} can be deduced from a *scuff-ldos* simulation giving the total LDOS. Our road to P_{rad} was therefore the following, with the

quantities output by simulations in bold:

$$P_{rad} = P_{tot} - P_{abs} = \left(\frac{\rho_{tot} - \rho_0}{\rho_0} + 1 \right) P_0 - P_{abs} \tag{5.15}$$

where $P_0 = \mu_0 \omega^4 / (12\pi c) |\mu|^2$ is the power expanded in free-space by a dipole of moment μ. Two simulations are thus required. One *scuff-ldos* simulation, taking as input the location of the Raman material, outputs the total LDOS value at this point. Then, a *scuff-scatter* simulation, with a point source located at the Raman material's location and expending a power P_0, outputs the power absorbed by the scatterer.

For each geometry, a set of *scuff-ldos* simulations were first run with meshes of different size (see Figure 5-5). The outputs were then compared to verify convergence, and the largest mesh showing less than 2% variation compared to the next finer mesh was selected for further simulations. The three simulations described above were run, their results were compared to the respective limits for their specific step, and finally the results were brought together to yield the full Raman performance of the scatterer. Examples of such results are presented in the following section.

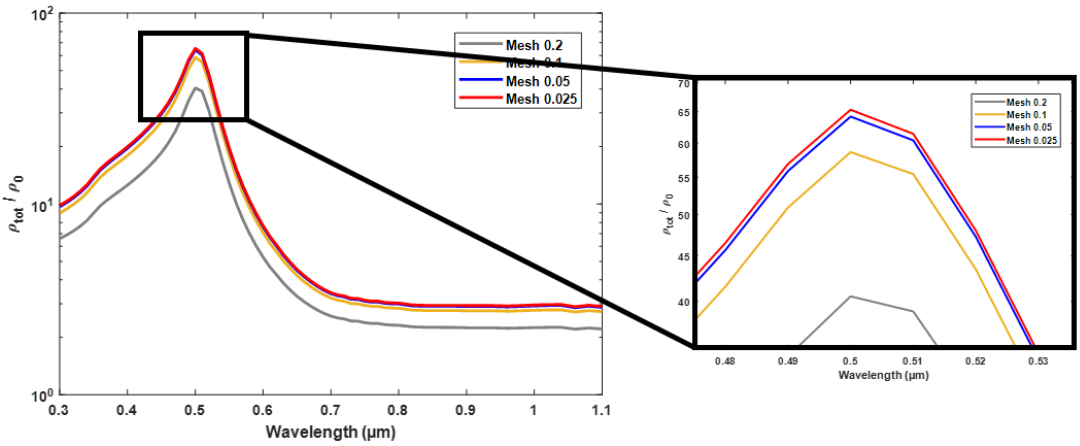

Figure 5-5: Total LDOS for different mesh sizes for a gold sphere of radius 30 nm, evaluated 10 nm away from the surface. The mesh precision is described by a number such that a smaller number corresponds to a finer mesh. In this case, the LDOS converges for a mesh of 0.05 or below.

5.2.2 Performance of typical antennas

For this study of the performance of typical nanoantennas used for SERS, we selected some of the most common shapes and materials: sphere, bowties and cones, made of gold and silver. In particular, we simulated a gold sphere of radius 30 nm with the Raman material located 10 nm away from the sphere's surface; a gold bowtie made of equilateral triangles with a 80 nm side, a 30 nm height, a 20 nm tip-to-tip spacing, and the Raman material located right in the middle [158]; and a silver bowtie made of cones with 105 nm base radius, a 40 nm tip-to-base length, a 20 nm tip-to-tip spacing, and the Raman material located right in the middle [156]. The results of these simulations are presented on Figure 5-6.

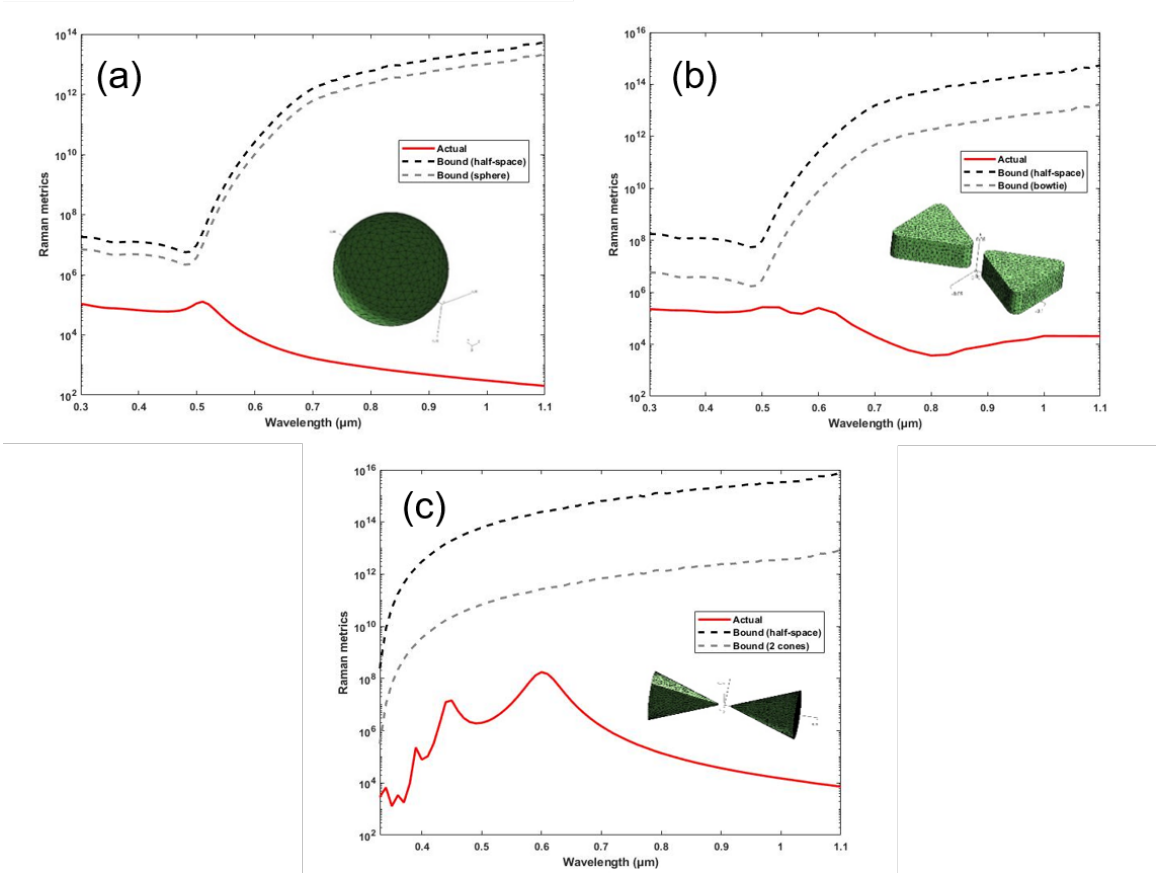

Figure 5-6: Simulated Raman performance metric for (a) the gold sphere (b) the gold triangle bowtie (c) the silver cone bowtie (see text for geometrical parameters).

We noticed that all of these structures are at least 1 to 2 orders of magnitude away from their shape-specific bound, and even further from the half-space bound. This seemingly

large difference can be understood by considering the requirements for a structure to exhibit good performances, therefore approaching the bounds. First, efficiently concentrating the incoming field means coupling strongly to both the incoming plane wave and a dipole source at the Raman material's location. Then, efficiently radiating the Raman power means again coupling strongly to the dipole source, yet this time at the Stokes-shifted frequency.

In particular, looking at the efficiency of each step separately (see Figure C-1 of Appendix C for plots of the performance of the gold sphere for each simulation) allows to realize that the largest loss comes in the first step. However, a nanosphere exposed to an incident plane wave effectively behaves as a dipole and should thus couple maximally to both that plane wave and a nearby dipole, thereby coming close to the bound for that step. We therefore looked at the analytical expression of the field at a distance d outside a sphere of radius R. An incident plane wave excites a dipole moment:

$$\mathbf{p} = \alpha V \mathbf{E_0} \tag{5.16}$$

where the polarizability α is

$$\alpha = \frac{3(\epsilon - 1)}{\epsilon + 2} = \frac{1}{1/3 + \chi^{-1}} \tag{5.17}$$

At the resonance, $\mathrm{Re}(\chi^{-1}) = -1/3$, such that:

$$\alpha_{max} = \frac{1}{\mathrm{Im}\,\chi^{-1}} = \frac{|\chi(\omega)|^2}{\mathrm{Im}\,\chi(\omega)} \tag{5.18}$$

The quasistatic field of that dipole is

$$\mathbf{E} = \frac{1}{4\pi}\left[\frac{3\mathbf{n}(\mathbf{p}\cdot\mathbf{p}) - \mathbf{p}}{(d+R)^3}\right] \tag{5.19}$$

where $\mathbf{n}$ is the unit vector along the line from the dipole to the measurement point. The amplitude of the field is maximum when $\mathbf{n}$ is parallel to $\mathbf{p}$, giving:

$$\mathbf{E} = \frac{\mathbf{p}}{2\pi(d+R)^3} \tag{5.20}$$

Replacing $\mathbf{p}$ by its value gives the expression of the concentrated field:

$$|\mathbf{E}|^2 = \frac{1}{4\pi^2}\frac{1}{(d+R)^6}\left(\frac{|\chi(\omega)|^2}{\mathrm{Im}\,\chi(\omega)}\right)^2 V^2|\mathbf{E_0}|^2 \tag{5.21}$$

This analytical expression includes all the same factors as our bound for the magnitude of the incident field (Equation 5.4), with the integral of the Green's function being $V/(d+R)^6$. This term lets us realize that for a sphere to approach the limit of Equation 5.4, it needs to have $R \ll d$, so that the distance is not effectively increased by the more distant center of mass. To verify this and make sure that the difference isn't due to numerical prefactors in the value of the bound, we plotted the analytical field value and the limit as a function of the distance to the sphere for spheres of several radius, as shown on Figure 5-7. As expected, spheres fall short of their limit when $R \geq d$ but approach it for $R \ll d$.

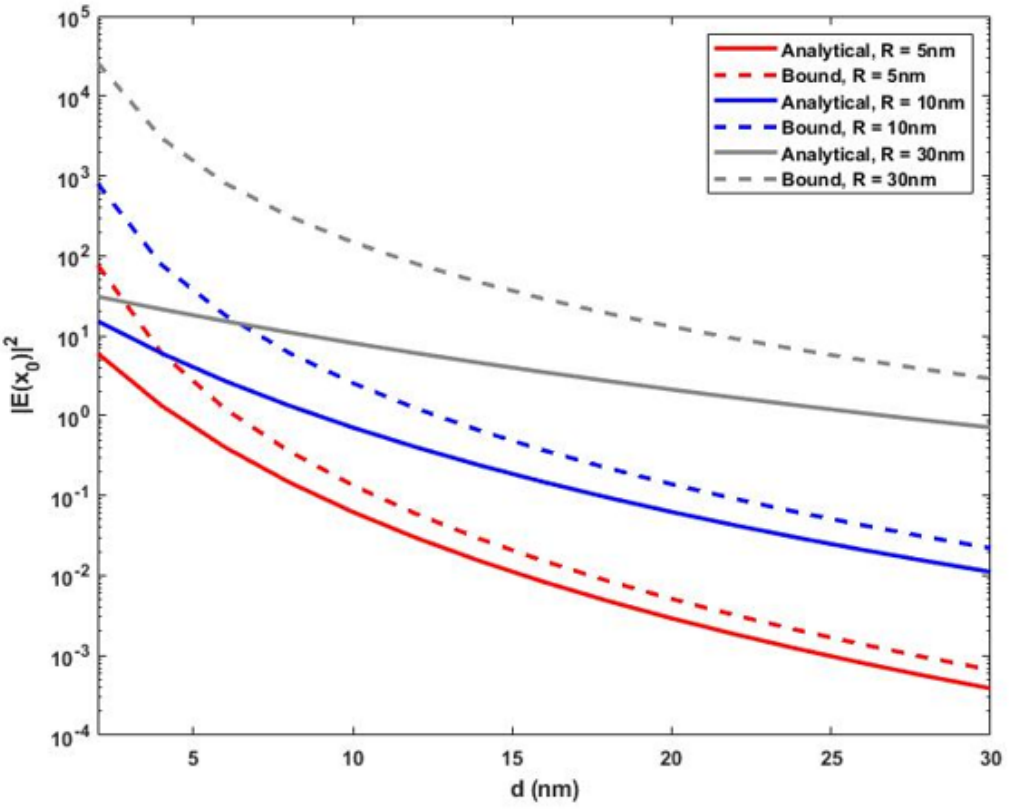

Figure 5-7: Analytical value of the concentrated field and limit to that field for silver spheres of different radius.

Another insight from the above derivation is that this match between the analytical

expression and the limit is only realized at the resonance frequency of the material. However, gold for example never satisfies $\mathrm{Re}(\chi^{-1}) = -1/3$, while silver does. Silver structures are thus more prone to reaching the bounds, while gold structures will always fall short. To verify this, we simulated another sphere, this time made of silver, with a 10 nm radius, and 20 nm away from the Raman material – which should come much closer to the bound for the first step. This is indeed the case, as can be seen on Figure 5-4. However, the overall Raman performance remains orders of magnitude away from the bound, as can be seen on Figure 5-8 which compares the performances of several silver structures located 20 nm away from the point of interest.

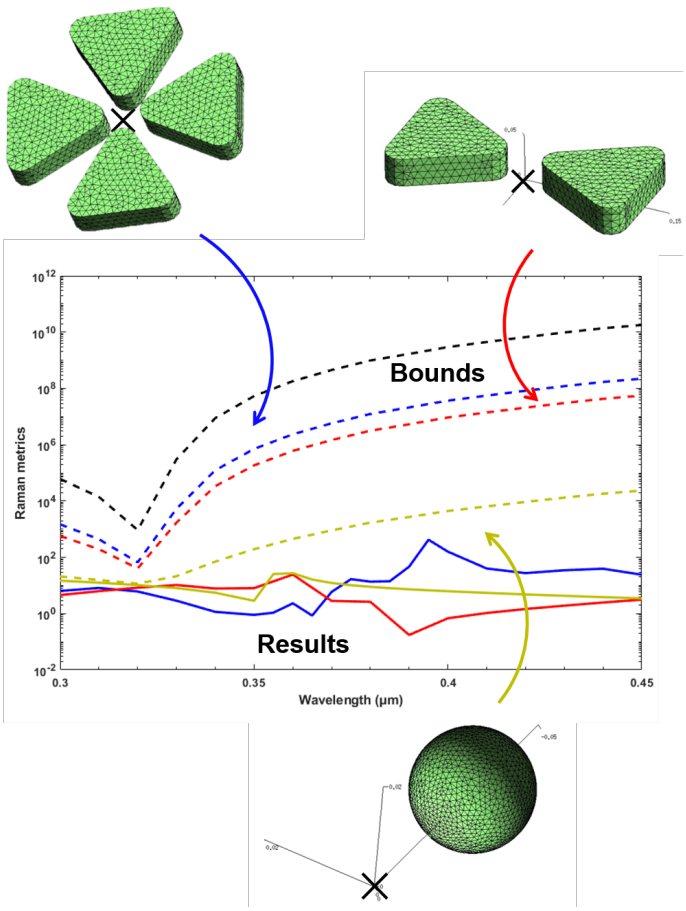

Figure 5-8: Simulated overall Raman performance for different silver structures with $d = 20$ nm. The bowties are made of equilateral triangles with a side length of 150 nm, height of 30 nm, and tip rounding radius of 16 nm.

There are several limitations to the simulations and bounds discussed here, in that

they differ from what happens in reality. First, we only evaluated the performances at a single point near the scatterer – this of maximal LDOS – while the value of all the quantities considered here do depend on the evaluation point. In practice, the Raman material's location is random, and oftentimes it actually occupies the entire space around the scatterer. Therefore, a metric calculated at a single point only gives a partial view of the actual enhancement provided by the scatterer. In addition, the structures are simulated by themselves, without any substrate, which obviously isn't the case in practice. The substrate is a scatterer itself, even if made out of a material with a much lower Raman response than the nanoantennas. Its presence would modify the overall response of the SERS substrate, in its magnitude and its geometrical distribution.

5.2.3 Performance of periodic structures

It is practically very difficult to work with single, isolated structures such as the ones simulated in the previous sections. Instead, wafer-scale microfabrication techniques favor the manufacturing of large-area repeating patterns. Moreover, just like bowties allow for additional field concentration compared to single triangles, periodic structures may offer increased SERS performances. We thus also looked at their performances, both with regards to their limits and compared with these of isolated structures. We considered the case of a square lattice (period a) of spheres of radius R, with the point of interest located at a distance d away from the surface of one of the spheres.

The periodic case can be treated similarly to the isolated case. In particular, all the previously derived bounds from Section 5.1.2 still apply if the proper Green's functions are used. In the first step, all the repeated structures combine their response to concentrate the field at the Raman material's location. The Green's function to be used is therefore the periodic Green's function. Inversely, in the third step, radiation of the Raman power, the structures radiate incoherently and thus the overall Green's function is the sum of the independent scatterers' Green's functions. However, another bound on the incident field may be derived by considering the field incident onto a single unit cell and using Bloch boundary conditions. This yields a limit (Equation B.12) with a different dependence than this used in the isolated case (Equation B.9): it scales with the surface of the unit cell a^2, instead of the volume of the scatterer V.

Given these two limits, we looked at how they compared to the limit for an isolated

sphere, as a function of the period of the lattice. The resulting graph is given on Figure 5-9. The expected dependencies on the period are observed: the area-based limit increases with the period as more power is incident on the unit cell, while the volume-based limit decreases as the volume is fixed yet the influence of other spheres diminishes. Three different zones (as a function of the period) can then be distinguished:

- On the left of point Q, the performance of the periodic structure is limited by the area-based limit which is smaller than the isolated limit.
- On the right of point P, the performance of the periodic structure is limited by the volume-based limit which converges (from above) towards the isolated limit.
- Between points Q and P, the performance of the periodic structure is limited by the increasing area-based limit which eventually crosses the decreasing volume-based limit.

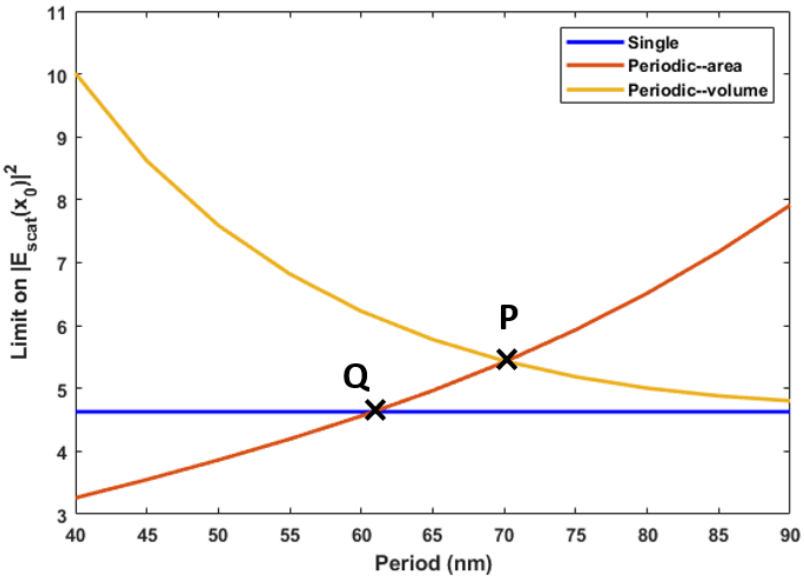

Figure 5-9: Calculated limits for a sphere with radius $R = 20$ nm and a distance to scatterer $d = 10$ nm, at 45°from the lattice axis (see Figure C-3(a)).

This graph provides insights as to the period most likely to provide performance enhancement: this of point P, where the periodic limit is furthest above the isolated limit. However, it also points at the possibility of a performance degradation caused by using a periodic structure, if the period is too small (left of point Q). To get a better idea of the design space available, the position of points P and Q is plotted on Figure 5-10 as a function of the radius of the spheres. We see that the difference between points P and Q gets smaller

as the radius increases, meaning P gets closer and closer to the isolated limit. Even at small radii, the difference in period between P and Q never exceeds 30 nm.

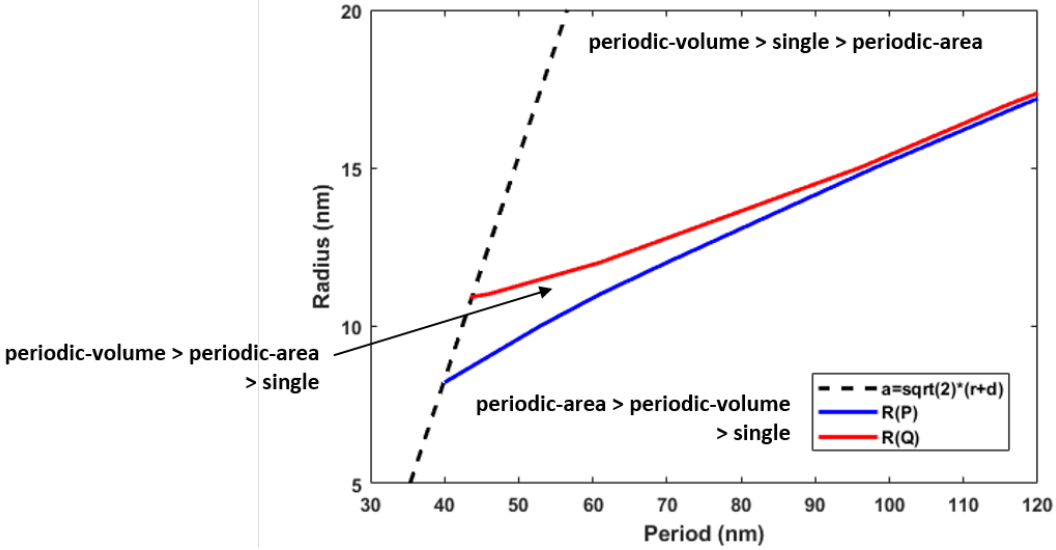

Figure 5-10: Position of points P and Q from Figure 5-9 as a function of the period and radius of the spheres, for a distance to scatterer $d = 10$ nm. The dashed corresponds to the geometrical condition where the spheres are touching.

These findings allow to make recommandations for the use of periodic structures. We found that a performance enhancement is indeed possible using periodic structures, yet that improvement is limited in magnitude (P isn't far above Q) and in the range of periods over which it can be reached. Furthermore, there exists a cutoff period under which the periodic limit is actually lower than the isolated limit. Users of periodic SERS substrates should therefore use a single structure optimized to come closer to the isolated bound, and use a long period to avoid risking to degrade the performances when going to periodic.

It should be noted here that the discussion in this Section involved the limits and not the actual simulated performances. For this discussion to translate directly to the performances, a structure getting close to the bounds would be required. However, by assuming a constant difference between the bound and the actual performance, comparing the bounds still provides insights into the relative performances.

Chapter 6

Summary and future works

6.1 Summary

This thesis aimed at advancing the field of photonic sensing by demonstrating novel devices and applications, and improving current sensors. Specifically, we looked at stress sensing in soft materials systems and at the performance of nanoantennas for surface-enhanced Raman spectroscopy.

In Chapter 2, 3, and 4, we first proposed a 3-D flexible integrated photonic device that can be used for stress sensing in soft materials. We showed that we can indeed use strain-optical coupling to quantify stress (or equivalently strain) by performing an optical measurement. We proposed and demonstrated experimentally a new way to fabricate 3-D photonic devices using buckling of strips. We are able to predict the final shape of the buckle based on parameters controlled experimentally: its thickness profile, its total length, and its span when buckled. In particular, modulating the thickness along the buckle allows us to create buckles spanning the entire plane in which the buckles lie, thereby enabling deterministic precise 3-D positioning.

We developed a fabrication process for these devices using standard, well-mastered fabrication techniques such as photolithography, e-beam lithography, and reactive ion etching, in an effort to ready flexible integrated photonics for large-scale production. A specific peel-off process had to be optimized in order to guarantee the integrity of the devices as they are removed from their substrates after 2-D fabrication: the device is undercut by etching the layer underneath it, picked up with water-soluble tape, placed onto its stage, and buckled. Once fabrication was completed, the device needed to be packaged such that it could be

shipped and used in a non-optical laboratory. We settled on using fiber arrays after trying edge coupling and single-fiber grating coupling. Fiber arrays and grating coupling met our specifications for an alignment-tolerant, robust, and scalable packaging approach. Upon measuring the devices, we characterized their performances and found an intrinsic Q-factor of ∼20,000, yielding a resonant wavelength measurement accuracy of below 1 pm. However, we also noticed that the resonant peaks were shifting over time even in the absence of mechanical deformation applied. We attributed this shift to relaxation effects in the glass and temperature variations. Temperature changes were accounted for by adding a second, temperature-tracking resonator on an area of the device not subject to stress, such that the contribution of temperature to the peak shift can be subtracted. A separate study of the stability of our set of materials found that photosaturating them and exposing them to 130°C for 2 hours sped up their relaxation to a stable state. Finally, we considered two photonic resonator designs, namely ring resonators and photonic crystal cavities. While rings were used for early demonstrations due to their simplicity, we optimized a side-coupled zero-length photonic crystal cavity design such that it produced a single peak in absorption, thereby enabling us to place several such cavities along a waveguide and monitor their responses independently. This realizes a unique advantage of photonic sensing over electronic sensing: the ability to multiplex sensing sites along a single channel.

Our device is only useful to its end-users to the extent that the optical measurement can be linked to a mechanical deformation. We therefore calibrated the strain-optical response of our sensors. We first did so by applying a known, controlled deformation to the device. We measured its optical response on the one hand, and simulated the mechanical response on the other hand. Bringing the results from both sides together yielded the strain-optical coupling relationship we were looking. We showed it to be linear with a slope of 3.2 nm/% – a value solely dependent on the resonator design and the materials used, but independent of the buckle shape and the resonator's position along the buckle. However, precision concerns due to visually determined parameters led us to come up with a calibration process that only relies on optical measurements. Having characterized the response of our sensors to mechanical stimulation, we were able to calculate its sensitivity and the range of materials to which it is applicable. We found that given our current design and materials, our devices should work in matrices with a modulus down to 300 Pa. The resolution of the measurement is found to be inversely proportional to the matrix modulus, with a force sensitivity of 10

ÂţN and a worst-case scenario 0.8% strain sensitivity in the softest biological materials. Yet the possibility to use a softer cladding polymer would allow for a much increased sensitivity, down to 1 nN and 0.001%. Overall, the ability to precisely monitor mechanical constraints in 3-D cell cultures promises to enhance the understanding of the mechanisms at work in such systems, hopefully leading to the development of new therapies for diseases involving cellular stresses.

In Chapter 5, we used a LDOS-based approach to derive a bound for the Raman enhancement provided a scatterer near the chemical considered. This bound includes contributions from the scatterer's material, the scatterer's geometry, and the chemical's Raman polarizability. We then simulated the performances of commonly used SERS structures and found them to lie far away from the bound, which is explained by the difficulty to both concentrate the incoming field and radiate the expended dipole power. We showed that nanospheres could be optimized to better concentrate the incoming field. We also considered periodic structures, which are often used in practice. We derived another expression for the field concentration bound in the periodic case, which led us to a condition for a periodic array of spheres to outperform a single sphere.

6.2 Outlooks

The projects pioneered in this thesis open up exciting avenues in their respective areas and in photonic sensing in general.

A limitation of the current design of the 3-D stress-sensing device is the inability to measure lateral stresses quantitatively. However, as explained in Section 2.2, using the different polarities of light theoretically allows for direction-resolved stress measurement. Implementing such sensors in our 3-D platform would expand its practical usability. This would require optimization at both the materials level and the resonator design level in order to sense the typically 2 to 3 orders of magnitude weaker out-of-plane stresses. Another way to get at multidirectional constraints without engineering new sensors would be to come up with a device architecture that would combine buckles along different directions, for example perpendicular to one another, such that each buckle would quantify constraints in its own direction. Equivalently, designing buckles that are not constrained to a single plane could

provide the same multidirectional information and give access to many more geometries [81].

Other materials could also be used for the fabrication of this device. On the cladding side, using a softer polymer than SU-8 would decrease the stiffness of the buckles and therefore make the device more sensitive. We have notably found that the minimum modulus of the matrix and the resolution of the measurement depend linearly on the modulus of the buckles. In addition, using a stretchable polymer would allow for a more direct detection of stresses in the matrix of interest: instead of detecting the effect of the matrix deformation on the buckle curvature, which is an averaged effect, the local contraction or expansion of the matrix would be directly transferred to the buckle and detected. PDMS for example is a stretchable polymer that has been used as substrate and cladding for fabrication of flexible and stretchable photonic devices [82], although its large CTE mismatch with typical optical materials would require careful processing to avoid cracking. Alternative optical materials include other chalcogenide glasses with higher index or that allow for solution-based processing [113, 159]. Titanium dioxide (TiO_2) could also be of interest. Besides meeting all the requirements for our platform (high index n = 2.4, monolithic processing at reduced temperatures, broad transparency window from 400 nm to 5.5 µm, biocompatibility [111]), it exhibits a low fluorescence background in the visible range that enables Raman spectroscopy [160].

Spectroscopy and more broadly speaking multifunctional sensing beyond stress and strain, are indeed perhaps the most exciting prospects of this platform. Optical resonators have been used to perform many other types of sensing such as label-free protein sensing [161, 162], small molecule spectroscopy [163], ultrasound detection [164], or pH and humidity monitoring [165]. Combining our 3-D fabrication process with these various sensing capabilities would enable a host of applications in the 3-D space we all live in. Notably, it would be most beneficial applications where monitoring complex physical/chemical parameter distributions and fluxes is mandatory, for instance directional electromagnetic wave sensors, flow monitoring in microfluidics, non-destructive structural health monitoring (SHM) in soft materials, as well as synthetic process control in tissue engineering and additive manufacturing. In biological materials, it could be used to selectively deliver and collect light at/from precise 3-D locations to enable different in-situ light-based diagnosis [176]. Overall, the proposed architecture is therefore amenable to becoming a multifunctional 3-D sensing and light delivery platform. Better sensing and light delivery capabilities promise to greatly

expand the available toolbox for biologists and soft matter researchers.

Our work on applying LDOS bounds to Raman enhancement was the first of its kind and therefore opens up many research directions. The limitations of our preliminary study could be addressed in future works. In practical uses of SERS, molecules are found all around the scatterer, not just at a single point. A location-averaged evaluation of the different scatterer geometries would therefore provide a better comparison metrics. Coming up with bandwidth-averaged bounds and benchmarking designs against these bounds would also be of interest [166,167]. Yet probably the most impactful work would be to look systematically for optimal structures, whose performance would more closely approach the bounds (for whichever metric is being considered – single-frequency and single-point, location-averaged, bandwidth-averaged, etc.), for example using the adjoint method to more effectively explore the very large available parameter space [168]. Given the vast application scope of SERS, improvements in these areas promise to positively influence research in many fields of research.

THIS PAGE INTENTIONALLY LEFT BLANK

Appendix A

Force sensitivity of buckled sensor

Having calibrated the strain-optical relationship of the resonators in Sections 4.1 and 4.2, the strains at the resonator's location and in the matrix are linked by considering the force needed to deform the buckle around the sensor. As SU-8, the polymer used to make up the structure of our device, isn't stretchable, the strain at the resonator's location is due to bending effects, that is, the local change in bending radius. To access this quantity and model its evolution, we model the region of the buckle close to the resonator by an arc of radius R and total length L. This configuration and the other geometrical notations are shown on the schematic of Figure A-1.

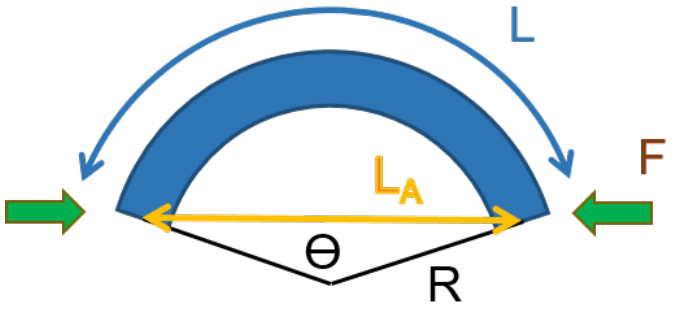

Figure A-1: Schematic side-view of a buckle segment with bending radius R and total length L. The buckle has a width w, a thickness $t = 2d$, and a Young's modulus E_{buckle}.

The strain in the buckle is a function of the distance δ to the neutral axis:

$$\epsilon(\delta) = \frac{\delta}{R} = \delta\kappa \tag{A.1}$$

with $\kappa = 1/R$ the curvature. The total strain energy is found by integrating the strain energy density, $E\epsilon^2/2$, over the whole segment:

$$W_s = \int_{-d}^{d} \frac{1}{2} E_{buckle} \left(\frac{x}{R}\right)^2 = \frac{E_b L w d^3}{3R^2} \tag{A.2}$$

$$= \frac{E_b L w t^3}{24R^2} \tag{A.3}$$

where we relabeled E_{buckle} to E_b for brevity. The chord length is given by:

$$L_A = 2R \sin\left(\frac{\theta}{2}\right) = 2R \sin\left(\frac{L}{2R}\right) \tag{A.4}$$

$$\frac{L_A}{R} = -\frac{L}{R} \cos\left(\frac{L}{2R}\right) + 2 \sin\left(\frac{L}{2R}\right) \tag{A.5}$$

The force that was needed to bend the buckle to its current radius is thus:

$$F = \frac{dW_s}{dL_A} = \frac{dW_s}{dR} \cdot \frac{dR}{dL_A} \tag{A.6}$$

$$= \frac{-E_b L w t^3}{12R^3} \cdot \frac{1}{-\frac{L}{R} \cos\left(\frac{L}{2R}\right) + 2 \sin\left(\frac{L}{2R}\right)} \tag{A.7}$$

For our sensor to read accurately the strain in the matrix, it must follow its deformation. If the matrix contracts or expands by $\epsilon_{matrix} = \Delta L_A / L_A$, the buckle must do the same, which would require an additional force:

$$\Delta F_{buckle} = \frac{dF}{dL_A} \cdot \Delta L_A = \frac{dF}{dR} \cdot \frac{dR}{dL_A} \cdot L_A \epsilon_{matrix} \tag{A.8}$$

It is useful at this point to look at the actual values of our parameters. As stated in Section 3.5.2, multiplexed resonators could be placed all along the waveguide with a spacing only limited by the size of the resonators themselves. Given that our strips measure 1 cm, a spacing of 1 mm is reasonable. The bending radius is around 1 mm according to the calculations of Section 2.2. In this case, we have $L_A = 0.96\text{mm} \approx L$ and $dL_A/dR \approx$

$-L^3/12R^3$. We can thus simplify the expressions of the forces:

$$F \approx \frac{E_b w t^3}{L^2} \tag{A.9}$$

$$\frac{dF}{dR} \approx \frac{-E_b w t^3}{10R^3} \tag{A.10}$$

$$\Rightarrow \Delta F_{buckle} \approx -\frac{6E_b w t^3}{5L^2} \cdot \epsilon_{matrix} \tag{A.11}$$

On the other hand, the force actually exerted by the matrix on the buckle is:

$$\Delta F_{matrix} = A \cdot E_{matrix} \cdot \epsilon_{matrix} \tag{A.12}$$

where $A = w \cdot R\,[1 - \cos(L/2R)] \approx wL^2/8R$ is the cross-section of the matrix interacting with the buckle. The condition for the buckle to indeed follow the matrix's deformation is thus:

$$\Delta F_{matrix} \geq |\Delta F_{buckle}| \tag{A.13}$$

$$\Rightarrow E_{matrix} \geq \frac{48}{5}\frac{Rt^3}{L^4} E_{buckle} \tag{A.14}$$

For a structure made out of SU-8 with a modulus of 4.02 GPa, this gives a minimum modulus for the matrix of 300 Pa.

We can also use Equation A.7 to estimate the sensitivity of the sensor, that is, the smallest change in strain that can be detected. For a wavelength measurement accuracy $\Delta\lambda$ and a strain-optical coupling coefficient α, we have for the smallest resolvable change in strain at the resonator's position and the corresponding change in curvature:

$$\Delta\epsilon_{res} = \frac{\Delta\lambda}{\alpha} \tag{A.15}$$

$$\Delta\kappa = \frac{\Delta\epsilon_{res}}{\delta} \tag{A.16}$$

$$\tag{A.17}$$

This corresponds to an additional force applied to the buckle:

$$\Delta F_{buckle} = \frac{dF}{d\kappa} \cdot \Delta\kappa = \frac{dF}{d\kappa} \cdot (-R)^2 \cdot \Delta\kappa \tag{A.18}$$

$$= \frac{E_b w t^3}{10R^3} \cdot \frac{\Delta\lambda}{\alpha} \tag{A.19}$$

And finally to an increase in strain in the matrix:

$$\Delta\epsilon_{matrix} = \frac{\Delta F_{buckle}}{A \cdot E_m} \tag{A.20}$$

$$= \frac{4}{5}\frac{t^3}{\delta L^2} \cdot \frac{E_{buckle}}{E_{matrix}} \cdot \frac{\Delta\lambda}{\alpha} \tag{A.21}$$

As expected, the softer the matrix the weaker the stress transfer from the matrix to the buckle, and therefore the larger the resolution. Given our wavelength measurement accuracy $\Delta\lambda = 1$ pm (see Section 3.4.2) and strain-optical coupling coefficient of $\alpha = 3.2$ nm/%, the equation, we finally have:

$$\Delta\epsilon_{matrix} = \frac{804\,\text{kPa}}{E_{matrix}} \tag{A.22}$$

For usual biological materials that have a modulus of 1 to 50 kPa, this corresponds to a minimum detectable strain of 0.1 to 0.8%.

Appendix B

Derivation of bounds on the incoming field

The aim is to derive a bound for the value of the incident field at the Raman material's location. We thus consider an incident plane wave $\mathbf{E_{inc}}$, creating a field $\mathbf{E_{scat}}$ after interaction in the scatterer, and want to evaluate the total field at the location $\mathbf{E_{inc}}$: $|\mathbf{E_{inc}}(\mathbf{x_0}) + \mathbf{E_{scat}}(\mathbf{x_0})|^2$. We can do this by maximizing either the total or the scattering amplitude, with both results being similar in the limit of large scattering. From reciprocity, we can write:

$$\mathbf{x} \cdot \mathbf{E_{scat}}(\mathbf{x_0}) = \int_V \mathbf{E_{inc}} \cdot \chi \mathbf{E_x} \tag{B.1}$$

where $\mathbf{E_x}$ is the field created by a dipole placed at $\mathbf{x_0}$ oriented along $\mathbf{x}$. $\mathbf{E_x}$ must verify:

$$\mathrm{Im}\left(\int_V \mathbf{E_x}^* \cdot \chi \mathbf{E_x}\right) - \mathrm{Im}\left(\int_V |G(\mathbf{x}, \mathbf{x_0})\mathbf{x}|^* \cdot \chi \mathbf{E_x}\right) \leq 0 \tag{B.2}$$

We want to maximize $g = |\mathbf{x} \cdot \mathbf{E_{scat}}(\mathbf{x_0})|^2$ under that constraint, which corresponds to maximizing $\langle \mathbf{P}, \mathbf{AP} \rangle$ under $\langle \mathbf{P}, \mathbf{P} \rangle \leq \alpha \mathrm{Re}(\langle \mathbf{b}, \mathbf{P} \rangle)$ where $\mathbf{P} = \chi \mathbf{E_x}$, $\alpha = |\chi|^2 / \mathrm{Im}\,\chi$, $\mathbf{A} = |\mathbf{a}^*\rangle\langle\mathbf{a}^*|$, $\mathbf{a} = \mathbf{E_{inc}}^*$, $\mathbf{b} = iG(\mathbf{x}, \mathbf{x_0})\mathbf{x}$, and $\langle \mathbf{F}, \mathbf{G} \rangle = \int_V \mathbf{F}^* \cdot \mathbf{G}$. Optimal values verify:

$$\mathbf{AP} + \lambda \left(\mathbf{P} - \frac{\alpha}{2}\mathbf{b}\right) = 0 \tag{B.3}$$

$$\Rightarrow \mathbf{P} = \frac{\alpha}{2}\mathbf{b} - \frac{1}{\lambda}\langle \mathbf{a}, \mathbf{P} \rangle \mathbf{a} = \frac{\alpha}{2}\mathbf{b} + \frac{\beta}{2}\mathbf{a} \tag{B.4}$$

$$\langle \mathbf{P}, \mathbf{P} \rangle - \alpha \mathrm{Re}(\langle \mathbf{b}, \mathbf{P} \rangle) = 0 \tag{B.5}$$

After simplification,

$$|\beta||\mathbf{a}| = |\alpha||\mathbf{b}| \tag{B.6}$$

$$\beta = \pm\alpha\frac{|\mathbf{b}|\langle\mathbf{a},\mathbf{b}\rangle}{|\mathbf{a}||\langle\mathbf{a},\mathbf{b}\rangle|} \Rightarrow \qquad g_{max} = \frac{\alpha^2}{4}\left(|\langle\mathbf{a},\mathbf{b}\rangle| + |\mathbf{a}||\mathbf{b}|\right)^2 \tag{B.7}$$

Plugging in the physical quantities yields the desired bound:

$$|\mathbf{x}\cdot\mathbf{E_{scat}}(\mathbf{x_0})|^2 \leq \frac{1}{4}\left(\frac{|\chi(\omega)|^2}{\operatorname{Im}\chi(\omega)}\right)^2\left[\left|\int_V \mathbf{E_{inc}}\cdot G(\mathbf{x},\mathbf{x_0})\right| + \sqrt{\int_V |\mathbf{E_{inc}}|^2\cdot\int_V |G(\mathbf{x},\mathbf{x_0})|^2}\right] \tag{B.8}$$

$$\leq \left(\frac{|\chi(\omega)|^2}{\operatorname{Im}\chi(\omega)}\right)^2\cdot V\cdot|\mathbf{E_{inc}}|^2\cdot\int_V |G(\mathbf{x},\mathbf{x_0})|^2 = g_{max} \tag{B.9}$$

The bound on the total field of the Raman material's location is thus:

$$|\mathbf{E}(\mathbf{x_0})|^2 \leq |\mathbf{E_{inc}}|^2\left(1+\sqrt{g_{max}}\right)^2 \tag{B.10}$$

We note that this expression also applies to periodic structures, with V the volume of the "unit" scatterer (contained within the unit cell) and G the periodic Green's function. However, a different expression may be derived in the periodic case by considering the field incident onto a unit cell, taken here to be square with period a:

$$|\mathbf{E_{scat}}(\mathbf{x_0})|^2 \leq \frac{2}{\pi}\frac{a^2k^2\cos(\theta)}{\epsilon_r}\left(1+\frac{\pi}{2k^3}\frac{|\chi(\omega)|^2}{\operatorname{Im}\chi(\omega)}\int_V |G|^2\right)|\mathbf{E_{inc}}|^2 \tag{B.11}$$

$$\approx \frac{a^2\cos(\theta)}{k\epsilon_r}\frac{|\chi(\omega)|^2}{\operatorname{Im}\chi(\omega)}\int_V |G|^2|\mathbf{E_{inc}}|^2 \tag{B.12}$$

where θ is the angle of the incident field with respect to the normal to the unit cell, and G is the periodic Green's function again.

Appendix C

scuff-em results

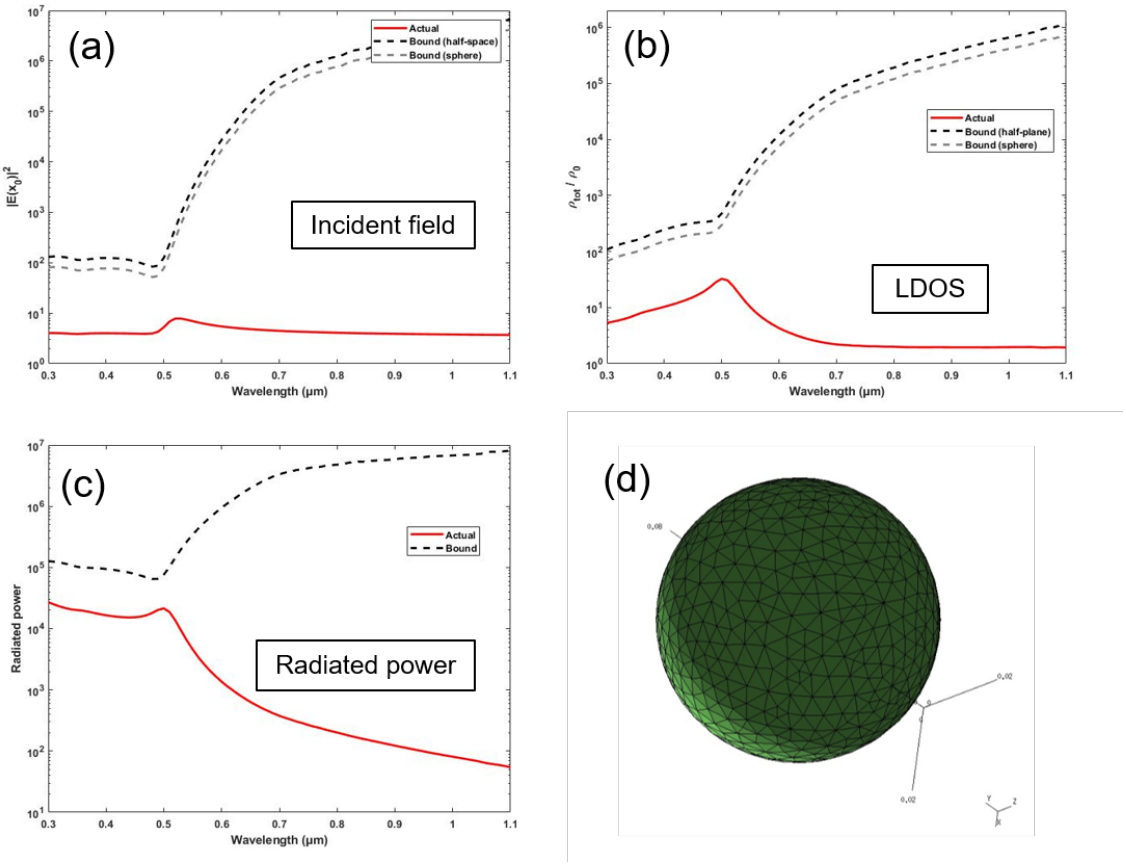

Figure C-1: Performances of a gold sphere of radius 30 nm, with a Raman material 10 nm away from its surface. (a) Concentrated incident field intensity (b) Total LDOS (c) Radiated dipole power (d) Mesh.

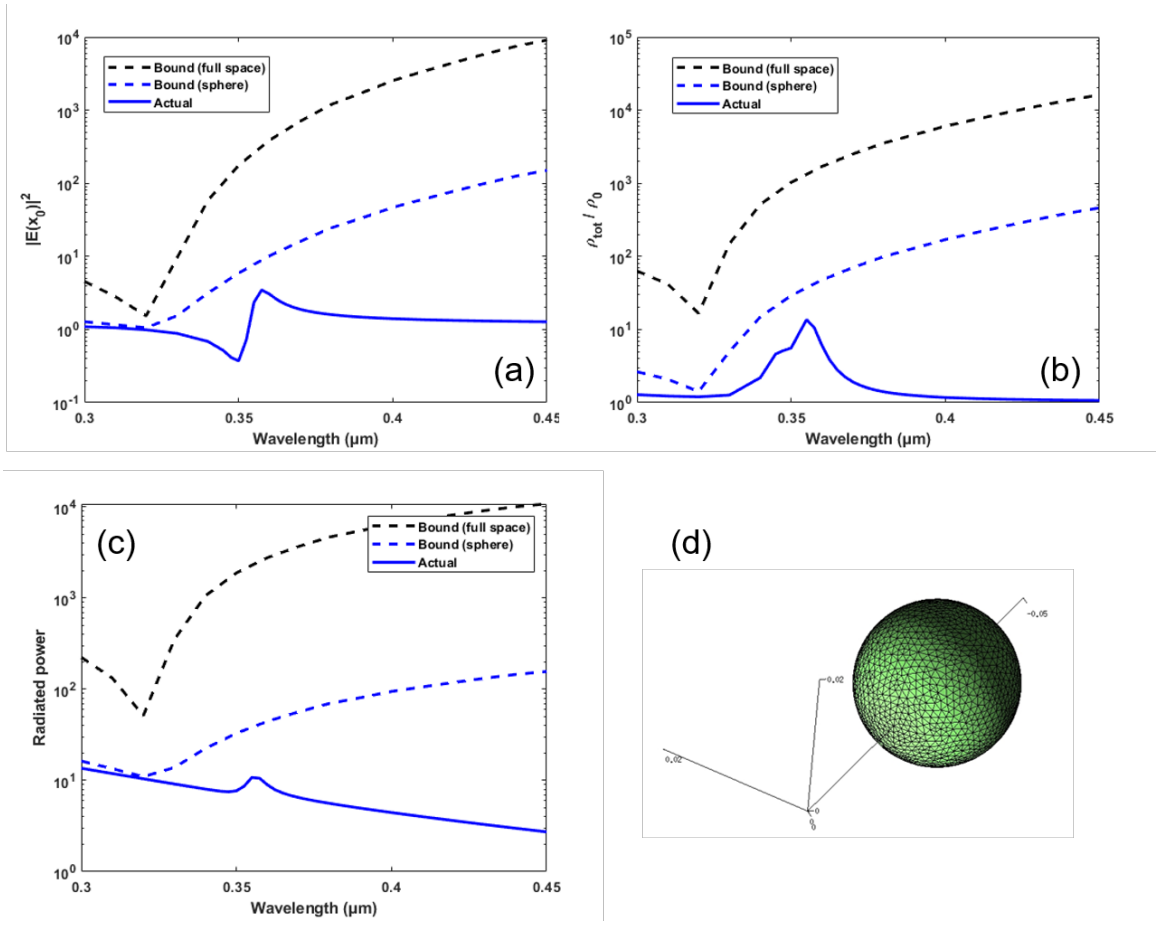

Figure C-2: Performances of a silver sphere of radius 10 nm, with a Raman material 20 nm away from its surface. (a) Concentrated incident field intensity (b) Total LDOS (c) Radiated dipole power (d) Mesh.

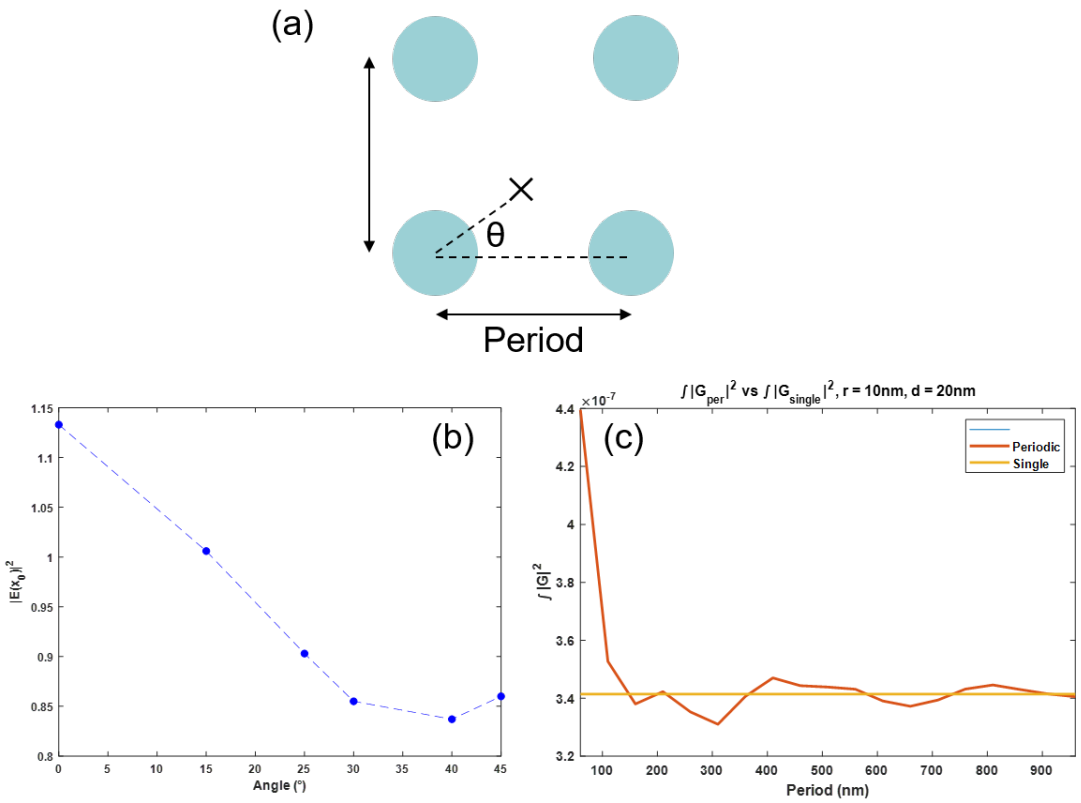

Figure C-3: (a) Schematics of the configuration simulated for periodic structures. (b) Influence of the angular position of the sphere with respect to the lattice axis. (c) Influence of the period. As expected, in the limit of long periods, the periodic results converge towards the isolated results.

THIS PAGE INTENTIONALLY LEFT BLANK

Bibliography

[1] "File:Raman energy levels.svg – Wikimedia Commons, https://commons.wikimedia.org/wiki/File:Raman_energy_levels.svg," .

[2] L. Li, H. Lin, S. Qiao, Y. Zou, S. Danto, K. Richardson, J. D. Musgraves, N. Lu, and J. Hu, "Integrated flexible chalcogenide glass photonic devices," Nature Photonics **8**, 643–649 (2014).

[3] H. Lin, L. Li, Y. Zou, O. Ogbuu, S. Danto, J. D. Musgraves, K. Richardson, and J. Hu, "Chalcogenide glass planar photonics: from mid-IR sensing to 3-D flexible substrate integration," in "Laser Resonators, Microresonators, and Beam Control XV," , vol. 8600, A. V. Kudryashov, A. H. Paxton, V. S. Ilchenko, L. Aschke, and K. Washio, eds. (International Society for Optics and Photonics, 2013), vol. 8600, p. 86000K.

[4] S. Geiger, Q. Du, B. Huang, M. Y. Shalaginov, J. Michon, H. Lin, T. Gu, A. Yadav, K. A. Richardson, X. Jia, and J. Hu, "Understanding aging in chalcogenide glass thin films using precision resonant cavity refractometry," Optical Materials Express **9**, 2252 (2019).

[5] "Distributed Bragg Reflectors – picwriter 0.0.1 documentation, https://picwriter.readthedocs.io/en/latest/components/dbr.html," .

[6] D.-H. Kim, N. Lu, R. Ghaffari, Y.-S. Kim, S. P. Lee, L. Xu, J. Wu, R.-H. Kim, J. Song, Z. Liu, J. Viventi, B. de Graff, B. Elolampi, M. Mansour, M. J. Slepian, S. Hwang, J. D. Moss, S.-M. Won, Y. Huang, B. Litt, and J. A. Rogers, "Materials for multifunctional balloon catheters with capabilities in cardiac electrophysiological mapping and ablation therapy," Nature Materials **10**, 316–323 (2011).

[7] S. Aikio, J. Hiltunen, J. Hiitola-Keinänen, M. Hiltunen, V. Kontturi, S. Siitonen, J. Puustinen, and P. Karioja, "Disposable photonic integrated circuits for evanescent wave sensors by ultra-high volume roll-to-roll method," Optics Express **24**, 2527 (2016).

[8] A. V. Shneidman, K. P. Becker, M. A. Lukas, N. Torgerson, C. Wang, O. Reshef, M. J. Burek, K. Paul, J. McLellan, and M. Lončar, "All-Polymer Integrated Optical Resonators by Roll-to-Roll Nanoimprint Lithography," ACS Photonics **5**, 1839–1845 (2018).

[9] S. H. Ahn and L. J. Guo, "High-Speed Roll-to-Roll Nanoimprint Lithography on Flexible Plastic Substrates," Advanced Materials **20**, 2044–2049 (2008).

[10] J. G. Ok, H. Seok Youn, M. Kyu Kwak, K.-T. Lee, Y. Jae Shin, L. Jay Guo, A. Greenwald, and Y. Liu, "Continuous and scalable fabrication of flexible metamaterial films

via roll-to-roll nanoimprint process for broadband plasmonic infrared filters," Applied Physics Letters **101**, 223102 (2012).

[11] R. K. Kramer, C. Majidi, and R. J. Wood, "Wearable tactile keypad with stretchable artificial skin," in "2011 IEEE International Conference on Robotics and Automation," (IEEE, 2011), pp. 1103–1107.

[12] J. A. Rogers, T. Someya, and Y. Huang, "Materials and mechanics for stretchable electronics." Science (New York, N.Y.) **327**, 1603–7 (2010).

[13] S. Xu, Z. Yan, K.-I. Jang, W. Huang, H. Fu, J. Kim, Z. Wei, M. Flavin, J. McCracken, R. Wang, A. Badea, Y. Liu, D. Xiao, G. Zhou, J. Lee, H. U. Chung, H. Cheng, W. Ren, A. Banks, X. Li, U. Paik, R. G. Nuzzo, Y. Huang, Y. Zhang, and J. A. Rogers, "Assembly of micro/nanomaterials into complex, three-dimensional architectures by compressive buckling," Science **347**, 154–159 (2015).

[14] D.-H. Kim and J. A. Rogers, "Stretchable Electronics: Materials Strategies and Devices," Advanced Materials **20**, 4887–4892 (2008).

[15] R. Verplancke, F. Bossuyt, D. Cuypers, and J. Vanfleteren, "Thin-film stretchable electronics technology based on meandering interconnections: fabrication and mechanical performance," Journal of Micromechanics and Microengineering **22**, 015002 (2012).

[16] D.-Y. Khang, H. Jiang, Y. Huang, and J. A. Rogers, "A stretchable form of single-crystal silicon for high-performance electronics on rubber substrates." Science (New York, N.Y.) **311**, 208–12 (2006).

[17] H.-C. Yuan, Z. Ma, M. M. Roberts, D. E. Savage, and M. G. Lagally, "High-speed strained-single-crystal-silicon thin-film transistors on flexible polymers," Journal of Applied Physics **100**, 013708 (2006).

[18] H. Huang, "Flexible wireless antenna sensor: A review," (2013).

[19] H. Dembo, Y. Kurokawa, T. Ikeda, S. Iwata, K. Ohshima, J. Ishii, T. Tsurume, E. Sugiyama, D. Yamada, A. Isobe, S. Saito, K. Dairiki, N. Kusumoto, Y. Shionoiri, T. Atsumi, M. Fujita, H. Kobayashi, H. Takashina, Y. Yamashita, and S. Yamazaki, "RFCPUs on glass and plastic substrates fabricated by TFT transfer technology," in "IEEE InternationalElectron Devices Meeting, 2005. IEDM Technical Digest.", (IEEE, 2006), pp. 125–127.

[20] N. Li, Z. Chen, W. Ren, F. Li, and H.-M. Cheng, "Flexible graphene-based lithium ion batteries with ultrafast charge and discharge rates," Proceedings of the National Academy of Sciences **109**, 17360–17365 (2012).

[21] Z. Chen, J. W. To, C. Wang, Z. Lu, N. Liu, A. Chortos, L. Pan, F. Wei, Y. Cui, and Z. Bao, "A three-dimensionally interconnected carbon nanotube-conducting polymer hydrogel network for high-performance flexible battery electrodes," Advanced Energy Materials **4**, 1400207 (2014).

[22] M. A. Meitl, Z.-T. Zhu, V. Kumar, K. J. Lee, X. Feng, Y. Y. Huang, I. Adesida, R. G. Nuzzo, and J. A. Rogers, "Transfer printing by kinetic control of adhesion to an elastomeric stamp," Nature Materials **5**, 33–38 (2005).

[23] S.-I. Park, Y. Xiong, R.-H. Kim, P. Elvikis, M. Meitl, D.-H. Kim, J. Wu, J. Yoon, C.-J. Yu, Z. Liu, Y. Huang, K.-c. Hwang, P. Ferreira, X. Li, K. Choquette, and J. A. Rogers, "Printed assemblies of inorganic light-emitting diodes for deformable and semitransparent displays." Science (New York, N.Y.) **325**, 977–81 (2009).

[24] G. Gustafsson, Y. Cao, G. M. Treacy, F. Klavetter, N. Colaneri, and A. J. Heeger, "Flexible light-emitting diodes made from soluble conducting polymers," Nature **357**, 477–479 (1992).

[25] G. Zhang, C. Lan, H. Bian, R. Gao, and J. Zhou, "Flexible, all-dielectric metasurface fabricated via nanosphere lithography and its applications in sensing," Optics Express **25**, 22038 (2017).

[26] X. Xu, B. Peng, D. Li, J. Zhang, L. M. Wong, Q. Zhang, S. Wang, and Q. Xiong, "Flexible visible-infrared metamaterials and their applications in highly sensitive chemical and biological sensing," Nano Letters **11**, 3232–3238 (2011).

[27] J. Valentine, J. Li, T. Zentgraf, G. Bartal, and X. Zhang, "An optical cloak made of dielectrics," Nature Materials **8**, 568–571 (2009).

[28] X. Ni, Z. J. Wong, M. Mrejen, Y. Wang, and X. Zhang, "An ultrathin invisibility skin cloak for visible light," Science **349**, 1310–1314 (2015).

[29] L. Zhang, J. Ding, H. Zheng, S. An, H. Lin, B. Zheng, Q. Du, G. Yin, J. Michon, Y. Zhang, Z. Fang, M. Y. Shalaginov, L. Deng, T. Gu, H. Zhang, and J. Hu, "Ultra-thin high-efficiency mid-infrared transmissive Huygens meta-optics," Nature Communications **9**, 1481 (2018).

[30] S. M. Kamali, A. Arbabi, E. Arbabi, Y. Horie, and A. Faraon, "Decoupling optical function and geometrical form using conformal flexible dielectric metasurfaces," Nature Communications **7**, 11618 (2016).

[31] R. R. Shannon, "Overview of conformal optics," in "Window and Dome Technologies and Materials VI," , vol. 3705, R. W. Tustison, ed. (International Society for Optics and Photonics, 2003), vol. 3705, pp. 180–188.

[32] L. Li, Y. Zou, H. Lin, J. Hu, X. Sun, N. N. Feng, S. Danto, K. Richardson, T. Gu, and M. Haney, "A fully-integrated flexible photonic platform for chip-to-chip optical interconnects," Journal of Lightwave Technology **31**, 4080–4086 (2013).

[33] R. Dangel, F. Horst, D. Jubin, N. Meier, J. Weiss, B. J. Offrein, B. W. Swatowski, C. M. Amb, D. J. Deshazer, and W. K. Weidner, "Development of versatile polymer waveguide flex technology for use in optical interconnects," Journal of Lightwave Technology **31**, 3915–3926 (2013).

[34] R. Dangel, A. La Porta, D. Jubin, F. Horst, N. Meier, M. Seifried, and B. J. Offrein, "Polymer waveguides enabling scalable low-loss adiabatic optical coupling for silicon photonics," IEEE Journal of Selected Topics in Quantum Electronics **24** (2018).

[35] C. Choi, L. Lin, Y. Liu, J. Choi, L. Wang, D. Haas, J. Magera, and R. T. Chen, "Flexible optical waveguide film fabrications and optoelectronic devices integration for fully embedded board-level optical interconnects," Journal of Lightwave Technology **22**, 2168–2176 (2004).

[36] E. Bosnian, G. Van Steenberge, B. Van Hoe, J. Missinne, J. Vanfleteren, and P. Van Daele, "Highly reliable flexible active optical links," IEEE Photonics Technology Letters **22**, 287–289 (2010).

[37] D. Jubin, R. Dangel, N. Meier, F. Horst, T. Lamprecht, J. Weiss, R. Beyeler, B. J. Offrein, M. Halter, R. Stieger, and F. Betschon, "Polymer waveguide-based multilayer optical connector," in "Optoelectronic Interconnects and Component Integration IX," , vol. 7607, A. L. Glebov and R. T. Chen, eds. (2010), vol. 7607, p. 76070K.

[38] T. Gu, R. Nair, and M. W. Haney, "Chip-level multiple quantum well modulator-based optical interconnects," Journal of Lightwave Technology **31**, 4166–4174 (2013).

[39] J. Missinne, N. Teigell Benéitez, A. Lamberti, G. Chiesura, G. Luyckx, M. A. Mattelin, W. Van Paepegem, and G. Van Steenberge, "Thin and Flexible Polymer Photonic Sensor Foils for Monitoring Composite Structures," Advanced Engineering Materials **20**, 1701127 (2018).

[40] S. C. Malek, H. S. Ee, and R. Agarwal, "Strain Multiplexed Metasurface Holograms on a Stretchable Substrate," Nano Letters **17**, 3641–3645 (2017).

[41] Y. Chen, H. Li, and M. Li, "Flexible and tunable silicon photonic circuits on plastic substrates," Scientific Reports **2**, 622 (2012).

[42] D. A. Lauffenburger and A. F. Horwitz, "Cell Migration: A Physically Integrated Molecular Process," Cell **84**, 359–369 (1996).

[43] R. Sunyer, V. Conte, J. Escribano, A. Elosegui-Artola, A. Labernadie, L. Valon, D. Navajas, J. M. García-Aznar, J. J. Muñoz, P. Roca-Cusachs, and X. Trepat, "Collective cell durotaxis emerges from long-range intercellular force transmission," Science **353**, 1157–1161 (2016).

[44] D. A. Lee, M. M. Knight, J. J. Campbell, and D. L. Bader, "Stem cell mechanobiology." Journal of cellular biochemistry **112**, 1–9 (2011).

[45] V. W. Wong, M. T. Longaker, and G. C. Gurtner, "Soft tissue mechanotransduction in wound healing and fibrosis." Seminars in cell & developmental biology **23**, 981–6 (2012).

[46] J. J. Tomasek, G. Gabbiani, B. Hinz, C. Chaponnier, and R. A. Brown, "Myofibroblasts and mechano: Regulation of connective tissue remodelling," (2002).

[47] W. J. Polacheck and C. S. Chen, "Measuring cell-generated forces: A guide to the available tools," (2016).

[48] G. Cheng, J. Tse, R. K. Jain, and L. L. Munn, "Micro-environmental mechanical stress controls tumor spheroid size and morphology by suppressing proliferation and inducing apoptosis in cancer cells." PloS one **4**, e4632 (2009).

[49] V. S. Polikov, P. A. Tresco, and W. M. Reichert, "Response of brain tissue to chronically implanted neural electrodes." Journal of neuroscience methods **148**, 1–18 (2005).

[50] C. Franck, S. Hong, S. A. Maskarinec, D. A. Tirrell, and G. Ravichandran, "Three-dimensional Full-field Measurements of Large Deformations in Soft Materials Using Confocal Microscopy and Digital Volume Correlation," Experimental Mechanics **47**, 427–438 (2007).

[51] S. V. Plotnikov, B. Sabass, U. S. Schwarz, and C. M. Waterman, "High-Resolution Traction Force Microscopy," in "Methods in Cell Biology," , vol. 123 (2014), pp. 367–394.

[52] R. W. Style, R. Boltyanskiy, G. K. German, C. Hyland, C. W. Macminn, A. F. Mertz, L. A. Wilen, Y. Xu, and E. R. Dufresne, "Traction force microscopy in physics and biology," (2014).

[53] B. Sabass, M. L. Gardel, C. M. Waterman, and U. S. Schwarz, "High resolution traction force microscopy based on experimental and computational advances," Biophysical Journal **94**, 207–220 (2008).

[54] S. J. Han, Y. Oak, A. Groisman, and G. Danuser, "Traction microscopy to identify force modulation in subresolution adhesions," Nature Methods **12**, 653–656 (2015).

[55] C. M. Cesa, N. Kirchgessner, D. Mayer, U. S. Schwarz, B. Hoffmann, and R. Merkel, "Micropatterned silicone elastomer substrates for high resolution analysis of cellular force patterns." The Review of scientific instruments **78**, 034301 (2007).

[56] S. Lee, J. Hong, and J. Lee, "Cell motility regulation on a stepped micro pillar array device (SMPAD) with a discrete stiffness gradient," Soft Matter **12**, 2325–2333 (2016).

[57] S. Ghassemi, G. Meacci, S. Liu, A. A. Gondarenko, A. Mathur, P. Roca-Cusachs, M. P. Sheetz, and J. Hone, "Cells test substrate rigidity by local contractions on submicrometer pillars," Proceedings of the National Academy of Sciences **109**, 5328–5333 (2012).

[58] J. L. Tan, J. Tien, D. M. Pirone, D. S. Gray, K. Bhadriraju, and C. S. Chen, "Cells lying on a bed of microneedles: an approach to isolate mechanical force." Proceedings of the National Academy of Sciences of the United States of America **100**, 1484–9 (2003).

[59] F. Meng, T. M. Suchyna, and F. Sachs, "A fluorescence energy transfer-based mechanical stress sensor for specific proteins in situ," FEBS Journal **275**, 3072–3087 (2008).

[60] B. L. Blakely, C. E. Dumelin, B. Trappmann, L. M. McGregor, C. K. Choi, P. C. Anthony, V. K. Duesterberg, B. M. Baker, S. M. Block, D. R. Liu, and C. S. Chen, "A DNA-based molecular probe for optically reporting cellular traction forces," Nature Methods **11**, 1229–1232 (2014).

[61] C. Grashoff, B. D. Hoffman, M. D. Brenner, R. Zhou, M. Parsons, M. T. Yang, M. A. McLean, S. G. Sligar, C. S. Chen, T. Ha, and M. A. Schwartz, "Measuring mechanical tension across vinculin reveals regulation of focal adhesion dynamics," Nature **466**, 263–266 (2010).

[62] N. Lu, C. Lu, S. Yang, and J. Rogers, "Highly Sensitive Skin-Mountable Strain Gauges Based Entirely on Elastomers," Advanced Functional Materials **22**, 4044–4050 (2012).

[63] Z. Bao and X. Chen, "Flexible and Stretchable Devices," Advanced Materials **28**, 4177–4179 (2016).

[64] D. J. Lipomi, M. Vosgueritchian, B. C.-K. Tee, S. L. Hellstrom, J. A. Lee, C. H. Fox, and Z. Bao, "Skin-like pressure and strain sensors based on transparent elastic films of carbon nanotubes," Nature Nanotechnology **6**, 788–792 (2011).

[65] S. Park, M. Vosguerichian, and Z. Bao, "A review of fabrication and applications of carbon nanotube film-based flexible electronics," (2013).

[66] J. T. Muth, D. M. Vogt, R. L. Truby, Y. Mengüç, D. B. Kolesky, R. J. Wood, and J. A. Lewis, "Embedded 3D printing of strain sensors within highly stretchable elastomers." Advanced materials (Deerfield Beach, Fla.) **26**, 6307–12 (2014).

[67] J. Toyjanova, E. Bar-Kochba, C. López-Fagundo, J. Reichner, D. Hoffman-Kim, and C. Franck, "High resolution, large deformation 3D traction force microscopy," PLoS ONE **9**, e90976 (2014).

[68] C. Franck, S. A. Maskarinec, D. A. Tirrell, and G. Ravichandran, "Three-dimensional traction force microscopy: A new tool for quantifying cell-matrix interactions," PLoS ONE **6**, e17833 (2011).

[69] A. Buljac, C. Jailin, A. Mendoza, J. Neggers, T. Taillandier-Thomas, A. Bouterf, B. Smaniotto, F. Hild, and S. Roux, "Digital Volume Correlation: Review of Progress and Challenges," Experimental Mechanics **58**, 661–708 (2018).

[70] F. Gillard, R. Boardman, M. Mavrogordato, D. Hollis, I. Sinclair, F. Pierron, and M. Browne, "The application of digital volume correlation (DVC) to study the microstructural behaviour of trabecular bone during compression," Journal of the Mechanical Behavior of Biomedical Materials **29**, 480–499 (2014).

[71] H. Xu, S. F. Othman, and R. L. Magin, "Monitoring Tissue Engineering Using Magnetic Resonance Imaging," Journal of Bioscience and Bioengineering **106**, 515–527 (2008).

[72] D. A. Long, *Raman spectroscopy* (McGraw-Hill, 1977).

[73] K. Kneipp, M. Moskovits, and H. Kneipp, eds., *Surface-Enhanced Raman Scattering*, vol. 103 of *Topics in Applied Physics* (Springer Berlin Heidelberg, 2006).

[74] A. Campion and P. Kambhampati, "Surface-enhanced Raman scattering," Chemical Society Reviews **27**, 241 (1998).

[75] L. Jensen, C. M. Aikens, and G. C. Schatz, "Electronic structure methods for studying surface-enhanced Raman scattering," Chemical Society Reviews **37**, 1061–1073 (2008).

[76] K. Kneipp, Y. Wang, H. Kneipp, L. T. Perelman, I. Itzkan, R. R. Dasari, and M. S. Feld, "Single molecule detection using surface-enhanced raman scattering (SERS)," Physical Review Letters **78**, 1667–1670 (1997).

[77] S. Nie and S. R. Emory, "Probing Single Molecules and Single Nanoparticles by Surface-Enhanced Raman Scattering," Science **275**, 1102–6 (1997).

[78] B. Sharma, R. R. Frontiera, A. I. Henry, E. Ringe, and R. P. Van Duyne, "SERS: Materials, applications, and the future," (2012).

[79] J. P. Camden, J. A. Dieringer, Y. Wang, D. J. Masiello, L. D. Marks, G. C. Schatz, and R. P. Van Duyne, "Probing the structure of single-molecule surface-enhanced Raman scattering hot spots," Journal of the American Chemical Society **130**, 12616–12617 (2008).

[80] E. C. Le Ru, E. Blackie, M. Meyer, and P. G. Etchegoint, "Surface enhanced raman scattering enhancement factors: A comprehensive study," Journal of Physical Chemistry C **111**, 13794–13803 (2007).

[81] H. Yan, L. Huang, X. Xu, S. Chakravarty, N. Tang, H. Tian, and R. T. Chen, "Unique surface sensing property and enhanced sensitivity in microring resonator biosensors based on subwavelength grating waveguides," Optics Express **24**, 29724 (2016).

[82] L. Li, H. Lin, S. Qiao, Y.-Z. Huang, J.-Y. Li, J. Michon, T. Gu, C. Alosno-Ramos, L. Vivien, A. Yadav, K. Richardson, N. Lu, and J. Hu, "Monolithically integrated stretchable photonics," Light: Science & Applications **7**, 17138 (2018).

[83] S. Timoshenko, *Theory of elastic stability* (McGraw-Hill, New York, 1961), 2nd ed.

[84] T. Hauck, W. H. Müller, and I. Schmadlak, "Nonlinear buckling analysis of vertical wafer probe technology," Microsystem Technologies **16**, 1909–1920 (2010).

[85] H. Aben, J. Anton, and A. Errapart, "Modern photoelasticity for residual stress measurement in glass," in "Strain," , vol. 44 (Springer Netherlands, Dordrecht, 2008), vol. 44, pp. 40–48.

[86] J. F. Orr and J. B. Finlay, "Photoelastic stress analysis," in "Optical measurement methods in biomechanics," (Springer US, Boston, MA, 2007), pp. 1–16.

[87] W. J. Westerveld, J. Pozo, P. J. Harmsma, R. Schmits, E. Tabak, T. C. van den Dool, S. M. Leinders, K. W. A. van Dongen, H. P. Urbach, and M. Yousefi, "Characterization of a photonic strain sensor in silicon-on-insulator technology." Optics letters **37**, 479–81 (2012).

[88] L. Fan, L. T. Varghese, Y. Xuan, J. Wang, B. Niu, and M. Qi, "Direct fabrication of silicon photonic devices on a flexible platform and its application for strain sensing." Optics express **20**, 20564–75 (2012).

[89] J. Hu, X. Sun, A. Agarwal, and L. C. Kimerling, "Design guidelines for optical resonator biochemical sensors," Journal of the Optical Society of America B **26**, 1032 (2009).

[90] S. R. Quake, "From Micro- to Nanofabrication with Soft Materials," Science **290**, 1536–1540 (2000).

[91] H. Ma, A.-Y. Jen, and L. Dalton, "Polymer-Based Optical Waveguides: Materials, Processing, and Devices," Advanced Materials **14**, 1339–1365 (2002).

[92] G. T. Paloczi, Y. Huang, and A. Yariv, "Free-standing all-polymer microring resonator optical filter," (2003).

[93] B. Bhola and W. H. Steier, "A Novel Optical Microring Resonator Accelerometer," IEEE Sensors Journal **7**, 1759–1766 (2007).

[94] S. Ashkenazi, C.-Y. Chao, L. J. Guo, and M. O'Donnell, "Ultrasound detection using polymer microring optical resonator," Applied Physics Letters **85**, 5418 (2004).

[95] J. Clark and G. Lanzani, "Organic photonics for communications," Nature Photonics **4**, 438–446 (2010).

[96] D. Chen, H. R. Fetterman, A. Chen, W. H. Steier, L. R. Dalton, W. Wang, and Y. Shi, "Demonstration of 110 GHz electro-optic polymer modulators," Applied Physics Letters **70**, 3335 (1997).

[97] E. Yablonovitch, T. Gmitter, J. P. Harbison, and R. Bhat, "Extreme selectivity in the lift-off of epitaxial GaAs films," Applied Physics Letters **51**, 2222 (1987).

[98] B. J. Eggleton, B. Luther-Davies, and K. Richardson, "Chalcogenide Photonics," Nature Photonics **5** (2011).

[99] M. Kawachi, "Silica waveguides on silicon and their application to integrated-optic components," Optical and Quantum Electronics **22**, 391–416 (1990).

[100] J. T. Choy, J. D. B. Bradley, P. B. Deotare, I. B. Burgess, C. C. Evans, E. Mazur, and M. Lončar, "Integrated TiO2 resonators for visible photonics." Optics letters **37**, 539–41 (2012).

[101] B. Rangarajan, A. Y. Kovalgin, K. Wörhoff, and J. Schmitz, "Low-temperature deposition of high-quality silicon oxynitride films for CMOS-integrated optics." Optics letters **38**, 941–3 (2013).

[102] A. Agarwal, J. Hu, K. Richardson, L. Petit, L. C. Kimerling, and N. Carlie, "Cavity-Enhanced IR Absorption in Planar Chalcogenide Glass Microdisk Resonators: Experiment and Analysis," Journal of Lightwave Technology, Vol. 27, Issue 23, pp. 5240-5245 **27**, 5240–5245 (2009).

[103] A. Seddon, "Chalcogenide glasses: a review of their preparation, properties and applications," Journal of Non-Crystalline Solids **184**, 44–50 (1995).

[104] C. Quémard, F. Smektala, V. Couderc, A. Barthélémy, and J. Lucas, "Chalcogenide glasses with high non linear optical properties for telecommunications," Journal of Physics and Chemistry of Solids **62**, 1435–1440 (2001).

[105] G. Pfeiffer, M. Paesler, and S. Agarwal, "Reversible photodarkening of amorphous arsenic chalcogens," Journal of Non-Crystalline Solids **130**, 111–143 (1991).

[106] L. Li, P. Zhang, W.-M. Wang, H. Lin, A. B. Zerdoum, S. J. Geiger, Y. Liu, N. Xiao, Y. Zou, O. Ogbuu, Q. Du, X. Jia, J. Li, and J. Hu, "Foldable and Cytocompatible Sol-gel TiO2 Photonics." Scientific reports **5**, 13832 (2015).

[107] J. Hu, L. Li, H. Lin, Y. Zou, Q. Du, C. Smith, S. Novak, K. Richardson, and J. D. Musgraves, "Chalcogenide glass microphotonics: Stepping into the spotlight," American Ceramic Society Bulletin **94**, 24–29 (2015).

[108] H. Lin, Y. Song, Y. Huang, D. Kita, S. Deckoff-Jones, K. Wang, L. Li, J. Li, H. Zheng, Z. Luo, H. Wang, S. Novak, A. Yadav, C.-C. Huang, R.-J. Shiue, D. Englund, T. Gu, D. Hewak, K. Richardson, J. Kong, and J. Hu, "Chalcogenide glass-on-graphene photonics," Nature Photonics **11**, 798–805 (2017).

[109] H. Lorenz, M. Laudon, and P. Renaud, "Mechanical characterization of a new high-aspect-ratio near UV-photoresist," Microelectronic Engineering **41-42**, 371–374 (1998).

[110] S. Keller, G. Blagoi, M. Lillemose, D. Haefliger, and A. Boisen, "Processing of thin SU-8 films," Journal of Micromechanics and Microengineering **18**, 125020 (2008).

[111] R. P. Wang, A. V. Rode, S. J. Madden, C. J. Zha, R. A. Jarvis, and B. Luther-Davies, "Structural relaxation and optical properties in amorphous Ge33As12Se55 films," Journal of Non-Crystalline Solids **353**, 950–952 (2007).

[112] F. Vanier, M. Rochette, N. Godbout, and Y.-A. Peter, "Raman lasing in As2S3 high-Q whispering gallery mode resonators," Optics Letters **38**, 4966 (2013).

[113] Y. Zou, L. Moreel, H. Lin, J. Zhou, L. Li, S. Danto, J. D. Musgraves, E. Koontz, K. Richardson, K. D. Dobson, R. Birkmire, and J. Hu, "Solution Processing and Resist-Free Nanoimprint Fabrication of Thin Film Chalcogenide Glass Devices: Inorganic-Organic Hybrid Photonic Integration," Advanced Optical Materials **2**, 759–764 (2014).

[114] S. J. Madden, D.-Y. Choi, D. A. Bulla, A. V. Rode, B. Luther-Davies, V. G. Ta'eed, M. D. Pelusi, and B. J. Eggleton, "Long, low loss etched As2S3 chalcogenide waveguides for all-optical signal regeneration," Optics Express **15**, 14414 (2007).

[115] J. Chiles, M. Malinowski, A. Rao, S. Novak, K. Richardson, and S. Fathpour, "Extremely Low-Loss Chalcogenide Photonics Devices with Chlorine-Based Plasma Etching," in "CLEO: 2015," (OSA, Washington, D.C., 2015), p. STh1G.6.

[116] Q. Du, Y. Huang, J. Li, D. Kita, J. Michon, H. Lin, L. Li, S. Novak, K. Richardson, W. Zhang, and J. Hu, "Low-loss photonic device in GeâĂŞSbâĂŞS chalcogenide glass," Optics Letters **41**, 3090 (2016).

[117] K. R. Williams and R. S. Muller, "Etch rates for micromachining processing," Journal of Microelectromechanical Systems **5**, 256–269 (1996).

[118] V. R. Almeida, R. R. Panepucci, and M. Lipson, "Nanotaper for compact mode conversion," Optics Letters **28**, 1302 (2007).

[119] M. Papes, P. Cheben, D. Benedikovic, J. H. Schmid, J. Pond, R. Halir, A. Ortega-Moñux, G. Wangüemert-Pérez, W. N. Ye, D.-X. Xu, S. Janz, M. Dado, and V. Vašinek, "Fiber-chip edge coupler with large mode size for silicon photonic wire waveguides," Optics Express **24**, 5026 (2016).

[120] D. Ohana and U. Levy, "Mode conversion based on dielectric metamaterial in silicon," Optics Express **22**, 27617 (2014).

[121] J. R. Ong, T. Y. L. Ang, G. Alagappan, C. H. Son, S. T. Lim, and C. E. Png, "Silicon nitride double-tip fiber-to-waveguide edge couplers at visible wavelengths," in "2017

Conference on Lasers and Electro-Optics Pacific Rim (CLEO-PR)," (IEEE, 2017), pp. 1–3.

[122] D. Taillaert, W. Bogaerts, P. Bienstman, T. F. Krauss, P. Van Daele, I. Moerman, S. Verstuyft, K. De Mesel, and R. Baets, "An out-of-plane grating coupler for efficient butt-coupling between compact planar waveguides and single-mode fibers," IEEE Journal of Quantum Electronics **38**, 949–955 (2002).

[123] D. Taillaert, F. Van Laere, M. Ayre, W. Bogaerts, D. Van Thourhout, P. Bienstman, and R. Baets, "Grating couplers for coupling between optical fibers and nanophotonic waveguides," Japanese Journal of Applied Physics, Part 1: Regular Papers and Short Notes and Review Papers **45**, 6071–6077 (2006).

[124] G. A. Koepf and B. J. Markey, "Fabrication and characterization of a 2-D fiber array," Applied Optics **23**, 3515 (2009).

[125] D. M. Kita, B. Miranda, D. Favela, D. Bono, J. J. Michon, H. Lin, T. Gu, and J. Hu, "High-performance and scalable on-chip digital Fourier transform spectroscopy," Nature Communications **9**, 4405 (2018).

[126] S. R. Ovshinsky, "Reversible electrical switching phenomena in disordered structures," Physical Review Letters **21**, 1450–1453 (1968).

[127] K. Shimakawa, A. Kolobov, and S. R. Elliott, "Photoinduced effects and metastability in amorphous semiconductors and insulators," Advances in Physics **44**, 475–588 (1995).

[128] H. Fritzsche, "Light-Induced Structural Changes in Glasses," in "Insulating and Semiconducting Glasses," , P. Boolchand, ed. (2010), pp. 653–690, world scie ed.

[129] A. Kozdras, "Kinetics of light-assisted physical ageing in S-rich arsenic sulphide glasses," Bulletin of Materials Science **39**, 997–1000 (2016).

[130] Y. Kokubun, S. Taga, and M. Takizawa, "Three-dimensional athermal waveguides for temperature independent lightwave devices," Electronics Letters **30**, 1223–1224 (2002).

[131] M. M. Milošević, N. G. Emerson, F. Y. Gardes, X. Chen, A. A. D. T. Adikaari, and G. Z. Mashanovich, "Athermal waveguides for optical communication wavelengths," Optics Letters **36**, 4659 (2011).

[132] A. Yariv, "Universal relations for coupling of optical power between microresonators and dielectric waveguides," Electronics Letters **36**, 321 (2000).

[133] A. Yariv, "Critical coupling and its control in optical waveguide-ring resonator systems," IEEE Photonics Technology Letters **14**, 483–485 (2002).

[134] J. D. Joannopoulos, S. G. Johnson, J. N. Winn, R. D. Meade, and C. J. Sjödahl, *Photonic crystals: molding the flow of light*, vol. 60 (Princeton University Press, 2011).

[135] P. B. Deotare, M. W. McCutcheon, I. W. Frank, M. Khan, and M. Lončar, "High quality factor photonic crystal nanobeam cavities," Applied Physics Letters **94**, 121106 (2009).

[136] J. P. Berenger, "A perfectly matched layer for the absorption of electromagnetic waves," Journal of Computational Physics **114**, 185–200 (1994).

[137] J. R. de Lasson, L. H. Frandsen, P. Gutsche, S. Burger, O. S. Kim, O. Breinbjerg, A. Ivinskaya, F. Wang, O. Sigmund, T. Häyrynen, A. V. Lavrinenko, J. Mørk, and N. Gregersen, "Benchmarking five numerical simulation techniques for computing resonance wavelengths and quality factors in photonic crystal membrane line defect cavities," Optics Express **26**, 11366 (2017).

[138] N. Gregersen, S. Reitzenstein, C. Kistner, M. Strauss, C. Schneider, S. Höfling, L. Worschech, A. Forchel, T. R. Nielsen, J. Mørk, and J. M. Gérard, "Numerical and experimental study of the Q factor of high-Q micropillar cavities," IEEE Journal of Quantum Electronics **46**, 1470–1483 (2010).

[139] Y. Gong and J. Vučković, "Photonic crystal cavities in silicon dioxide," Applied Physics Letters **96**, 031107 (2010).

[140] Q. Quan, I. B. Burgess, S. K. Y. Tang, D. L. Floyd, and M. Loncar, "High-Q, low index-contrast polymeric photonic crystal nanobeam cavities," Optics Express **19**, 22191 (2011).

[141] S. Mandal and D. Erickson, "Nanoscale optofluidic sensor arrays," Optics Express **16**, 1623 (2008).

[142] Q. Quan, P. B. Deotare, and M. Loncar, "Photonic crystal nanobeam cavity strongly coupled to the feeding waveguide," Applied Physics Letters **96**, 203102 (2010).

[143] M. Palamaru and P. Lalanne, "Photonic crystal waveguides: Out-of-plane losses and adiabatic modal conversion," Applied Physics Letters **78**, 1466 (2001).

[144] Z. Wang, A. A. Volinsky, and N. D. Gallant, "Crosslinking effect on polydimethylsiloxane elastic modulus measured by custom-built compression instrument," Journal of Applied Polymer Science **131**, n/a–n/a (2014).

[145] V. Normand, D. L. Lootens, E. Amici, K. P. Plucknett, and P. Aymard, "New insight into agarose gel mechanical properties," Biomacromolecules **1**, 730–738 (2000).

[146] K. Manickam, R. R. Machireddy, and S. Seshadri, "Characterization of biomechanical properties of agar based tissue mimicking phantoms for ultrasound stiffness imaging techniques," Journal of the Mechanical Behavior of Biomedical Materials **35**, 132–143 (2014).

[147] S. Katz and S. Givli, "The post-buckling behavior of a beam constrained by springy walls," Journal of the Mechanics and Physics of Solids **78**, 443–466 (2015).

[148] T. Y. Wang, C. G. Koh, and C. Y. Liaw, "Post-buckling analysis of planar elastica using a hybrid numerical strategy," Computers and Structures **88**, 785–795 (2010).

[149] A. Pocheau and B. Roman, "Uniqueness of solutions for constrained Elastica," Physica D: Nonlinear Phenomena **192**, 161–186 (2004).

[150] B. Roman and A. Pocheau, "Postbuckling of bilaterally constrained rectangular thin plates," Journal of the Mechanics and Physics of Solids **50**, 2379–2401 (2002).

[151] H. Lorenz, M. Despont, N. Fahrni, N. LaBianca, P. Renaud, and P. Vettiger, "SU-8: A low-cost negative resist for MEMS," Journal of Micromechanics and Microengineering **7**, 121–124 (1997).

[152] A. Taflove, A. F. Oskooi, and S. G. Johnson, *Advances in FDTD Computational Electrodynamics: Photonics and Nanotechnology* (2013).

[153] K. H. Drexhage, "Influence of a dielectric interface on fluorescence decay time," Journal of Luminescence **1-2**, 693–701 (1970).

[154] Y. Xu, R. K. Lee, and A. Yariv, "Quantum analysis and the classical analysis of spontaneous emission in a microcavity," Physical Review A **61**, 033807 (2002).

[155] F. Wijnands, J. B. Pendry, F. J. Garcia-Vidal, P. M. Bell, P. J. Roberts, and L. Martín Moreno, "Green's functions for Maxwell's equations: Application to spontaneous emission," Optical and Quantum Electronics **29**, 199–216 (1997).

[156] O. D. Miller, A. G. Polimeridis, M. T. H. Reid, C. W. Hsu, B. G. DeLacy, J. D. Joannopoulos, M. Soljačić, and S. G. Johnson, "Fundamental limits to optical response in absorptive systems," Optics Express **24**, 3329 (2015).

[157] M. T. Homer Reid and S. G. Johnson, "Efficient Computation of Power, Force, and Torque in BEM Scattering Calculations," ArXiv e-prints (2013).

[158] P. Kühler, M. Weber, and T. Lohmüller, "Plasmonic Nanoantenna Arrays for Surface-Enhanced Raman Spectroscopy of Lipid Molecules Embedded in a Bilayer Membrane," ACS Applied Materials & Interfaces **6**, 8947–8952 (2014).

[159] Y. Zou, H. Lin, O. Ogbuu, L. Li, S. Danto, S. Novak, J. Novak, J. D. Musgraves, K. Richardson, and J. Hu, "Effect of annealing conditions on the physio-chemical properties of spin-coated As2Se3 chalcogenide glass films," Optical Materials Express **2**, 1723–1732 (2012).

[160] C. C. Evans, C. Liu, and J. Suntivich, "TiO2 Nanophotonic Sensors for Efficient Integrated Evanescent Raman Spectroscopy," ACS Photonics **3**, 1662–1669 (2016).

[161] A. Ksendzov and Y. Lin, "Integrated optics ring-resonator sensors for protein detection," Optics Letters **30**, 3344 (2005).

[162] A. Yalcin, K. Popat, J. Aldridge, T. Desai, J. Hryniewicz, N. Chbouki, B. Little, V. Van, D. Gill, M. Anthes-Washburn, M. Unlu, and B. Goldberg, "Optical sensing of biomolecules using microring resonators," IEEE Journal of Selected Topics in Quantum Electronics **12**, 148–155 (2006).

[163] A. Nitkowski, L. Chen, and M. Lipson, "Cavity-enhanced on-chip absorption spectroscopy using microring resonators," Optics Express **16**, 11930 (2008).

[164] C.-y. Chao, S. Ashkenazi, S.-w. Huang, M. O'Donnell, and L. Guo, "High-frequency ultrasound sensors using polymer microring resonators," IEEE Transactions on Ultrasonics, Ferroelectrics and Frequency Control **54**, 957–965 (2007).

[165] B. Bhola, P. Nosovitskiy, H. Mahalingam, and W. H. Steier, "Sol-Gel-Based Integrated Optical Microring Resonator Humidity Sensor," IEEE Sensors Journal **9**, 740–747 (2009).

[166] H. Shim, L. Fan, S. G. Johnson, and O. D. Miller, "Fundamental limits to near-field optical response, over any bandwidth," Physical Review X **9**, 011043 (2018).

[167] E. L. Anquillare, O. D. Miller, C. W. Hsu, B. G. DeLacy, J. D. Joannopoulos, S. G. Johnson, and M. Soljačić, "Efficient, designable, and broad-bandwidth optical extinction via aspect-ratio-tailored silver nanodisks," Optics Express **24**, 10806 (2016).

[168] C. M. Lalau-Keraly, S. Bhargava, O. D. Miller, and E. Yablonovitch, "Adjoint shape optimization applied to electromagnetic design," Optics Express **21**, 21693 (2013).